Development of a New High Speed Cable-Based Planar Parallel Manipulator

by

NanNan Sun

A thesis
presented to the University of Waterloo
in fulfillment of the degree of
Master of Applied Science
in
Mechanical Engineering

Waterloo, Ontario, Canada, 2012

I hereby declare that I am the sole author of this thesis. This is a true copy of this thesis, including any required final revisions, as accepted by my examiners

I understand that my thesis may be made electronically available to the public.

Acknowledgements

I would like to thank my supervisor Dr. Amir Khajepour for all the help and guidance on this project. I am honoured and proud to have Dr. Khajepour as my supervisor in my graduate studies. He has such a genius mind and a unique way to approach a problem, and he was always supportive of my research.

I would also like to thank my co-workers from AEMK System. Edmon Chan helped me more than anyone else in my graduate studies. Edmon has great insight and experience in design of cable-based manipulators, and he taught me how to approach many difficult problems. Chris Pop helped me code and debug control program for the robot, as well as setting up test environment.

I would also like to thank partners from Conestoga College; Dr. Hamidreza Karbasi for accepting the partnership program and providing us with opportunity and resources to manufacture a professional prototype of the robot; Greg Virgo for his help in designing a physical model of the robot; Brian Jeffery and Ryan van Veen for their help in manufacturing, assembly, and testing for the robot. Without their help, it would not have been possible to build such a professionally manufactured prototype.

Finally, I would like to thank my parents and friends for encouraging me throughout my graduate studies. Special thanks to Steven Tong and Edward Yam, who have been my friends and classmates since the first year in university. They made my undergraduate and graduate studies at University of Waterloo an unforgettable experience.

Abstract

Industrial robots and automation technology have advanced rapidly in the last several decades. New types of manipulators that uses parallel mechanisms are becoming more popular due to their high speed and high stiffness. This thesis focuses on a sub-class of parallel manipulators that uses cables to replace rigid links for further increase in speed. The design strategies in this study were expanded from research works by Khajepour. Behzadipour, and Edmon Chan. This thesis presents analysis and development of a new cable-based planar parallel manipulator that is based on a previous prototype built by Edmon Chan.

The new manipulator design added a new rotational DOF to the end-effector, and the number of cables are doubled in order to increase the stiffness. New methods for kinematics and dynamics analysis are formulated to make the procedure more systematic. A new mathematical formulation for stiffness matrix of the end-effector is presented. The resultant stiffness matrix is equivalent to the stiffness matrix formulated by Behzadipour. Additional stiffness analysis is conducted on valid range of stiffness calculation and comparison of different cable configurations. A multi-objective optimization problem is formulated in order to search for the best set of design parameters for the manipulator, and it is solved with an exhaustive complete search method.

A physical prototype of the manipulator is modelled and manufactured with the help of partners from Conestoga college. Experiments with the manipulator show that more powerful motors are needed to run the robot at full speed. Motor torque measurements show that the dynamics analysis of the manipulator is valid. Stiffness of the manipulator is measured by applying external force to the end-effector, and it is shown to be strong. The manipulator is able to demonstrate a sort and pick-and-place operation at 60 cycles per minute while running at 70% of the maximum speed, with an acceleration of 2.8 g and velocity of 4 m/s.

Table of Contents

List of Tables

List of Figures

Chapter 1

Introduction

Advancement in automation technology has helped the manufacturing industry grow rapidly in the last several decades. Industry always seeks for faster, better quality, and less expensive solutions. Fast and accurate pick-and-place operation is one of many manufacturing processes helped by automation technology. Typical applications of pick-and-place operations include packaging, sorting, and placing parts for assembly. It is a common practice to align multiple planar pick-and-place robots with a planer workspace to have a conveyer belt carry parts normal to the robot workspace. This speeds up the process and saves precious factory space. In this thesis, a new 2D cable-based parallel manipulator is proposed for fast and accurate pick-and-place operation of light objects, and heavier objects up to 20 *kg* at lower speed.

Desired properties of a pick-and-place robot are speed, accuracy, and repeatability. Accuracy is dependent on the backlash and stiffness of the robot since higher stiffness results in less deformation under high loads. Speed is dependent on actuator power and moving inertia of the robot. High stiffness and powerful actuators typically result in heavier parts which provide more moving inertia. It is up to the designer to make compromises and choose a suitable balance for a design.

The most common type of industrial robots are serial manipulators. Their structure is a series of rigid links connected by various types of joints forming a single of kinematic chain. Each joint is controlled independently by an actuator mounted at the joint, which results in masses of the actuators to be included in the moving inertia of the robot. The motor at the fixed base of the robot must support inertia of all the

links and other motors. This greatly limits the speed and the load capacity of serial manipulators. Furthermore, errors at each joint can accumulate and amplify from link to link which reduces the overall accuracy.

Parallel mechanisms are newer concept for robotic manipulator design. They are closed-loop mechanisms in which the end-effector is connected to the base by two or more independent kinematic chains. Robotic manipulators which uses the parallel mechanism design are becoming increasingly more popular. In parallel manipulators, movements of multiple kinematic chains are coupled together to control the position of the end-effector. This allows all the actuators to be placed at the base, which reduces the moving inertia and effectively increases the maximum speed and load capacity. Accumulation of error is reduced due to the use of multiple kinematic chains. Any force applied to the manipulator is distributed among all the kinematic chains, which also increases stiffness. These properties make parallel manipulators much more attractive compared to serial manipulators for high-speed applications.

Cable-based parallel manipulators have further potential to reduce moving inertia while still maintaining a reasonable amount of stiffness. In a cable-based manipulator, some rigid links are replaced with cables under tension. These cables are virtually massless and they provide good mechanical strength as long as they have tension. In addition to lower moving inertia, cable-based manipulators also have advantages of reduced material cost and less maintenance. However, cable-based manipulators come with their own design challenges. All cables must guaranteed to be under tension at all times in order to avoid structural failure. Cables provide less mechanical stiffness compared to rigid links, hence is it is necessary to analyze stiffness of cable-based manipulators and ensure that the stiffness is high enough. This thesis expands design principles from research done by Khajepour, Behzadipour, and Edmon Chan on cable-based parallel manipulators [1][2][20][22][29]. In particular, this thesis focuses on revising the design and analysis of 2D planer cable-based parallel manipulator researched by Edmon Chan [1].

The layout of this thesis is as follows: Chapter 2 presents literature review of some parallel mechanisms and design considerations regarding cable tension and stiffness that are specific to cable-based mechanisms. Chapter 3 introduces conceptual design and kinematic schemes for the previous prototype by Edmon Chan and a new proposed 2D cable-based parallel manipulator with new features and design changes. Chapter 4 presents new methods for kinematics and dynamics analysis for the new proposed manipulator, which is necessary for performance evaluation, stiffness analysis, and optimization of design parameters. Chapter 5 discusses stiffness analysis for cable-based structures as well as strategies to estimate the validity of stiffness calculations and design cable configurations with better stiffness. Chapter 6 provides methods for the optimization of design parameters and the final set of design parameters selected for building a physical prototype. Chapter 7 presents the design of a fully functional prototype and results from experimental measurements, as well as a pick-and-place demonstration. Chapter 8 gives concluding remarks of this work and highlights future research directions.

Chapter 2

Literature Review

2.1 Introduction to Parallel Mechanisms

The idea and theory of parallel mechanisms existed for a long time. One of the earliest US patent involving a parallel mechanism dates back to 1931; it was an idea of a moving platform for amusement purposes. The first industrial robot patented in US in 1942 is a parallel mechanism, although it was not the first industrial robot built [3]. Early parallel mechanisms were usually targeted for 6 degree of freedom (DOF). One of the simplest designs is the Gough Platform introduced by Gough and Whitehall in 1947 [4]. The Stewart platform is another famous design introduced after the Gough Platform. This type of parallel mechanism is commonly known as the Gough-Stewart platform. Figure 2-1 shows a schematic of the Gough-Stewart platform. Parallel manipulators with this type of design has been most commonly used for motion simulators such as flight simulators [5][6] and tire testing machines [7], and it is still being studied today.

The Gough-Stewart design has limited application as industrial robots due to its large footprint and bulky design. A different type of parallel mechanism called Delta was introduced by Clavel in 1990 [8]. Figure 2-2 shows a schematic of the Delta design. The moving platform is actuated by three kinematic chains, where each one is driven independently. The parallelogram structure on each kinematic chain fixes the orientation of the moving platform. The Delta design has been studied extensively and many modified designs have been proposed [9][10][11].

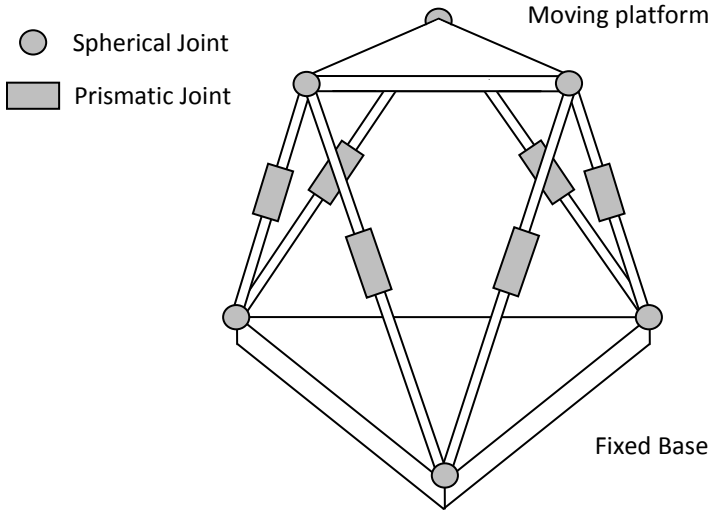

Figure 2-1: Schematic of Gough-Stewart Platform

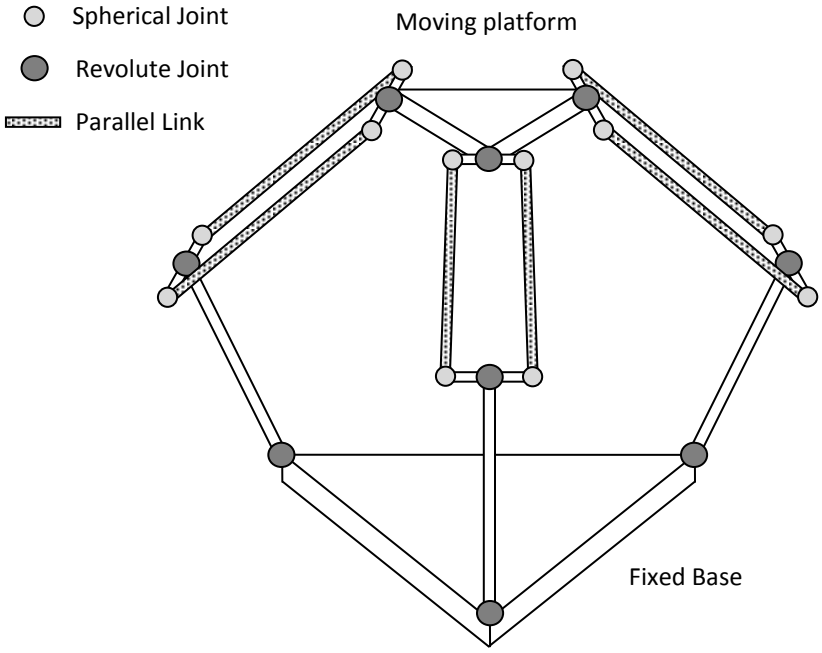

Figure 3-2: Schematic of Delta Design

Some researchers focused on 2DOF translational parallel mechanisms. Ghorbel developed Rice Planar Delta robot in 1990s to demonstrate control and analysis techniques for parallel robot [12]. However, the Rice Planar Delta robot had limited application, because the orientational DOF is coupled with the translational DOF. This problem was later addressed by Huang et al., who introduced parallel links in the structure much like the Delta design [13].

Researches have developed and analyzed many different types of parallel mechanisms. Analysis tools for parallel manipulators are usually subject to certain specific conditions, and there is no universal way to systematically analyse parallel mechanisms. For example, kinematics and dynamics of parallel mechanisms can vary significantly with its design. Some researches choose to use the Denavit–Hartenberg (DH) method for kinematic analysis [14][15], while other researches choose to use geometrical methods [16][17].

2.2 Introduction to Cable-Based Mechanisms

While there are many different types of parallel mechanisms designs, this thesis focuses on one class of parallel mechanisms that uses cables in its kinematic chains. Cable-based parallel mechanisms usually have lower moving inertia compared to parallel mechanisms with rigid links. This allows cable-based mechanisms to achieve very high speed. Additionally, the use of cables reduce manufacturing costs and maintenance requirements. Some early cable-based manipulators are Landsberger's design that is an extension of the Gough-Stewart platform [18], and Falcon design that features high DOF and a large workspace [19]. The Falcon design is an excellent example of high speed of cable-based manipulators, it is capable of achieving an acceleration of 43g and a peak velocity of 13 m/s. Cable-based mechanisms with the Delta design has been studied by Behzadipour et al. for both 3D and planar applications [20]. The design of a new proposed cable-based manipulator in this thesis is an extension of works done by Behzadipour [2] and Edmon Chan [1].

Cable-based manipulators introduce extra design considerations not present in normal parallel manipulators. In order for cables to act as substitutes for rigid links, they must remain under tension at all operation conditions. Ming and Higuchi conducted early studies on tension distribution on high DOF cable-based manipulators [21]. Behzadipour et al. studied cable robot configurations and conditions to guarantee positive cable tensions [22]. Other researchers have also analyzed cable tensions in various types of cable-based manipulators including planar manipulators [23][24]. Another important factor in cable-based manipulator is stiffness analysis, because cables do not provide the same mechanical stiffness as rigid links. Low stiffness can result in less structural rigidity and poor accuracy. Stiffness analysis for parallel manipulators has been studied by many researchers. Griffis and Duffy derived stiffness matrix for a Gough-Stewart platform [25]. Ciblak and Lipkin continued this research by considering an arbitrary number of limbs [26]. Svinin et al. studied stiffness matrix for the stability of parallel manipulators [27][28]. Behzadipour and Khajepour extended stiffness analysis for cable-based mechanisms, and developed stiffness matrix for general cable-based structures using a spring model for cables [29].

Chapter 3

Robot Design Overview

3.1 Introduction of 2D Cable-Based Parallel Manipulator

The main design objective in high-speed manipulators is to reduce moving inertia while maintaining reasonable amount of stiffness. A parallel mechanisms typically have lower moving inertia compared to serial mechanisms because actuators are not part of moving inertia. In order to further reduce moving inertia, this thesis proposes to replace some rigid links with flexible cables. This has additional benefit of reducing material cost and maintenance requirement. One challenge in cable-based manipulator is to make sure that all cables have tension in order to maintain overall stiffness and avoid structural failure. Section 3.1.1 shows conceptual design of the proposed 2D cable-based parallel manipulator and how tension in cables are maintained. Section 3.1.2 discusses necessary conditions to guarantee that all cables are always under tension.

3.1.1 Conceptual Design

The workspace of the proposed manipulator is planer with 2 DOF. Figure 3-1 shows the simplest parallel mechanism to achieve this motion with two angular inputs. Figure 3-2 shows schematic of the proposed cable-based design, which is based on the parallel mechanism shown in Figure 3-1. Actuators attached on the fixed base rotate two upper links, which determine the position and orientation of two lower links. In the cable-based design, the upper links are rigid links called “arms”, and the lower links

are replaced with cables. The end-effector is attached to the lower end of the cables. In order to maintain tension in the cables, a pneumatic cylinder is added to the structure which applies a constant downward force on the end-effector to pull the cables tight and give them tension. This constant downward force is called "*spine force*". Rotational orientation of the end-effector is maintained by a parallelogram structure formed by a pair of two cables on the right side of the manipulator.

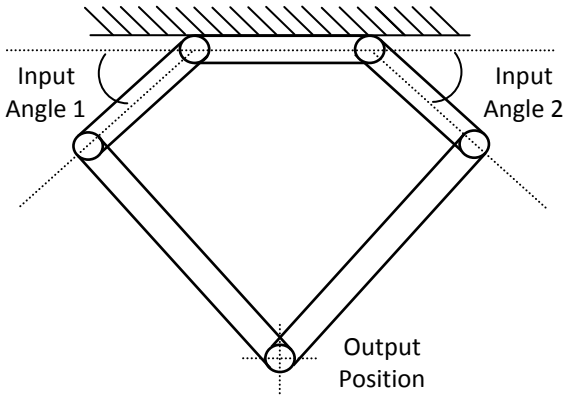

Figure 3-1: Schematic of Simple 2D Parallel Mechanism

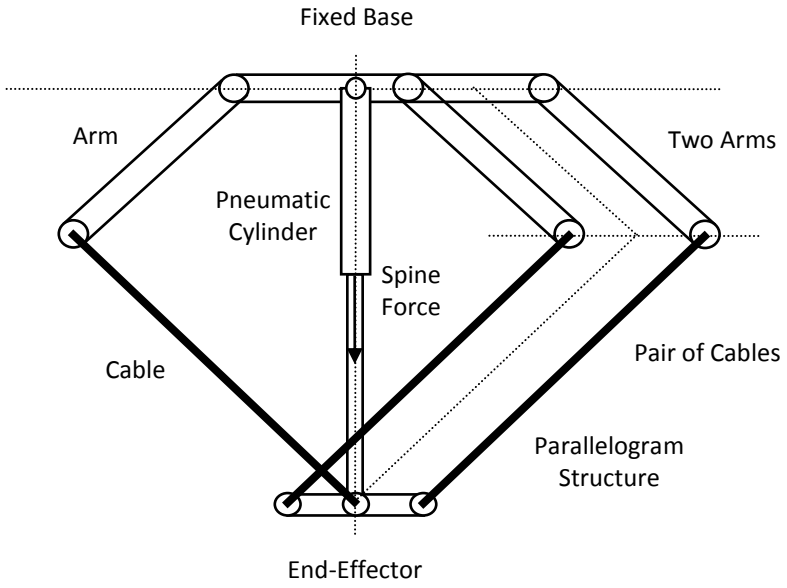

Figure 3-2: Schematic of the Proposed 2D Cable-Based Manipulator

3.1.2 Tensionability

In a cable-based structure, it is crucial that all cables always have tension under any operational circumstance. The cabled-based manipulator proposed in this work uses a pneumatic cylinder to apply constant downward force in order to maintain tension in the cables. Disturbances to cable tension can come from any external force and moment applied to the end-effector, which can be parcel load or force due to acceleration when the end-effector is under a motion.

Other researchers of cabled-based manipulator calls this tension requirement "*tensionability*". The formal definition of tensionability is as following:

Definition: ***Tensionability*** *A non-singular pose is tensionable if and only if for any arbitrary external load, there exists a finite spine force (in this case, the pneumatic cylinder force) to make the manipulator rigid. Tensionability, the ability to apply tension to the cables is a necessary condition to maintain a cable-based manipulator in a rigid pose regardless of any other external load.*

Design of a cable-based manipulator must have a "*tensionable configuration*". This means that tension in all cables monotonically increases with increase in the spine force. This condition guarantees that a finite spine force can balance any external force and moment on the end-effector and maintain tension in all the cables.

Definition: ***Tensionable Configuration*** *In a cable-based manipulator, an end-effector has a tensionable configuration if and only if tensions in all cables increases monotonically with increase in the spine force. An end-effector with tensionable configuration can always satisfy tensionability.*

Tensionable configurations for 3D and 2D cable-based manipulators have been analyzed and proven in works by Behzadipour [2], and Edmon Chan [1]. Both conclusions are best shown graphically. For 3D cable-based manipulator, define a polygon created from cable tension vectors as shown in Figure 3-3. If the spine force is within this polygon, and if all tension vectors and spine force coincide at a single point,

then it is a tensionable configuration. The result is similar for 2D cable-based manipulators. Tensions in the parallel cable pair are combined to a single tension vector, then a region is defined between the two tension vectors as shown in Figure 3-4. If the spine force is within this region, and if the two tension vectors and spine force coincide at a single point, then it is a tensionable configuration. The result for 2D cabled-based manipulator applies to the new proposed manipulator in this thesis.

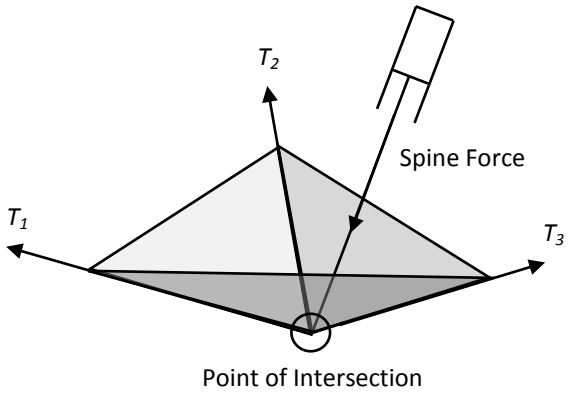

Figure 3-3: Tensionable Configuration for 3D Cable-Based Manipulator

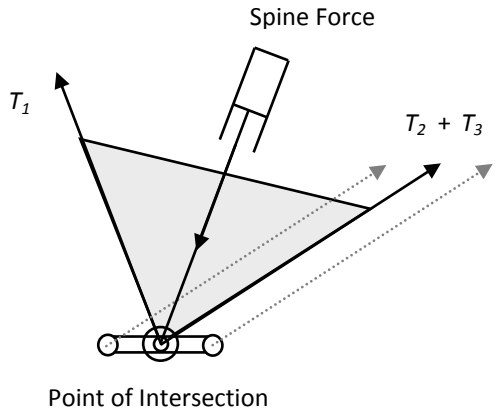

Figure 3-4: Tensionable Configuration for 2D Cable-Based Manipulator

3.2 Design of Previous Prototype

The previous prototype of 2D cable-based manipulator built by Edmon Chan follows the basic design concept discussed in Section 3.1.1. The kinematic scheme of the manipulator is shown in Figure 3-5. The workspace for the previous prototype is 0.7 *m* long and 0.1 *m* high. It is designed for maximum acceleration and velocity of 4 *g* and 4.0 *m/s*, respectively.

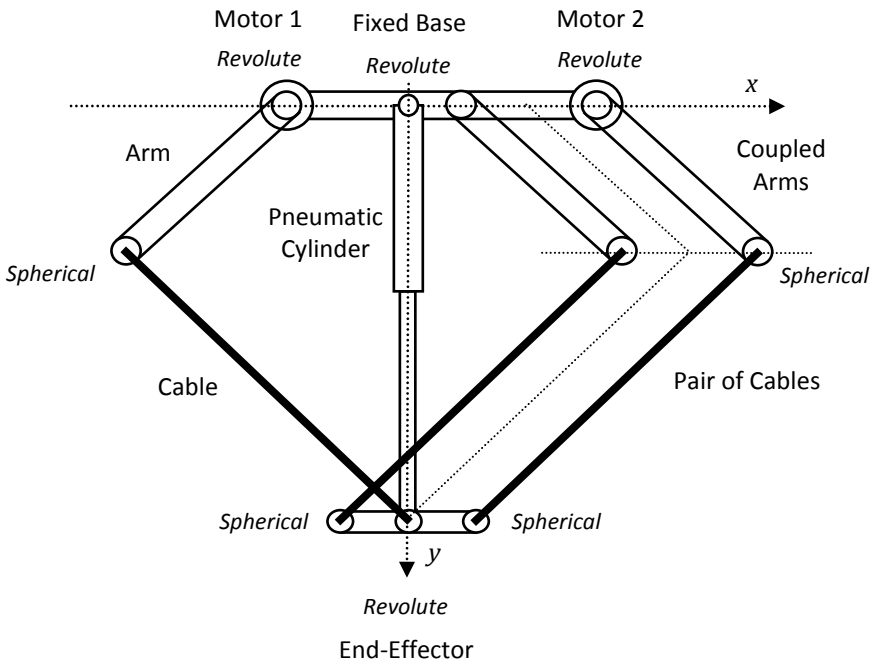

Figure 3-5: Kinematic Scheme of the Previous Manipulator

Two arms on the right side of the manipulator are mechanically coupled with chain linkage to rotate together. This creates the parallelogram structure on the right side and it maintains the orientation of the end-effector. The fixed base and arms are connected with revolute joints at the motor axis. Connections on both side of the cables are spherical joints, but rotations in some axis are limited due to mechanical design of the cable connectors. Since the cable connections are spherical joints with 3 rotational DOF, the end-effector is free to move in and out of the page away from the 2D planar workspace. In this thesis, this type of unwanted motion is defined as "*out-of-plane motion*".

Definition: ***Out-of-Plane Motion*** *In a 2D planar manipulator, movement of the end-effector must be on the workspace plane. Any undesired motion in directions normal to the workspace plane is called out-of-plane motion.*

In order to eliminate out-of-plane motion, the pneumatic cylinder is connected to the fixed base and end-effector with revolute joints, which mechanically constrains the end-effector in the workspace plane. Stiffness of the end-effector in the out-of-plane direction is purely dependent on mechanical stiffness of the pneumatic cylinder and revolute joint. On the other hand, stiffness of the end-effector in the workspace plane is dependent on motor backlash and combination of forces from the spine force and cable tensions.

3.3 Design of New Proposed Manipulator

3.3.1 Design Objectives

The workspace for the new proposed manipulator has a horizontal length of 1.2 *m* and height of 0.3 *m*. This requires the manipulator to be much larger and heavier than the previous design, but it is a goal to maintain high speed of the robot. The new design is aimed at a maximum acceleration and velocity of 4 *g* and 6.0 *m/s*, respectively, and a cycle of time 90 cycles per minute that is comparable to the previous design. One new feature for the proposed design is to add a third DOF for rotation of the end-effector about the vertical axis. This allows the robot to pickup arbitrarily oriented objects and rearrange them in the same orientation. The new DOF is completely independent from the 2 DOF of the planer motion and it does not affect the planer design. In order to transmit the third axis rotation to the end-effector, the two revolute joints on the pneumatic cylinders are replaced with universal joints. Recall that these revolute joints are used to mechanically constrain the end-effector from out-of-plane motion. Replacing them with universal joints would allow the end-effector to move in the out-of-plane direction again. Next section discusses this in more detail, and proposes a new kinematic scheme to solve this problem.

3.3.2 Kinematic Scheme

Front view of the new proposed 2D cable-based manipulator is shown in Figure 3-6. Design of the right side arm is changed to a structure with combination of two parallelograms and a triangle. This structure serves the purpose of both mechanically coupling the two right side arms and maintaining the orientation of the end-effector. Let "*angle of neutral position*" define the angle for the arms that orient the parallelogram into a rectangle. As the arms move away from the angle of neutral, the parallelogram becomes smaller until it is a line, and the structure approaches a singularity. The maximum angular range of the structure is less than 180 degrees, because the two arms mechanically interfere with each other as they move closer to 180 degrees. In order to optimize usage of this limited range, the maximum required range for the arm angle is calculated from kinematic analysis, and then the parallelogram structure is oriented such that angle of neutral position is at the center of the required arm movement range. This concept is shown in Figure 3-7.

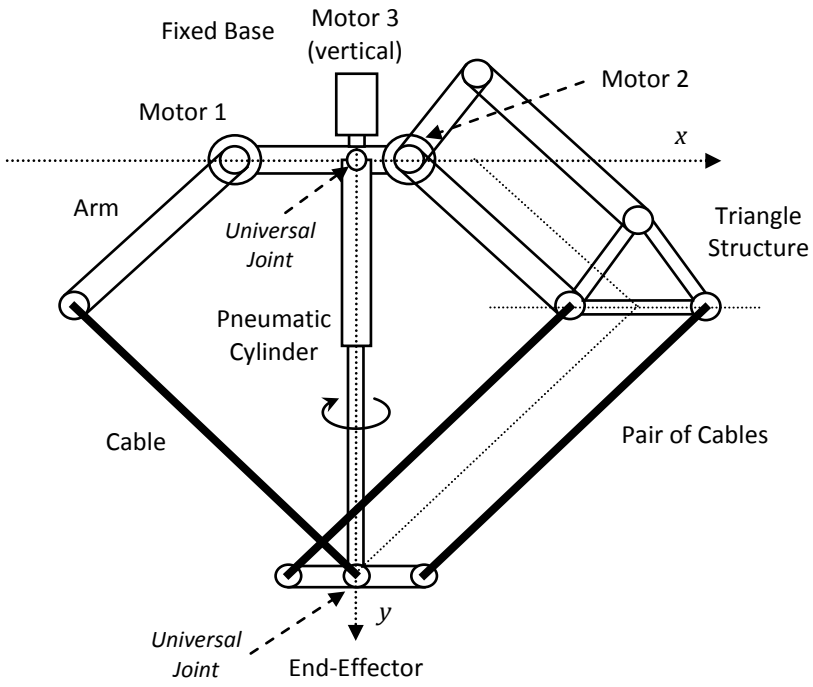

Figure 3-6: Kinematic Scheme of the New Proposed Manipulator (Front)

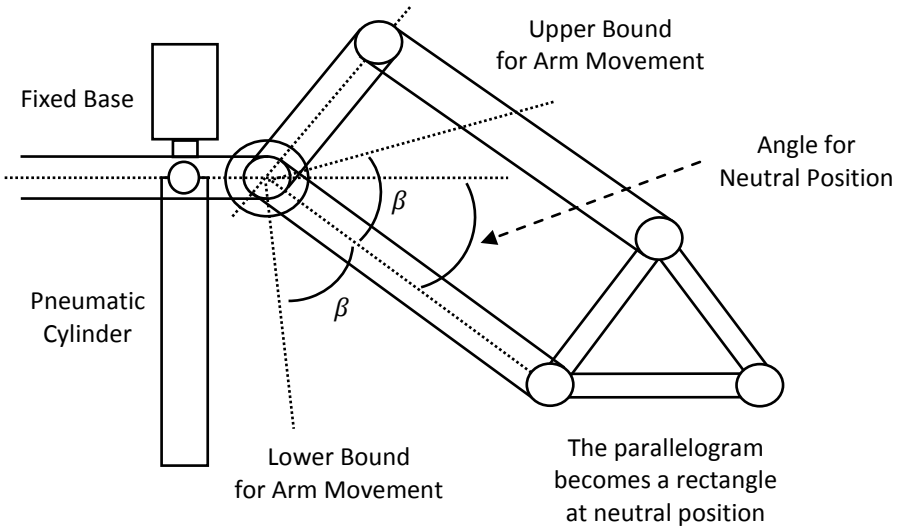

Figure 3-7: Orientation of Arms and Parallelogram Structure

In addition to the two motors for actuating the arms, a third motor is mounted vertically at center of the fixed base. Rotation of the third axis is transmitted from the motor to the end-effector by physically rotating the pneumatic cylinder. Replacing the two revolute joints with two universal joints allows the cylinder to rotate about its longitudinal (extending) axis while still allowing it to swing alone the workspace plane. In order to accommodate this change, the end-effector is separated into two major pieces as shown in Figure 3-8, which illustrates this concept. A large outer base plate encases a smaller inner manipulator piece. The outer base plate has all the cables attached to it in order to maintain angular orientation of the entire end-effector. The inner manipulator piece is attached to the pneumatic cylinder with an universal joint, and it is able to rotate within the fixed base plate. Cable tensions are still maintained by the spine force, which is now transmitted from the pneumatic cylinder to the outer base plate through the inner manipulator piece.

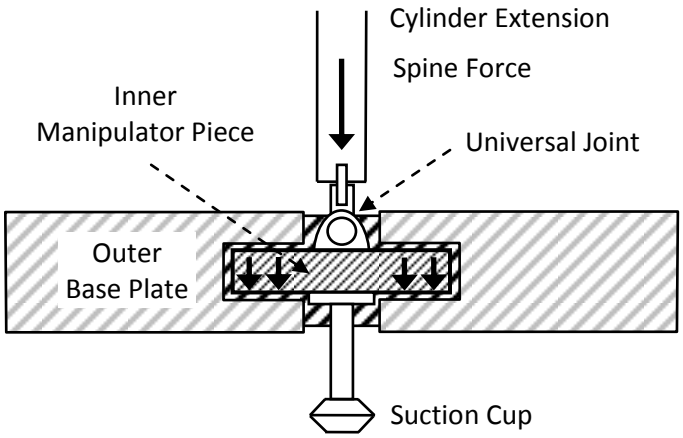

Figure 3-8: Cross-Section View of the New End-Effector Design

As previously mentioned, replacing the revolute joints with universal joints eliminates the mechanical constraint that prevents the end-effector from out-of-plane motion. Figure 3-9 and Figure 3-10 show top view and side view of the new proposed manipulator, respectively. In the design of previous prototype, all cables are on the workspace plane. However, in the new design, each cable is replaced with a pair of two cables as shown in Figure 3-9, which increases the total number of cables to six instead of three. Both Figure 3-9 and Figure 3-10 (*a*) show that on the left side of the structure, the separation distance between pair of cables is constant. However, on the right side of the structure, the separation distance is wider at the arms and becomes narrower towards the end-effector until it is zero. This is an important decision that affects the out-of-plane stiffness of the end-effector, and it is discussed in more detail in Section 5.4. For now it is enough to understand that this cable configuration creates a force relationship shown in Figure 3-10 (*b*) with some cable tensions having an out-of-plane component, which helps increase stiffness in the out-of-plane direction. There are some disadvantages to this six cable design. Increasing the number of cables results in less tension on each cable, thus the spine force must be roughly doubled to maintain the same tension as the three cable design. Although the separation distance at the arms increases out-of-plane stiffness, there is a practical limit since the robot is a 2D manipulator and it is undesirable to have a large out-of-plane profile.

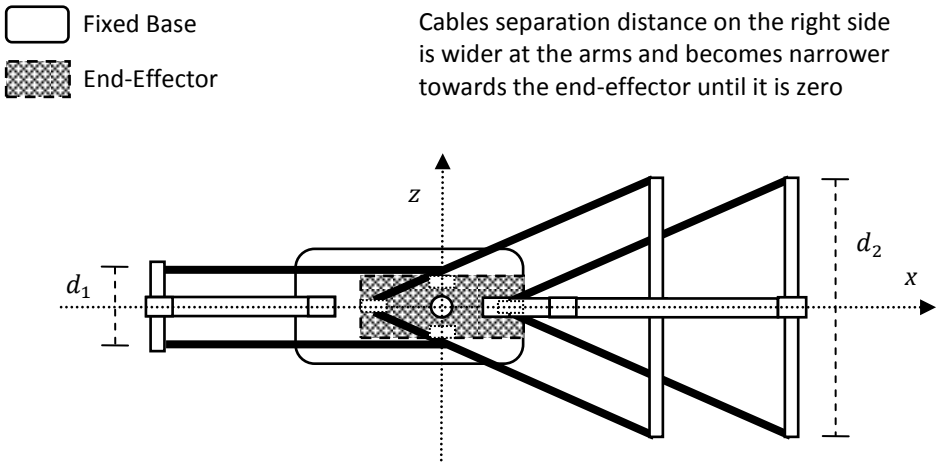

Figure 3-9: Kinematic Scheme of the New Proposed Manipulator (Top)

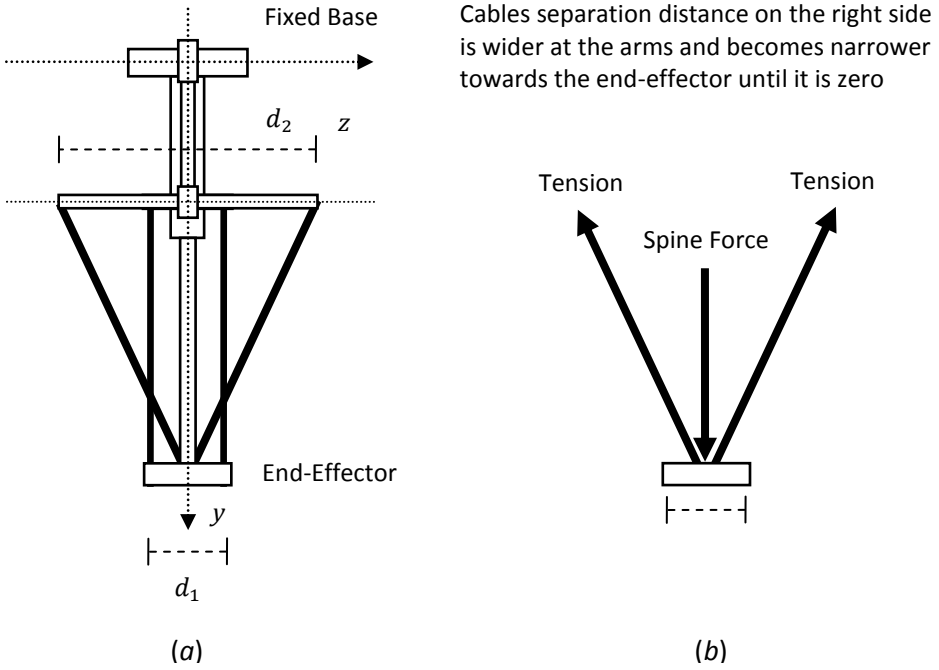

Figure 3-10: Kinematic Scheme of the New Proposed Manipulator (Side)

Chapter 4

Kinematics and Dynamics Analysis

4.1 Coordinate System and Parameters

This section defines the coordinate system, dimensional parameters, and numbering conventions used for the kinematic and dynamic analysis. Refer to Figure 4-1 and 4-2 for graphical information. This will help in reading and understanding rest of this section. More parameters are introduced later as needed.

Coordinate System

x-axis:	horizontal axis, positive is towards the right side in the front view
y-axis:	vertical axis, positive is downward in the front view
z-axis:	out-of-plane axis, positive is into of the page in the front view
P_0:	coordinate origin, located at the upper universal joint
P_E:	coordinate of the end-effector, located at the lower universal joint

Kinematic Parameters

L_B:	length between the origin and axis of left side motor
L_A:	length of the arm
L_C:	length of the cable **in the front view**, note that this is not the true cable length
L_E:	length of the end-effector, it is also the distance between the cables at the triangle
L_{AL}:	length of the cable separation distance at the left arm
L_{AR}:	length of the cable separation distance at the right arm(s)
θ_1:	Angle of the left arm from the horizontal axis, positive is CCW
θ_2:	Angle of the right arm(s) from the horizontal axis, positive is CW

Numbering Convention

Arms: arms are numbered 1 to 3 from left to right as shown in Figure 4-1.

Cables: cables are numbered 1 to 6 as shown in Figure 4-2.

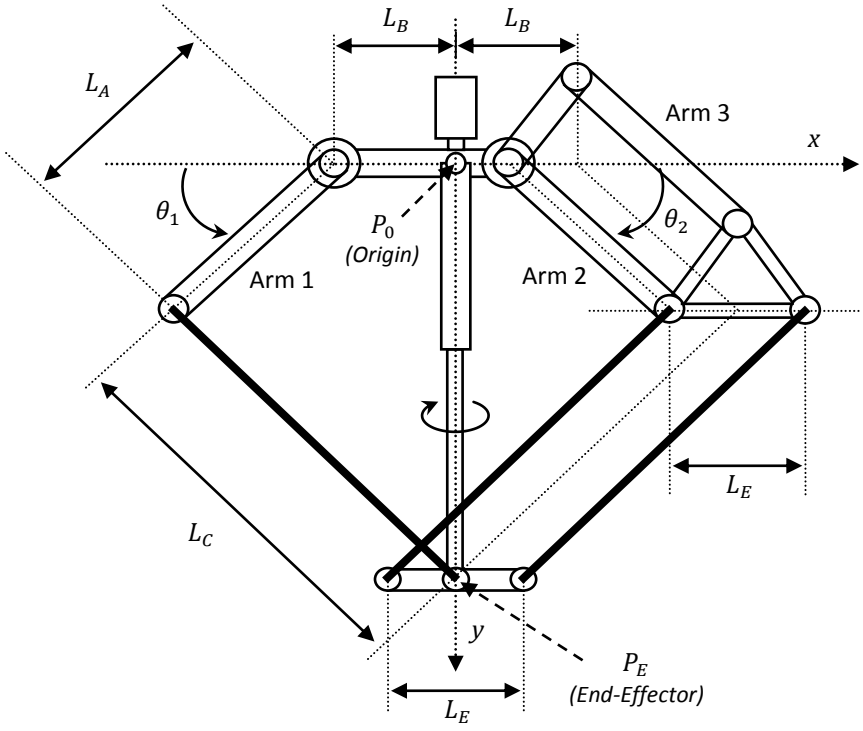

Figure 4-1: Fully Labelled Kinematic Scheme (Front)

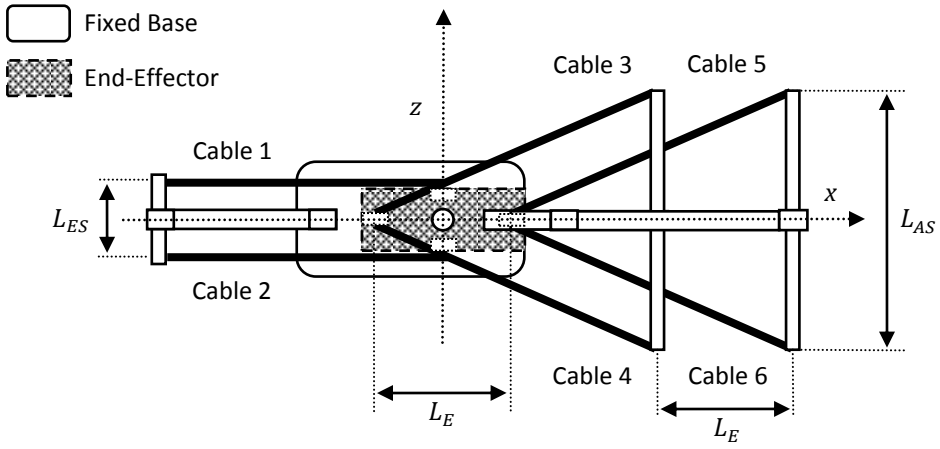

Figure 4-2: Fully Labelled Kinematic Scheme (Top)

4.2 Kinematic Analysis

In order to simplify the formulation of forward kinematic and inverse kinematic analysis for the manipulator, the robot model is simplified into a kinematically equivalent system shown in Figure 4-3. The parallelogram structure on the right is collapsed to a structure equivalent to the left side. P_{A1} and P_{A2} are coordinates of cable connections to left arm and right arm respectively.

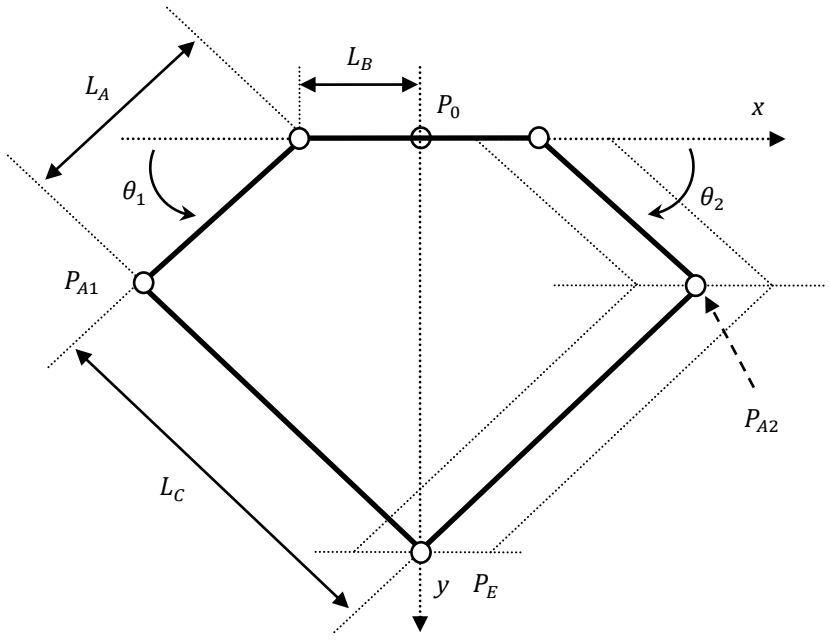

Figure 4-3: Kinematically Equivalent System

4.2.1 Forward Kinematic

Forward kinematic for the system shown in Figure 4-3 can be solved using intersection of two circles on a plane as shown in Figure 4-4. The two circles are centered at P_{A1} and P_{A2} with both having radius of L_C. There are variety of methods to solve intersection of two circles, and this thesis does not cover a specific method since the problem is trivial. Note that in the case of two solutions to the problem, the solution with the largest *y* value is selected to keep end end-effector below the fixed base.

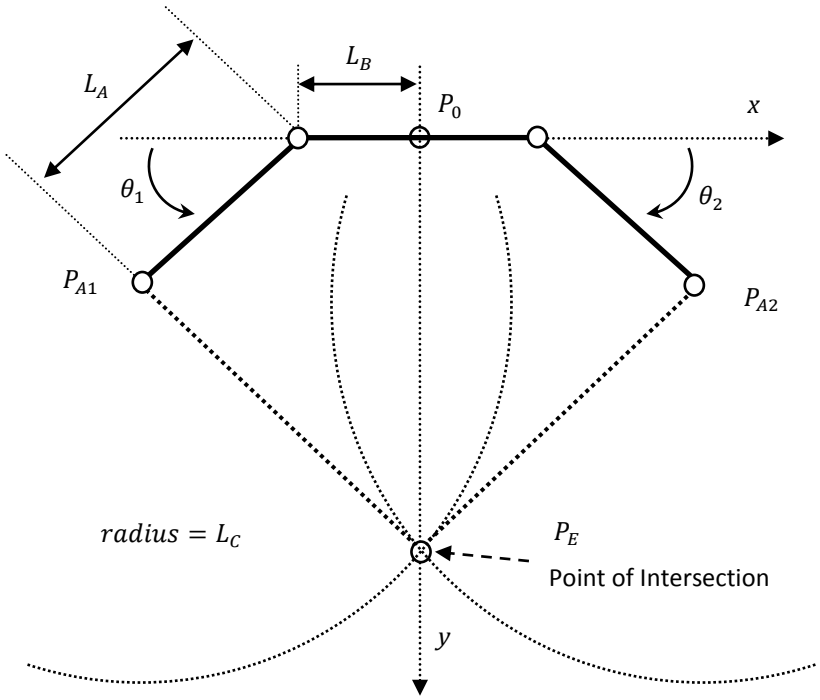

Figure 4-4: Forward Kinematic

4.2.2 Inverse Kinematic

Inverse kinematic is solved geometrically using the cosine law. The solution for the right side system (θ_2) is shown in Equations (4.1) and Figure 4-5 on the next page. Due to the symmetry about the *y*-axis, the solution for the left side system (θ_1) uses the same equations with negative value of *x*.

$$\theta_A(x,y) = cos^{-1}\left(\frac{{L_A}^2 + (y^2 + (L_B - x)^2) - {L_C}^2}{2L_A\sqrt{(y^2 + (L_B - x)^2)}}\right)$$

$$\theta_B(x,y) = tan^{-1}\left(\frac{y}{L_B - x}\right)$$

$$\theta_1(x,y) = \pi - \theta_A(-x,y) - \theta_B(-x,y)$$

$$\theta_2(x,y) = \pi - \theta_A(x,y) - \theta_B(x,y) \quad (4.1)$$

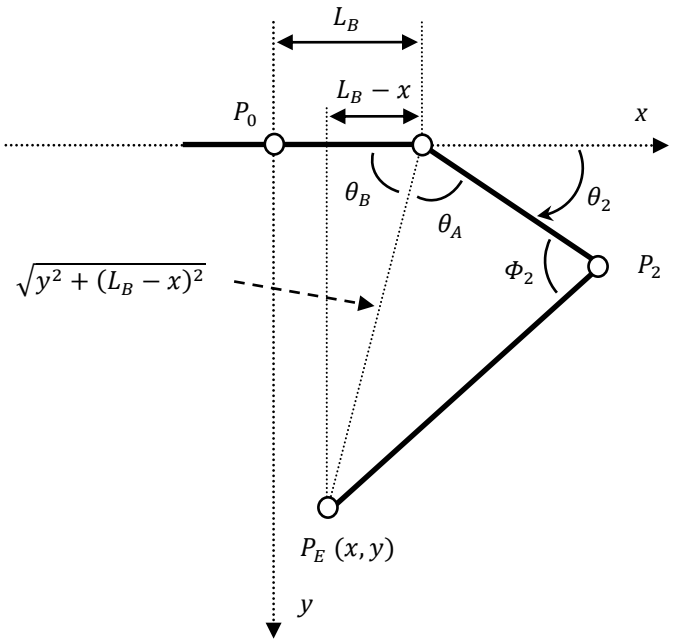

Figure 4-5: Inverse Kinematic

Gradient and Hessian of the inverse kinematic equation is necessary for dynamics formulation. Let $A = \sqrt{x^2 + y^2}$, and $Q_a = \frac{{L_A}^2 - {L_B}^2 - A^2}{\sqrt{4L_A A^2 - \left({L_A}^2 - {L_B}^2 - A^2\right)^2}}$. Gradient and Hessian are calculated for the right side system (θ_2), and then solutions for the left side system (θ_1) can be determined through symmetry.

$$\nabla\theta(x,y) = \frac{1}{A^2}\left(Q_a \begin{Bmatrix} L_B - x \\ -y \end{Bmatrix} + \begin{Bmatrix} L_B - x \\ y \end{Bmatrix}\right)^T$$

$$H_{11}(x,y) = -2\frac{L_B - x}{A^2}\left[\frac{\partial\theta_2}{\partial x} - \frac{Q_a(L_B - x)}{{L_A}^2 - {L_B}^2 - A^2}\left(1 + {Q_a}^2\frac{{L_A}^2 + {L_B}^2 - A^2}{{L_A}^2 - {L_B}^2 - A^2}\right)\right] - \frac{Q_a}{A^2}$$

$$H_{12}(x,y) = 2\frac{y}{A^2}\left[\frac{\partial\theta_2}{\partial x} - \frac{Q_a(L_B - x)}{{L_A}^2 - {L_B}^2 - A^2}\left(1 + {Q_a}^2\frac{{L_A}^2 + {L_B}^2 - A^2}{{L_A}^2 - {L_B}^2 - A^2}\right) - \frac{1}{2y}\right]$$

$$H_{22}(x,y) = 2\frac{y}{A^2}\left[\frac{\partial\theta_2}{\partial y} - \frac{Q_a y}{{L_A}^2 - {L_B}^2 - A^2}\left(1 + {Q_a}^2\frac{{L_A}^2 + {L_B}^2 - A^2}{{L_A}^2 - {L_B}^2 - A^2}\right)\right] - \frac{Q_a}{A^2}$$

$$\nabla\theta_1(x,y) = \nabla\theta(-x,y)$$

$$\nabla^2\theta_1(x,y) = \begin{bmatrix} H_{11}(-x,y) & H_{12}(-x,y) \\ H_{12}(-x,y) & H_{22}(-x,y) \end{bmatrix}$$

$$\nabla\theta_2(x,y) = \nabla\theta(x,y) \tag{4.2}$$

$$\nabla^2\theta_2(x,y) = \begin{bmatrix} H_{11}(x,y) & H_{12}(x,y) \\ H_{12}(x,y) & H_{22}(x,y) \end{bmatrix}$$

4.3 Dynamics Analysis

There is no way to simplify the robot model for dynamic analysis; the full 6-cable model must be used. The dynamics of a closed-loop parallel mechanism is typically complicated with several constraint equations. However, there are two specific goals in the dynamics formulation, and it is not necessary to obtain the complete set of dynamics equations. The first goal is to obtain expressions for tension in each cable given the spine force, acceleration, and velocity of the end-effector. The second goal is to use the cable tensions to calculate the required torque on the two motors. Equations for these two goals are used to calculate stiffness in Chapter 5 and perform optimization on the design parameters in Chapter 6.

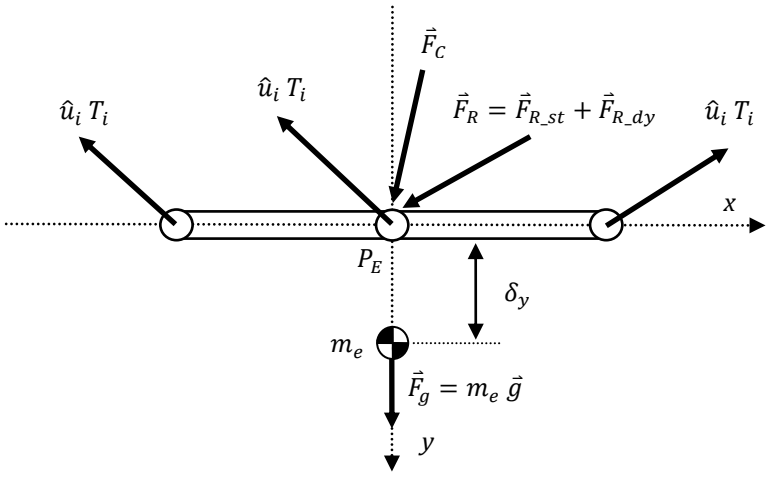

Figure 4-6: 2D Free-Body Diagram of the End-Effector

4.3.1 End-Effector Dynamics

Cable tensions can be calculated from dynamic equilibrium at the end-effector. Figure 4-6 shows the free-body diagram of the end-effector. Note that the acceleration due to gravity ($\vec{g}$) is positive downward. m_e is the mass of the end-effector including the payload. The center-of-mass for m_e is typically shifted to somewhere below the center of end-effector due to the payload. This offset is called "*eccentricity*", and it is represented by δ_y. For now, only eccentricity in the *y* direction is considered for simplicity, since it is trivial to add eccentricity in the other directions later. $\vec{F}_C$ is the constant spine force from the pneumatic cylinder. $\vec{F}_R$ is other forces applied to the end-effector from the pneumatic cylinder. This includes static force from weight of the cylinder ($\vec{F}_{R\_st}$), and dynamic reaction force ($\vec{F}_{R\_dy}$) from the cylinder. $\hat{u}_i$ is direction unit vector of *i*-th cable, and T_i is scalar value of tensile force of *i*-th cable. Multiplication of $\hat{u}_i$ and T_i represents the vector of tensile force for *i*-th cable. Let $\vec{X}$ be the position vector of the end-effector with (*x*, *y*) corresponding to the coordinate of P_E. Then $\ddot{\vec{X}}$ and $\dot{\vec{X}}$ represent acceleration and velocity of the end-effector respectively.

The following equation can be derived from Newton's second law:

$$\sum \hat{u}_i T_i + m_e\, \vec{g} + \vec{F}_C + \vec{F}_{R\_dy} + \vec{F}_{R\_st} = m_e\, \ddot{\vec{X}} \tag{4.3}$$

Rearranging the equation for cable tensions gives the following:

$$\sum \hat{u}_i T_i = m_e\, \ddot{\vec{X}} - \vec{F}_{R\_dy} - \vec{F}_{R\_st} - m_e\, \vec{g} - \vec{F}_C \tag{4.4}$$

Static force and dynamic force from the pneumatic cylinder ($\vec{F}_{R\_st}$ and $\vec{F}_{R\_dy}$) are the only unknown parameters in Equation (4.4). The next section examines the dynamic of the pneumatic cylinder to determine these unknown forces.

Now consider moments acting on the end-effector. Figure 4-7 shows a partial free-body diagram of the end-effector in 3D with some forces not shown. $\vec{r}_i$ is the distance vector of *i*-th cable connection from P_E (the center of the end-effector).

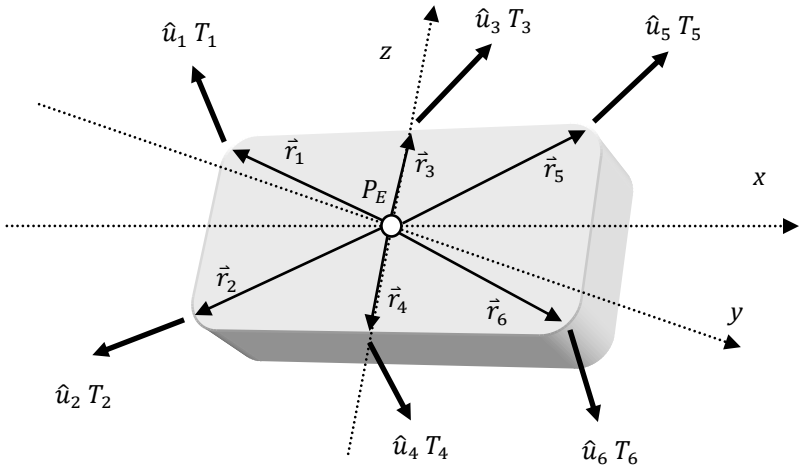

Figure 4-7: 3D Partial Free Body-Diagram of the End-Effector

The summation of moments at point P_E must be zero for the end-effector to maintain its rotational orientation. $\vec{F}_C$ and $\vec{F}_R$ are not shown in the free body diagram, and they do not cause moments on the end-effector since they passes through P_E. Then, moments on the end-effector are caused by cable tensions and eccentricity of the center-of-mass of m_e. Let $\vec{\delta}$ be a vector of eccentricity, or in other words the distance between the center-of-mass and P_E.

The summation of moments about P_E gives the following:

$$\sum \vec{r}_i \times (\hat{u}_i T_i) + \vec{\delta} \times \left(m_e \ddot{\vec{X}}\right) + \vec{\delta} \times (m_e \vec{g}) = 0 \tag{4.5}$$

Rearranging the equation for cable tensions gives the following:

$$\sum (\vec{r}_i \times \hat{u}_i)\, T_i = -\vec{\delta} \times \left(m_e \ddot{\vec{X}}\right) - \vec{\delta} \times (m_e \vec{g}) \tag{4.6}$$

4.3.2 Cylinder Dynamics

For analysis of the cylinder dynamics, a new coordinate frame that is attached to the pneumatic cylinder is defined and shown in Figure 4-8. $\hat{e}_x$ and $\hat{e}_y$ are unit vectors for the global coordinate frame used to define position of the end-effector. $\hat{e}_a$ is a unit vector for the axial (longitudinal) direction of the cylinder, and $\hat{e}_r$ is a unit vector normal to the axial direction of the cylinder. γ is the angle that the cylinder makes with the vertical axis ($\hat{e}_y$), it is positive in the CCW direction.

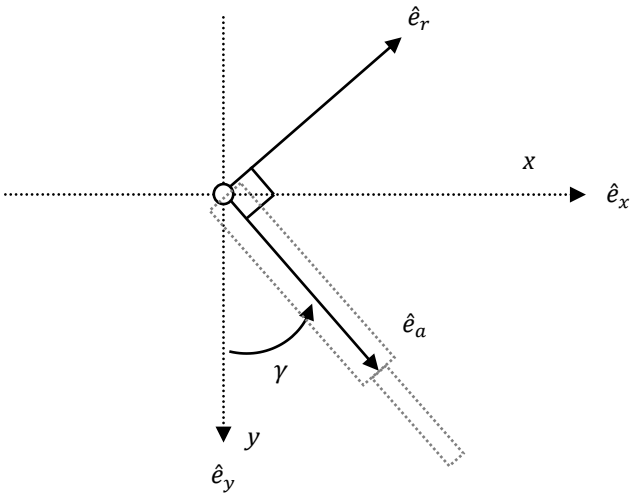

Figure 4-8: Coordinate Frame of the Pneumatic Cylinder

The pneumatic cylinder is divided into two sections. The upper body is called "*cylinder base*" and it is represented by the subscript "*cy*". The lower body is called "*piston*" and it is represented by the subscript "*p*". Parameters for the cylinder base and piston are listed in the next page along with a diagram of the entire cylinder shown in Figure 4-9.

Parameters

P_1: coordinate of connection between the cylinder and fixed base, equivalent to P_0

P_2: coordinate of contact point between the cylinder body and piston

P_3: coordinate of connection between the cylinder and end-effector, equivalent to P_E

m_{cy}: mass of the cylinder body

m_p: mass of the piston

L_{cy}: half the length of the cylinder body (distance to the center-of-mass)

L_p: half the length of the piston (distance to the center-of-mass)

R: current total length of the entire pneumatic cylinder

r_i: distance from P_1 to P_2

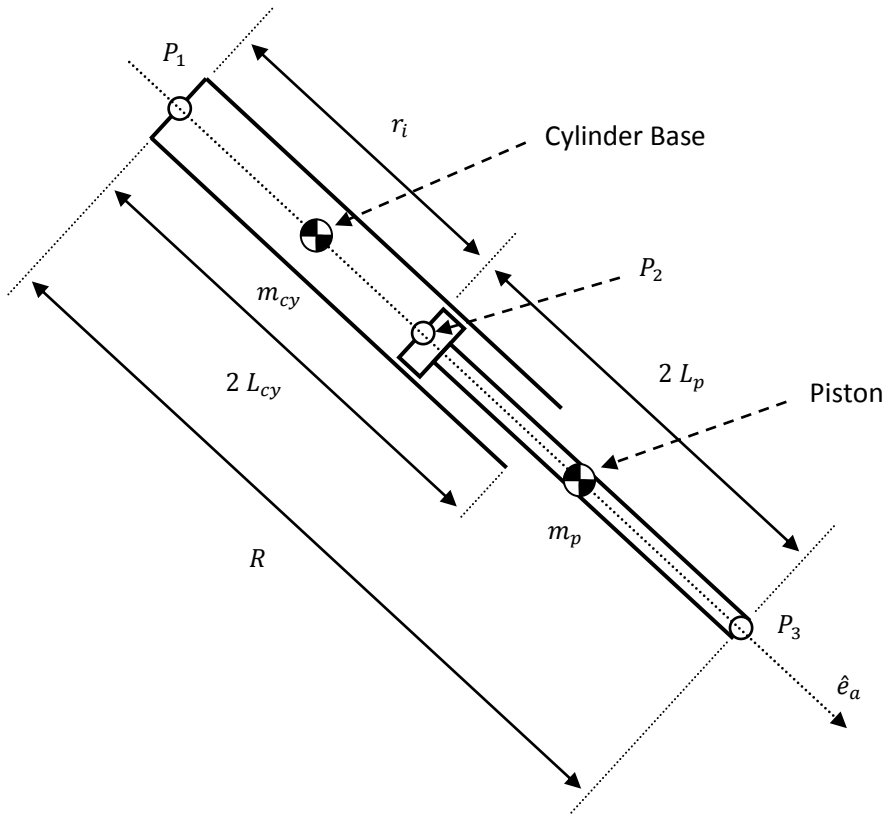

Figure 4-9: Parameters for the Pneumatic Cylinder

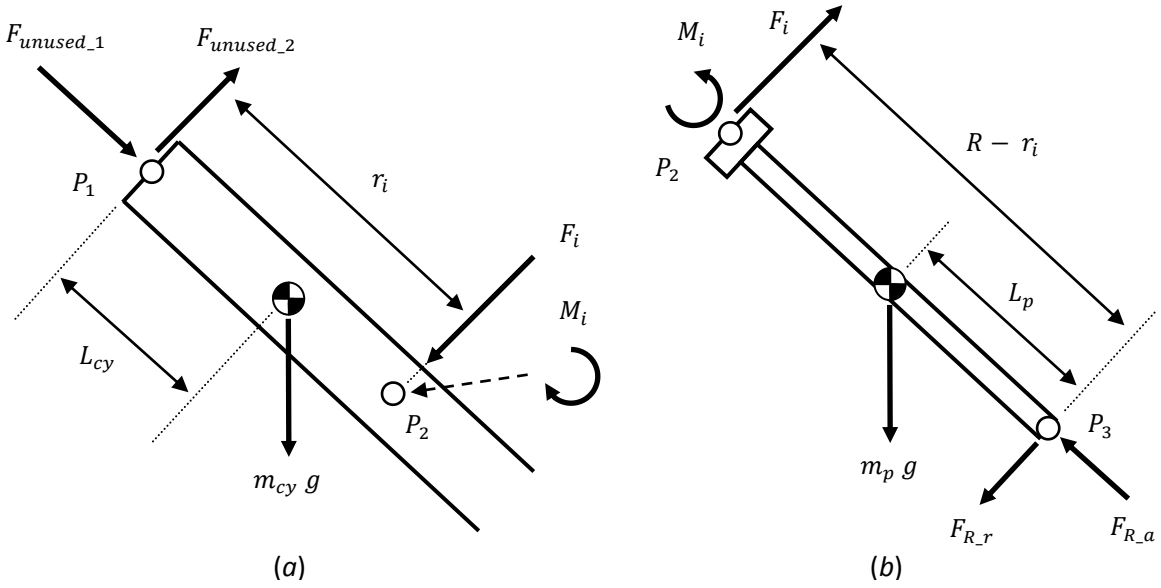

Figure 4-10: Free-Body Diagrams of the Pneumatic Cylinder

Figure 4-10 (*a*) and (*b*) shows free-body diagrams of the cylinder body and piston respectively. F_i and M_i are internal reaction force and internal reaction moment between the cylinder body and piston. F_{R_a} and F_{R_r} are axial and radial components of the reaction force from the end-effector. Sum of F_{R_a} and F_{R_r} equals to the negative value of $\vec{F}_R$ mentioned in the end-effector dynamic section. Reaction forces from the fixed base at P_1 are not necessary for this analysis.

First consider static component of the reaction force. The sum of moments at P_1 and P_3 are zero since they are universal joints. Taking moments at these points and isolating for the internal reaction moment, M_i , gives the following:

$$M_i = F_i\, r_i + m_{cy}\, g\, L_{cy}\ sin(\gamma) \tag{4.7}$$

$$M_i = -F_i\, (R - r_i) + m_p\, g\, L_p\ sin(\gamma) \tag{4.8}$$

Combining the two equations above and isolating for the internal reaction force F_i gives:

$$F_i = \left(m_p\, L_p - m_{cy}\, L_{cy}\right) \frac{g\ sin\,(\gamma)}{R} \tag{4.9}$$

Then, the expression for the static component of F_{R_a} and F_{R_r} can be obtained from the sum of forces on the piston. Let $F_{R\_a\_st}$ and $F_{R\_r\_st}$ be the static component of F_{R_a} and F_{R_r}, respectively. They can be expressed as shown in Equation (4.10), where the subscript *" cf "* on F_{R_st} means that it is expressed in the local coordinate frame of the pneumatic cylinder in terms of R and γ.

$$\vec{F}_{R\_st\_cf} = \begin{Bmatrix} F_{R\_a\_st} \\ F_{R\_r\_st} \end{Bmatrix} = \begin{Bmatrix} m_p\, g\, cos(\gamma) \\ F_i - m_p\, g\, sin(\gamma) \end{Bmatrix} \tag{4.10}$$

Let I_{cy} be inertia of the cylinder body and I_p be inertia of the piston. Equivalent inertia of the entire pneumatic cylinder at P_1 is:

$$I_{eq} = I_{cy} + I_p + m_p \left(R - L_p\right)^2 \tag{4.11}$$

Let $F_{R\_a\_dy}$ be the dynamic component of F_{R_a}. Dynamic forces acting on the piston in the axial direction are linear acceleration and centrifugal acceleration of the piston. The sum of these two forces equal the total dynamic force in the axial direction:

$$m_p\, \ddot{R} - m_p\, \dot{\gamma}^2 \left(R - L_p\right) = -\, F_{R\_a\_dy} \tag{4.12}$$

Let $F_{R\_r\_dy}$ be the dynamic component of F_{R_r}. There are forces in the radial direction due to tangential acceleration and Coriolis effect. The sum of Moments at P_1 equals to the moment caused by dynamic force in the radial direction:

$$I_{eq}\, \ddot{\gamma} + 2\, m_p \left(R - L_p\right) \dot{R}\, \dot{\gamma} = -\, R\, F_{R\_r\_dy} \tag{4.13}$$

Equations (4.12) and (4.13) can be written in a matrix form representing a standard dynamics equation.

$$\begin{bmatrix} m_p & 0 \\ 0 & I_{eq} \end{bmatrix} \begin{Bmatrix} \ddot{R} \\ \ddot{\gamma} \end{Bmatrix} + \{\dot{R}\ \ \dot{\gamma}\} \left\{ \begin{bmatrix} 0 & 0 \\ 0 & -\left(m_p \left(R - L_p\right)\right) \end{bmatrix} \right\} \begin{Bmatrix} \dot{R} \\ \dot{\gamma} \end{Bmatrix} = \begin{bmatrix} -1 & 0 \\ 0 & -R \end{bmatrix} \begin{Bmatrix} F_{R\_a\_dy} \\ F_{R\_r\_dy} \end{Bmatrix} \tag{4.14}$$

Let $\vec{F}_{R\_dy\_cf}$ represent a vector of dynamic force expressed in the local coordinate frame of the cylinder in terms of R and γ. Simplifying Equation (4.14) and rearranging for $\vec{F}_{R\_dy\_cf}$ gives the following:

$$[M_{cf}]\,\ddot{\vec{X}}_{cf} + \dot{\vec{X}}_{cf}^{\,T}\,[C_{cf}]\,\dot{\vec{X}}_{cf} = [K_{cf}]\,\vec{F}_{R\_dy\_cf} \tag{4.15}$$

$$\vec{F}_{R\_dy\_cf} = [K_{cf}]^{-1}\,[M_{cf}]\,\ddot{\vec{X}}_{cf} + [K_{cf}]^{-1}\,\dot{\vec{X}}_{cf}^{\,T}\,[C_{cf}]\,\dot{\vec{X}}_{cf} \tag{4.16}$$

$\ddot{\vec{X}}_{cf}$ and $\dot{\vec{X}}_{cf}$ are acceleration and velocity vectors in terms of R and γ. $[M_{cf}]$ is a mass inertia matrix. $[C_{cf}]$ is a three dimensional Christoffel symbol. $[K_{cf}]$ is a constant coefficient matrix.

4.3.3 Coordinate Transformation

In the previous section, expressions for static and dynamic components of the reaction force, $\vec{F}_{R\_st}$ and $\vec{F}_{R\_dy}$, are found for the local coordinate frame of the pneumatic cylinder in terms of R and γ. It is necessary to apply coordinate transformations to these expressions before it can be substituted back into the end-effector dynamics equation shown in Equation (4.4).

Let $[R_{rot}]$ represent the rotation matrix between the pneumatic cylinder coordinate frame and end-effector global coordinate frame described in Figure 4-8.

$$\begin{Bmatrix}\hat{e}_r\\ \hat{e}_a\end{Bmatrix} = [R_{rot}]\begin{Bmatrix}\hat{e}_x\\ \hat{e}_y\end{Bmatrix} \tag{4.17}$$

$$[\mathrm{R_{rot}}] = \begin{bmatrix}\cos(\gamma) & -\sin(\gamma)\\ \sin(\gamma) & \cos(\gamma)\end{bmatrix} \tag{4.18}$$

The geometrical relationship between (R, γ) and (x, y) are:

$$R = \sqrt{x^2 + y^2} \tag{4.19}$$

$$\gamma = tan^{-1}\left(\frac{y}{x}\right) \tag{4.20}$$

Let $[J_{cf}]$ and $[H_{cf}]$ be Jacobian and Hessian matrices for this relationship respectively.

$$[J_{cf}] = \begin{bmatrix} \frac{\partial R}{\partial x} & \frac{\partial R}{\partial y} \\ \frac{\partial \gamma}{\partial x} & \frac{\partial \gamma}{\partial y} \end{bmatrix} = \begin{bmatrix} \frac{x}{R} & \frac{y}{R} \\ \frac{y}{R^2} & -\frac{x}{R^2} \end{bmatrix} \tag{4.21}$$

$$[H_{cf}] = \left\{ \begin{bmatrix} \frac{\partial^2 R}{\partial x^2} & \frac{\partial^2 R}{\partial x \partial y} \\ \frac{\partial^2 R}{\partial x \partial y} & \frac{\partial^2 R}{\partial y^2} \end{bmatrix} \right\} = \left\{ \begin{bmatrix} \frac{y^2}{R^3} & -\frac{x\,y}{R^3} \\ -\frac{x\,y}{R^3} & \frac{x^2}{R^3} \end{bmatrix} \right\} \left\{ \begin{bmatrix} -\frac{2\,x\,y}{R^4} & \frac{x^2 - y^2}{R^4} \\ \frac{x^2 - y^2}{R^4} & \frac{2\,x\,y}{R^4} \end{bmatrix} \right\} \tag{4.22}$$

Let $\vec{X}$ be the coordinate defined by (x, y), and let $\vec{X}_{cy}$ be coordinate defined by (R, γ). Then, the transformation for velocity and acceleration between the two coordinate frames are as following:

$$\dot{\vec{X}}_{cf} = [J_{cf}]\dot{\vec{X}} \tag{4.23}$$

$$\ddot{\vec{X}}_{cf} = [J_{cf}]\ddot{\vec{X}} + \dot{\vec{X}}^T [H_{cf}] \dot{\vec{X}} \tag{4.24}$$

Now $\vec{F}_{R\_st}$ and $\vec{F}_{R\_dy}$ can be expressed in the end-effector global frame. A negative sign is added since the direction of reaction force acting on the end-effector is opposite from the direction of reaction force acting on the piston.

$$\vec{F}_{R\_st} = -[R_{rot}]^T \vec{F}_{R\_st\_cf} \tag{4.25}$$

$$\vec{F}_{R\_dy} = -\left[\left([R_{rot}]^T [K_{cf}]^{-1} [M_{cf}] \right) \ddot{\vec{X}} + \dot{\vec{X}}^T \left([R_{rot}]^T [K_{cf}]^{-1} \left[[J_{cf}]^T [C_{cf}][J_{cf}] + [M_{cf}][H_{cf}] \right] \right) \dot{\vec{X}} \right] \tag{4.26}$$

Equation (4.26) is simplified using $[M_C]$ and $[C_C]$ to substitute for equivalent mass inertia matrix and Christoffel symbol of the cylinder reaction force in the end-effector global frame.

$$[M_C] = \left([R_{rot}]^T \left[K_{cf}\right]^{-1}[M_{cf}]\right) \tag{4.27}$$

$$[C_C] = \left([R_{rot}]^T \left[K_{cf}\right]^{-1}\left[\left[J_{cf}\right]^T[C_{cf}][J_{cf}] + [M_{cf}][H_{cf}]\right]\right) \tag{4.28}$$

$$\vec{F}_{R\_dy} = -\left[\left[M_C\right]\ddot{\vec{X}} + \dot{\vec{X}}^T[C_C]\dot{\vec{X}}\right] \tag{4.29}$$

4.3.4 Expression for Cable Tension

Recall the dynamics equation of the end-effector from Equation (4.4). Substituting $\vec{F}_{R\_st}$ and $\vec{F}_{R\_dy}$ from Equations (4.25) and (4.29) gives:

$$\sum \hat{u}_i T_i = m_e \ddot{\vec{X}} + \left[M_C\right]\ddot{\vec{X}} + \dot{\vec{X}}^T[C_C]\dot{\vec{X}} + \left[R_{rot}{}^T\right]\vec{F}_{R\_st\_cf} - m_e \vec{g} - \vec{F}_C \tag{4.29}$$

Expression for forces from Equation (4.29) and expression for moments from Equation (4.6) can be written together in a single matrix expression. Let $[A]$ be a 6 x 6 matrix with columns representing $\hat{u}_i$ and $\vec{r}_i \times \hat{u}_i$ for each cable. Let $\vec{T}$ be a 6 x 1 vector representing scalar values of cable tensions.

$$[A] = \begin{bmatrix} \left\{\hat{u}_1\right\} & \left\{\hat{u}_2\right\} & \cdots & \left\{\hat{u}_6\right\} \\ \left\{\vec{r}_1 \times \hat{u}_1\right\} & \left\{\vec{r}_2 \times \hat{u}_2\right\} & \cdots & \left\{\vec{r}_6 \times \hat{u}_6\right\} \end{bmatrix} \tag{4.30}$$

$$\vec{T} = \{\ T_1\ \ T_2\ \ T_3\ \ T_4\ \ T_5\ \ T_6\ \}^T \tag{4.31}$$

$$[A]\,\vec{T} = \begin{Bmatrix} F_x \\ F_y \\ F_z \\ M_x \\ M_y \\ M_z \end{Bmatrix} = [M]\,\ddot{\vec{X}} + \dot{\vec{X}}^T[C]\,\dot{\vec{X}} + \vec{B} \tag{4.32}$$

$\ddot{\vec{X}}$ is 2 x 1 acceleration vector of the end-effector consisting of $\{ \ddot{x} \quad \ddot{y} \}^T$, and $\dot{\vec{X}}$ is 2 x 1 velocity vector of the end-effector consisting of $\{ \dot{x} \quad \dot{y} \}^T$.

$[M]$ is a 6 x 2 matrix with mass and inertia parameters. It has the end-effector mass component with m_e and acceleration dynamic force component ($[M_C]$) from the pneumatic cylinder. Since the dimension of $[M_C]$ is 2 x 2 with components in F_x and F_y, a 4 x 2 zero matrix is appended to make it a 6 x 2 matrix.

$$[M] = m_e \begin{bmatrix} 1 & 0 \\ 0 & 1 \\ 0 & 0 \\ 0 & \delta_z \\ -\delta_z & 0 \\ \delta_y & -\delta_x \end{bmatrix} + \begin{bmatrix} \begin{bmatrix} & M_C & \end{bmatrix} \\ 0 & 0 \\ 0 & 0 \\ 0 & 0 \\ 0 & 0 \end{bmatrix}$$

$[C]$ is a three dimensional 2 x 2 x 6 Christoffel symbol matrix that comes directly from velocity dynamic force component ($[C_C]$) from the pneumatic cylinder. Since the dimension of $[C_C]$ is 2 x 2 x 2 with components in F_x and F_y, zero matrices are also appended here as well.

$$[C] = \begin{Bmatrix} \begin{bmatrix} \begin{bmatrix} C_{c\,(1,:,:)} \end{bmatrix} & 0 & 0 & 0 & 0 \\ 0 & 0 & 0 & 0 & 0 \end{bmatrix} \\ \begin{bmatrix} \begin{bmatrix} C_{c\,(2,:,:)} \end{bmatrix} & 0 & 0 & 0 & 0 \\ 0 & 0 & 0 & 0 & 0 \end{bmatrix} \end{Bmatrix}$$

B is a 6 x 1 matrix that represents static component of forces and moments from the constant spine force and masses of the end-effector and pneumatic cylinder. Subscripts "*x*" and "*y*" on F_C and $\left({R_{rot}}^T \vec{F}_{R\_st\_cf}\right)$ represents *x* and *y* components of the forces respectively.

$$[B] = -\begin{Bmatrix} \vec{F}_{C_x} + \left([R_{rot}]^T \vec{F}_{R\_st\_cf}\right)_x \\ \vec{F}_{C_y} + \left([R_{rot}]^T \vec{F}_{R\_st\_cf}\right)_y + m_e \vec{g}_y \\ 0 \\ \delta_z \, m_e \vec{g}_y \\ 0 \\ -\delta_x \, m_e \vec{g}_y \end{Bmatrix}$$

Finally, the tension for each cable can be obtained by multiplying the inverse of matrix A on both sides of Equation (4.32).

$$\vec{T} = [A]^{-1}\left([M]\,\ddot{\vec{X}} + \dot{\vec{X}}^{T}[C]\,\dot{\vec{X}} + \vec{B}\right) \tag{4.36}$$

4.3.5 Expression for Actuator Torque

Now that the expression for cable tensions is available, the actuator torque can be calculated. Consider the free-body diagram of the left side arm shown in Figure 4-11.

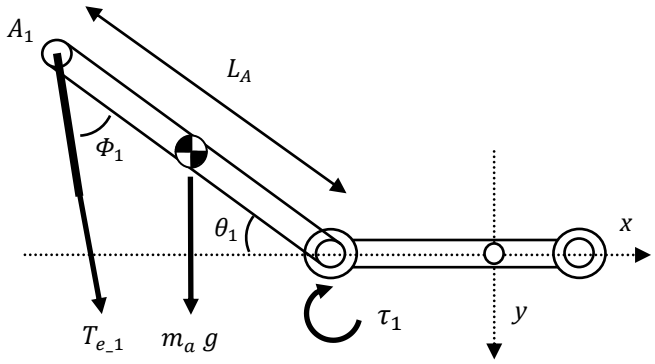

Figure 4-11: Free-Body Diagram of Left Side Arm

T_{e_1} is the effective tension acting on the left arm that comes from the vector summation of T_1 and T_2. Φ_1 is the angle between the arm and cable, which can be calculated from inverse kinematics. m_a is mass of the arm, and I_a is the inertia of the arm. The expression for left side actuator torque (τ_1) can be obtained from a moment balance at the joint between the fixed base and left arm.

$$\tau_1 = \frac{1}{2} L_A\, m_a g\, \cos(\theta_1) - I_a \ddot{\theta}_1 + T_{e1}\, L_A\, sin(\Phi_1) \tag{4.37}$$

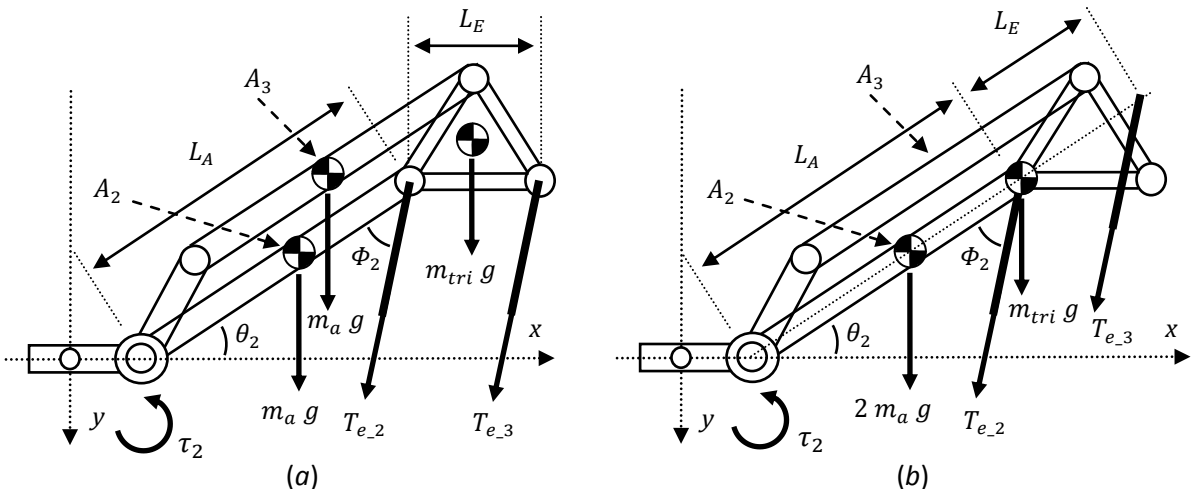

Figure 4-12: Free Body Diagram of Right Side Arms

Now, consider the free body diagram of the right side arms shown in Figure 4-12 a). T_{e_2} is the effective tension that comes from vector summation of T_3 and T_4. T_{e_3} is the effective tension that comes from vector summation of T_5 and T_6. m_{tri} the is mass of the triangle structure. In order to simplify the calculation for actuator torque, some simplifications are made to the structure as shown in Figure 4-12 b). Arm A_3 is moved to the same location as arm A_2 so that their center-of-mass coincide. The center-of-mass of the triangle is moved to the end of arm A_2. Tension T_{e3} is moved to a point L_E away from the end of arm A_2 in the direction parallel to A_2. Finally, expression for right side actuator torque (τ_2) is:

$$\tau_2 \;=\; 2\left(\frac{1}{2}L_A\, m_a g\, \cos(\theta_2)\right) - \left(2I_a + m_{tri}\, {L_A}^2\right)\ddot{\theta}_2 + L_A\, T_{e2}\, sin(\Phi_2) + (L_A + L_E)\, T_{e3}\, sin(\Phi_2) \tag{4.38}$$

$\ddot{\theta}$ is calculated from the Gradient ($\nabla\theta$) and Hessian ($\nabla^2\theta$) of θ found in Equations (4.1) and (4.2) in the inverse kinematic section as shown below:

$$\ddot{\theta} \;= [\nabla^2\theta(x,y)]\,\vec{\ddot{X}} + \vec{\dot{X}}^{\,T}\,[\nabla\theta(x,y)]\,\vec{\dot{X}} \tag{4.39}$$

where (x, y) is position of the end-effector, $\vec{\ddot{X}}$ is acceleration vector of the end-effector, and $\vec{\dot{X}}$ is velocity vector of the end-effector.

Chapter 5

Stiffness Analysis

5.1 Introduction of Stiffness in Cable-Based Manipulator

Chapter 3 discussed concept and importance of tensionability and tensionable configuration in cable-based manipulator design. In Chapter 4, equations for calculating cable tensions are formulated, which can be used to verify tensionability. However, tensionability does not guarantee good stiffness, and a cable-based mechanism has an inherent disadvantage in stiffness due to lack of lateral and torsional stiffness on cables compared to rigid links. Therefore, stiffness analysis on a cable-based manipulator is just as important as tensionability analysis. In the case of the new proposed manipulator design, stiffness analysis is especially important for minimizing out-of-plane motion.

There has been a great deal of research on the topic of stiffness of parallel mechanisms. However, few have studied stiffness of cable-based mechanisms. Khajepour and Behzadipour studied 3D cable-based delta design and developed basis for stiffness analysis of cable-based manipulators [29]. This thesis proposes a slightly different method to formulate the stiffness matrix compared to their work, which may be easier to understand. In the end, the stiffness matrix formulated in this thesis is equivalent to the stiffness matrix formulated by in [29] and Behzadipour's thesis [2]. In addition to formulating the stiffness matrix, this thesis discusses a valid range for stiffness calculation, an estimation method, and analysis comparing stiffness of different cable configurations.

5.2 Formulation of Stiffness Matrix

5.2.1 Definition of Stiffness Matrix

Stiffness is defined as resistance of an elastic body to deformation by an applied force. It is typically expressed in the following form:

$$\text{stiffness} = k = \frac{F}{\Delta l}$$

F is the force applied to the body, and Δl is the displacement of the body. Another way to interpret stiffness is the amount of force required to move a body per unit length. Let $\overrightarrow{W}$ be external forces and moments applied to the end-effector, and let $\vec{\delta}$ represent the change in position and orientation of the end-effector.

$$\overrightarrow{W} = (\ F_x \quad F_y \quad F_z \quad M_x \quad M_y \quad M_z\ )^T$$

$$\vec{\delta} = (\ \delta_x \quad \delta_y \quad \delta_z \quad \theta_x \quad \theta_y \quad \theta_z\ )^T$$

Now consider a free-body diagram of a conceptual end-effector under a static case shown in Figure 5-1. Stiffness analysis in this thesis is strictly for static forces, therefore dynamic forces are not considered.

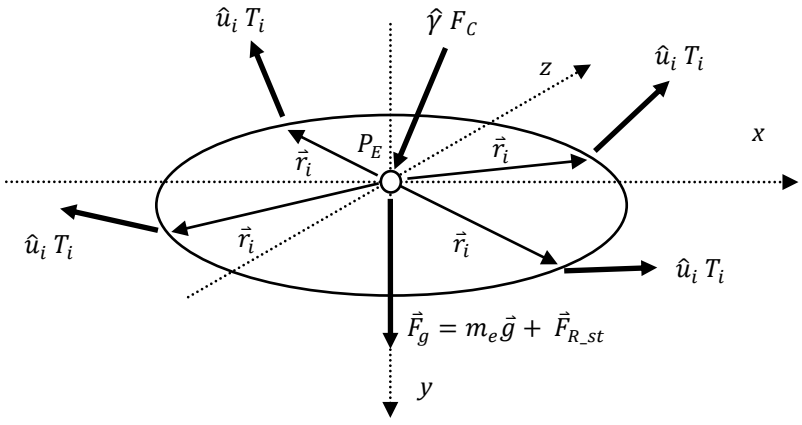

Figure 5-1: Free Body Diagram of a Conceptual End-Effector

$\vec{F}_g$ represents the static force from masses of the pneumatic cylinder and end-effector due to gravity. $\hat{u}_i$ is the unit vector of *i*-th cables, $\vec{r}_i$ is the distance vector of *i*-th cable connection from the center of the end-effector to the *i*-th cable connection. T_i is the scalar value of tension in *i*-th cable. $\hat{\gamma}$ is the unit vector of the scalar spine force, F_C. Note that $\hat{u}$ points outward from the end-effector, while $\hat{\gamma}$ points toward the end-effector. This convention is used to keep the scalar values of T_i and F_C positive.

Let $[A]$ be a 6 x 6 matrix with columns representing $\hat{u}_i$ and $\vec{r}_i \times \hat{u}_i$ for each cable. Let $\vec{T}$ be a 6 x 1 vector representing scalar values of cable tensions. $[A]$ and $\vec{T}$ are equivalent to the matrix and vector introduced in Equation (4.30) and (4.31) in Section 4.3.4. They are shown again here for clarity:

$$[A] = \begin{bmatrix} \begin{Bmatrix} \hat{u}_1 \end{Bmatrix} & \begin{Bmatrix} \hat{u}_2 \end{Bmatrix} & \cdots & \begin{Bmatrix} \hat{u}_6 \end{Bmatrix} \\ \begin{Bmatrix} \vec{r}_1 \times \hat{u}_1 \end{Bmatrix} & \begin{Bmatrix} \vec{r}_2 \times \hat{u}_2 \end{Bmatrix} & \cdots & \begin{Bmatrix} \vec{r}_6 \times \hat{u}_6 \end{Bmatrix} \end{bmatrix}$$

$$\vec{T} = \{ \; T_1 \;\; T_2 \;\; T_3 \;\; T_4 \;\; T_5 \;\; T_6 \; \}^T$$

The sum of forces and moments on the end-effector is zero at the equilibrium. Rearranging for the applied forces and moments ($\overrightarrow{W}$) gives the following equation:

$$[A]\,\vec{T} + \hat{\gamma}\,F_C + \vec{F}_g + \overrightarrow{W} = 0 \tag{5.1}$$

$$\overrightarrow{W} = -\left([A]\,\vec{T} + \hat{\gamma}\,\vec{F}_C + \vec{F}_g\right) \tag{5.2}$$

Taking the derivative of both sides of Equation (5.2) with respect to $\vec{\delta}$ gives:

$$\frac{\partial \overrightarrow{W}}{\partial \vec{\delta}} = -\frac{\partial}{\partial \vec{\delta}}\left([A]\,\vec{T} + \hat{\gamma}\,\vec{F}_C + \vec{F}_g\right) \tag{5.3}$$

The left side of Equation (5.3) is in the form of $\frac{F}{\Delta l}$, and therefore this equation represents stiffness of the end-effector. $\vec{F}_g$ can be eliminated from this partial derivative because direction and magnitude of $\vec{F}_g$ do

not change with respect to $\vec{\delta}$. Now, taking a closer look at the remaining terms, $[A]$ and $\hat{\gamma}$ are unit vectors of cables and pneumatic cylinder which are affected by $\vec{\delta}$. $\vec{F}_C$ is the constant spine force, and its magnitude does not change with respect to $\vec{\delta}$. $\vec{T}$ is a vector of cable tensions, and it is affected by $\vec{\delta}$ due to changes in the length of cables. The cables are modeled as linear springs with a very high spring constant (k) as shown:

$$T^* = T + k\,(L^* - L) \tag{5.4}$$

in Equation (5.4). T^* is the final tension on the cable after the end-effector is moved by $\vec{\delta}$. T is the unstretched pre-tension on the cable. L^* and L are the final length and unstretched length of the cable respectively.

Since $[A]$ and $\hat{\gamma}$ are both direction unit vectors, and $\vec{T}$ and F_C are both scalar values of forces, it is possible to group them together and simplify the right side of Equation (5.3) as follows:

$$-\frac{\partial}{\partial\vec{\delta}}\left([A]\,\vec{T} + \hat{\gamma}\,F_C\right) = -\frac{\partial}{\partial\vec{\delta}}\left(\begin{bmatrix}[A] & \hat{\gamma}\end{bmatrix}\begin{bmatrix}\vec{T}\\ F_C\end{bmatrix}\right) = -\frac{\partial}{\partial\vec{\delta}}\left(\begin{bmatrix}\hat{u}_1 & \hat{u}_2 & \cdots & \hat{\gamma}\\ \vec{r}_1\times\hat{u}_1 & \vec{r}_2\times\hat{u}_2 & \cdots & 0\end{bmatrix}\begin{bmatrix}T_1\\ T_2\\ \vdots\\ F_C\end{bmatrix}\right) \tag{5.5}$$

It is possible to treat the spine force with $\hat{\gamma}$ and F_C as one of the cables with unit vector $\hat{u}_7$ and tension T_7. $\vec{r}_7$ is zero since $\hat{u}_7$ goes into the center of the end-effector. Stiffness of the pneumatic cylinder is zero since it is connected to a constant pressure, therefore k in Equation (5.4) is zero for T_7.

Equation (5.5) can be rewritten in a summation form:

$$-\sum_{i=1}^{7}\frac{\partial}{\partial\vec{\delta}}\begin{bmatrix}\hat{u}_i\,T_i\\ (\vec{r}_i\times\hat{u}_i)\,T_i\end{bmatrix} = -\sum_{i=1}^{7}\frac{\partial}{\partial\vec{\delta}}\begin{bmatrix}\hat{u}_{i\_x}\,T_i\\ \hat{u}_{i\_y}\,T_i\\ \hat{u}_{i\_z}\,T_i\\ (\vec{r}_i\times\hat{u}_i)_x\,T_i\\ (\vec{r}_i\times\hat{u}_i)_y\,T_i\\ (\vec{r}_i\times\hat{u}_i)_z\,T_i\end{bmatrix} \tag{5.6}$$

Finally, the stiffness matrix $[K]$ of the end-effector becomes:

$$[K] = \frac{\partial W}{\partial \vec{\delta}} = -\begin{bmatrix} \frac{\partial F_x}{\partial \delta_x} & \frac{\partial F_x}{\partial \delta_y} & \frac{\partial F_x}{\partial \delta_z} & \frac{\partial F_x}{\partial \theta_x} & \frac{\partial F_x}{\partial \theta_y} & \frac{\partial F_x}{\partial \theta_z} \\ \frac{\partial F_y}{\partial \delta_x} & \frac{\partial F_y}{\partial \delta_y} & \frac{\partial F_y}{\partial \delta_z} & \frac{\partial F_y}{\partial \theta_x} & \frac{\partial F_y}{\partial \theta_y} & \frac{\partial F_y}{\partial \theta_z} \\ \frac{\partial F_z}{\partial \delta_x} & \frac{\partial F_z}{\partial \delta_y} & \frac{\partial F_z}{\partial \delta_z} & \frac{\partial F_z}{\partial \theta_x} & \frac{\partial F_z}{\partial \theta_y} & \frac{\partial F_z}{\partial \theta_z} \\ \frac{\partial M_x}{\partial \delta_x} & \frac{\partial M_x}{\partial \delta_y} & \frac{\partial M_x}{\partial \delta_z} & \frac{\partial M_x}{\partial \theta_x} & \frac{\partial M_x}{\partial \theta_y} & \frac{\partial M_x}{\partial \theta_z} \\ \frac{\partial M_y}{\partial \delta_x} & \frac{\partial M_y}{\partial \delta_y} & \frac{\partial M_y}{\partial \delta_z} & \frac{\partial M_y}{\partial \theta_x} & \frac{\partial M_y}{\partial \theta_y} & \frac{\partial M_y}{\partial \theta_z} \\ \frac{\partial M_z}{\partial \delta_x} & \frac{\partial M_z}{\partial \delta_y} & \frac{\partial M_z}{\partial \delta_z} & \frac{\partial M_z}{\partial \theta_x} & \frac{\partial M_z}{\partial \theta_y} & \frac{\partial M_z}{\partial \theta_z} \end{bmatrix} = -\sum_{i=1}^{7} \begin{bmatrix} \frac{\partial(\hat{u}_{i\_x}\, T_i)}{\partial \delta_x} & \frac{\partial(\hat{u}_{i\_x}\, T_i)}{\partial \delta_y} & \cdots & \frac{\partial(\hat{u}_{i\_x}\, T_i)}{\partial \theta_z} \\ \frac{\partial(\hat{u}_{i\_y}\, T_i)}{\partial \delta_x} & \frac{\partial(\hat{u}_{i\_y}\, T_i)}{\partial \delta_y} & \cdots & \frac{\partial(\hat{u}_{i\_y}\, T_i)}{\partial \theta_z} \\ \frac{\partial(\hat{u}_{i\_z}\, T_i)}{\partial \delta_x} & \frac{\partial(\hat{u}_{i\_z}\, T_i)}{\partial \delta_y} & \cdots & \frac{\partial(\hat{u}_{i\_z}\, T_i)}{\partial \theta_z} \\ \frac{\partial((\vec{r}_i \times \hat{u}_i)_x\, T_i)}{\partial \delta_x} & \frac{\partial((\vec{r}_i \times \hat{u}_i)_x\, T_i)}{\partial \delta_y} & \cdots & \frac{\partial((\vec{r}_i \times \hat{u}_i)_x\, T_i)}{\partial \theta_z} \\ \frac{\partial((\vec{r}_i \times \hat{u}_i)_y\, T_i)}{\partial \delta_x} & \frac{\partial((\vec{r}_i \times \hat{u}_i)_y\, T_i)}{\partial \delta_y} & \cdots & \frac{\partial((\vec{r}_i \times \hat{u}_i)_y\, T_i)}{\partial \theta_z} \\ \frac{\partial((\vec{r}_i \times \hat{u}_i)_z\, T_i)}{\partial \delta_x} & \frac{\partial((\vec{r}_i \times \hat{u}_i)_z\, T_i)}{\partial \delta_y} & \cdots & \frac{\partial((\vec{r}_i \times \hat{u}_i)_z\, T_i)}{\partial \theta_z} \end{bmatrix} \tag{5.7}$$

Now, consider each term in the stiffness matrix. Ignore the summation on the right side of Equation (5.7) and consider one cable at a time. Let $\vec{\delta}_d$ represent displacement part of $\vec{\delta}$ with ($\delta_x\ \delta_y\ \delta_z$), and let $\vec{\delta}_r$ represent rotation part of $\vec{\delta}$ with ($\theta_x\ \theta_y\ \theta_z$). Then, the stiffness matrix can be divided into four quadrants:

$$[\mathrm{K}] = -\begin{bmatrix} \frac{\partial F}{\partial \vec{\delta}_d} & \frac{\partial F}{\partial \vec{\delta}_r} \\ \frac{\partial M}{\partial \vec{\delta}_d} & \frac{\partial M}{\partial \vec{\delta}_r} \end{bmatrix} = \begin{bmatrix} -\frac{\partial(\hat{u}\, T)}{\partial \vec{\delta}_d} & -\frac{\partial(\hat{u}\, T)}{\partial \vec{\delta}_r} \\ -\frac{\partial((\vec{r} \times \hat{u})\, T)}{\partial \vec{\delta}_d} & -\frac{\partial((\vec{r} \times \hat{u})\, T)}{\partial \vec{\delta}_r} \end{bmatrix} = \begin{bmatrix} \text{quadrant 1} & \text{quadrant 2} \\ \text{quadrant 3} & \text{quadrant 4} \end{bmatrix} \tag{5.8}$$

Quadrant 1 represents translational stiffness of the end-effector. Quadrant 4 represents rotational stiffness of the end-effector. Quadrants 2 and 3 represent the coupling effect between translational stiffness and rotational stiffness. In order to keep the calculation manageable, it is best to consider one quadrant at a time.

5.2.2 First Quadrant

The partial derivatives in the stiffness matrix requires the product rule since $\hat{u}$ and T are both variables of $\vec{\delta}$. The partial derivative in the first quadrant becomes:

$$-\frac{\partial(\hat{u}\,T)}{\partial\vec{\delta}_d} = -T\frac{\partial(\hat{u})}{\partial\vec{\delta}_d} - \hat{u}\frac{\partial(T)}{\partial\vec{\delta}_d} \tag{5.9}$$

Figure 5-2 shows what happens to the direction vector $\hat{u}$ and cable length L for a single cable when the end-effector is moved by a small displacement $\vec{\delta}_d$. $\hat{u}$ and $\hat{u}^*$ are the original and final directions of the cable. L and L^* are the original and final lengths of the cable.

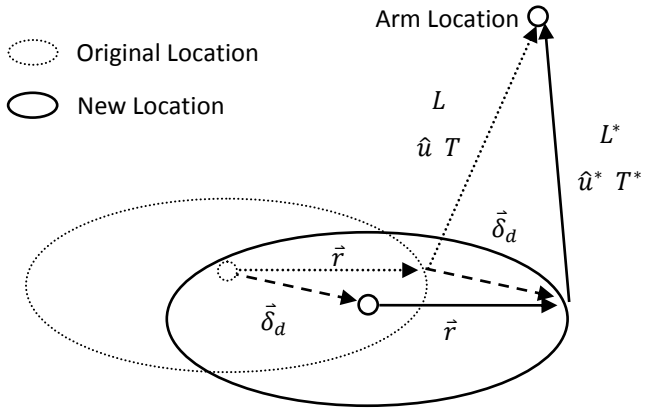

Figure 5-2: Changes in Cable Direction and Length under Small Displacement $\vec{\delta}_d$

Consider the first term in Equation (5.9), the partial derivative for the unit vector can be written with the limit definition of derivative as following:

$$\frac{\partial(\hat{u})}{\partial\vec{\delta}_d} = \lim_{\delta_d\to 0}\frac{\hat{u}^* - \hat{u}}{\vec{\delta}_d} \tag{5.10}$$

Let $\vec{u}$ and $\vec{u}^*$ be vector forms of the original and final lengths of the cable, where their magnitudes are L and L^*. The relationship between ($\hat{u}$, $\vec{u}$, L) and ($\hat{u}^*$, $\vec{u}^*$, L^*) is:

$$\hat{u} = \frac{\vec{u}}{L} \tag{5.11}$$

$$\hat{u}^* = \frac{\vec{u}^*}{L^*} \tag{5.12}$$

$$\vec{u}^* = \vec{u} - \vec{\delta}_d \tag{5.13}$$

Substituting these Equations (5.11) through (5.13) into Equation (5.10) gives:

$$\frac{\partial(\hat{u})}{\partial\vec{\delta}_d} = \lim_{\delta_d \to 0} \frac{\hat{u}^* - \hat{u}}{\vec{\delta}_d} = \lim_{\delta_d \to 0} \frac{\frac{\vec{u}^*}{L^*} - \frac{\vec{u}}{L}}{\vec{\delta}_d} = \lim_{\delta_d \to 0} \frac{\vec{u}^* L - \vec{u}\, L^*}{\vec{\delta}_d\, L\, L^*} \tag{5.14}$$

The scalar lengths L and L^* can be expressed in terms of components of $\vec{u}$ and $\vec{u}^*$:

$$L = \sqrt{{u_x}^2 + {u_y}^2 + {u_z}^2} \tag{5.15}$$

$$\begin{aligned} L^* &= \sqrt{{u^*}_x{}^2 + {u^*}_y{}^2 + {u^*}_z{}^2} \\ &= \sqrt{(u_x - \delta_x)^2 + \left(u_y - \delta_y\right)^2 + (u_z - \delta_z)^2} \\ &= \sqrt{{u_x}^2 + {u_y}^2 + {u_z}^2 - 2u_x\delta_x - 2u_y\delta_y - 2u_z\delta_z + {\delta_x}^2 + {\delta_y}^2 + {\delta_z}^2} \\ &= \sqrt{L^2 - 2u_x\delta_x - 2u_y\delta_y - 2u_z\delta_z + {\delta_x}^2 + {\delta_y}^2 + {\delta_z}^2} \\ &= L\sqrt{1 - \frac{2[u\delta]_{xyz}}{L^2} + \frac{[\delta^2]_{xyz}}{L^2}} \end{aligned} \tag{5.16}$$

where $[u\delta]_{xyz}$ represents $u_x\delta_x + u_y\delta_y + u_z\delta_z$, and $[\delta^2]_{xyz}$ represents ${\delta_x}^2 + {\delta_y}^2 + {\delta_z}^2$.

Substituting Equations (5.15) and (5.16) into Equation (5.14) gives:

$$\lim_{\delta_d \to 0} \frac{\vec{u}^* L - \vec{u}\, L^*}{\vec{\delta}_d\, L\, L^*} = \lim_{\delta_d \to 0} \frac{\left(\vec{u} - \vec{\delta}_d\right) - \vec{u}\sqrt{1 - \frac{2[u\delta]_{xyz}}{L^2} + \frac{[\delta^2]_{xyz}}{L^2}}}{\vec{\delta}_d\, L\sqrt{1 - \frac{2[u\delta]_{xyz}}{L^2} + \frac{[\delta^2]_{xyz}}{L^2}}} \tag{5.17}$$

Now, consider the partial derivative of Equation (5.17) limited to $\hat{u}_x$ with respect to δ_x:

$$\frac{\partial(\hat{u}_x)}{\partial\delta_x} = \lim_{\substack{\delta_x\to 0\\ \delta_y=0\\ \delta_z=0}} \frac{u^*{}_x - u_x\sqrt{1-\frac{2[u\delta]_{xyz}}{L^2}+\frac{[\delta^2]_{xyz}}{L^2}}}{\delta_d\, L\sqrt{1-\frac{2[u\delta]_{xyz}}{L^2}+\frac{[\delta^2]_{xyz}}{L^2}}} = \lim_{\substack{\delta_x\to 0\\ \delta_y=0\\ \delta_z=0}} \frac{(u_x-\delta_x) - u_x\sqrt{1-\frac{2\,u_x\delta_x}{L^2}+\frac{\delta_x{}^2}{L^2}}}{\delta_x\, L\sqrt{1-\frac{2\,u_x\delta_x}{L^2}+\frac{\delta_x{}^2}{L^2}}} = \frac{0}{0} \tag{5.18}$$

This yields an undefined solution to the limit, therefore the L'Hôpital's rule is necessary. Derivatives of the numerator and denominator with respect to δ_x gives:

$$\frac{\partial(\hat{u}_x)}{\partial\delta_x} = \lim_{\substack{\delta_x\to 0\\ \delta_y=0\\ \delta_z=0}} \frac{-1-u_x\,\frac{1}{2}\,\frac{\frac{-2\,u_x+2\,\delta_x}{L^2}}{\sqrt{1-\frac{2\,u_x\delta_x}{L^2}+\frac{\delta_x{}^2}{L^2}}}}{L\sqrt{1-\frac{2\,u_x\delta_x}{L^2}+\frac{\delta_x{}^2}{L^2}} \;+\; \delta_x[omitted]} \tag{5.19}$$

The second part of the denominator is omitted, because it is multiplied by δ_x and becomes zero. Evaluating the limit and simplifying gives the following final solution:

$$\frac{\partial(\hat{u}_x)}{\partial\delta_x} = \frac{-1-u_x\,\frac{1}{2}\,\frac{(-2\,u_x)}{L^2}}{L} = \frac{-1+\frac{u_x{}^2}{L^2}}{L} = \frac{-(L^2-u_x{}^2)}{L^3} \tag{5.20}$$

By the same pattern, partial derivatives of $\hat{u}_y$ with respect to δ_y and $\hat{u}_z$ with respect to δ_z are:

$$\frac{\partial(\hat{u}_y)}{\partial\delta_y} = \frac{-(L^2-u_y{}^2)}{L^3} \tag{5.21}$$

$$\frac{\partial(\hat{u}_z)}{\partial\delta_z} = \frac{-(L^2-u_z{}^2)}{L^3} \tag{5.22}$$

Now, consider partial derivative of Equation (5.17) for $\hat{u}_y$ with respect to δ_x:

$$\frac{\partial(\hat{u}_y)}{\partial\delta_x} = \lim_{\substack{\delta_x\to 0\\ \delta_y=0\\ \delta_z=0}} \frac{u^*{}_y - u_y\sqrt{1-\frac{2[u\delta]_{xyz}}{L^2}+\frac{[\delta^2]_{xyz}}{L^2}}}{\delta_d\, L\sqrt{1-\frac{2[u\delta]_{xyz}}{L^2}+\frac{[\delta^2]_{xyz}}{L^2}}} = \lim_{\substack{\delta_x\to 0\\ \delta_y=0\\ \delta_z=0}} \frac{(u_y-\delta_y) - u_y\sqrt{1-\frac{2\,u_x\delta_x}{L^2}+\frac{{\delta_x}^2}{L^2}}}{\delta_x\, L\sqrt{1-\frac{2\,u_x\delta_x}{L^2}+\frac{{\delta_x}^2}{L^2}}} = \frac{0}{0} \tag{5.23}$$

This limit also yields an undefined solution. Using the L'Hôpital's rule again gives:

$$\frac{\partial(\hat{u}_y)}{\partial\delta_x} = \lim_{\substack{\delta_x\to 0\\ \delta_y=0\\ \delta_z=0}} \frac{-u_y\,\frac{1}{2}\,\frac{\frac{-2\,u_x+2\,\delta_x}{L^2}}{\sqrt{1-\frac{2\,u_x\delta_x}{L^2}+\frac{{\delta_x}^2}{L^2}}}}{L\sqrt{1-\frac{2\,u_x\delta_x}{L^2}+\frac{{\delta_x}^2}{L^2}} \;+\; \delta_x[omitted]} \tag{5.24}$$

Evaluating the limit and simplifying gives:

$$\frac{\partial(\hat{u}_y)}{\partial\delta_x} = \frac{-u_y\frac{1}{2}\frac{(-2\,u_x)}{L^2}}{L} = \frac{u_x\,u_y}{L^3} \tag{5.25}$$

By the same pattern, other terms in the partial derivative are:

$$\frac{\partial(\hat{u}_z)}{\partial\delta_x} = \frac{u_x\,u_z}{L^3} \tag{5.26}$$

$$\frac{\partial(\hat{u}_x)}{\partial\delta_y} = \frac{u_x\,u_y}{L^3} \tag{5.27}$$

$$\frac{\partial(\hat{u}_z)}{\partial\delta_y} = \frac{u_y\,u_z}{L^3} \tag{5.28}$$

$$\frac{\partial(\hat{u}_x)}{\partial\delta_z} = \frac{u_x\,u_z}{L^3} \tag{5.29}$$

$$\frac{\partial(\hat{u}_y)}{\partial\delta_z} = \frac{u_y\,u_z}{L^3} \tag{5.30}$$

Finally, the first term in Equation (5.9) becomes the following:

$$-T\frac{\partial(\hat{u})}{\partial\vec{\delta}_d}=\frac{T}{L^3}\begin{bmatrix}L^2-{u_x}^2 & -u_x u_y & -u_x u_z\\ -u_x u_y & L^2-{u_y}^2 & -u_y u_z\\ -u_x u_z & -u_y u_z & L^2-{u_z}^2\end{bmatrix}=\frac{T}{L}\left[[I_{ide}]-\hat{u}\,\hat{u}^T\right] \tag{5.31}$$

where $[I_{ide}]$ is an 3 x 3 identity matrix.

Now, consider the second term in Equation (5.9). The partial derivative for the tension can be written in the limit definition of derivative as:

$$\frac{\partial(T)}{\partial\vec{\delta}_d}=\lim_{\delta_d\to 0}\frac{T^*-T}{\vec{\delta}_d} \tag{5.32}$$

Recall that the cables are modeled as linear springs with the equation for tension given in Equation (5.4). Rearranging this Equation gives:

$$T^*=T+k\,(L^*-L)$$

$$T^*-T=k\,(L^*-L) \tag{5.33}$$

Substituting Equation (5.33) and the expression for L^* from Equation (5.16) into Equation (5.32) gives:

$$\frac{\partial(T)}{\partial\vec{\delta}_d}=\lim_{\delta_d\to 0}\frac{T^*-T}{\vec{\delta}_d}=\lim_{\delta_d\to 0}\frac{k\,(L^*-L)}{\vec{\delta}_d}=\lim_{\delta_d\to 0}k\frac{L\sqrt{1-\frac{2[u\delta]_{xyz}}{L^2}+\frac{[\delta^2]_{xyz}}{L^2}}-L}{\vec{\delta}_d} \tag{5.34}$$

The partial derivative of Equation (5.35) for T with respect to δ_x gives:

$$\frac{\partial(T)}{\partial\delta_x}=\lim_{\substack{\delta_x\to 0\\ \delta_y=0\\ \delta_z=0}}k\,\frac{L\sqrt{1-\frac{2[u\delta]_{xyz}}{L^2}+\frac{[\delta^2]_{xyz}}{L^2}}-L}{\delta_x}=\lim_{\substack{\delta_x\to 0\\ \delta_y=0\\ \delta_z=0}}k\,\frac{L\sqrt{1-\frac{2\,u_x\delta_x}{L^2}+\frac{{\delta_x}^2}{L^2}}-L}{\delta_x}=\frac{0}{0} \tag{5.35}$$

Using the L'Hôpital's rule, derivatives of the numerator and denominator with respect to δ_x gives:

$$\frac{\partial(T)}{\partial \delta_x} = \lim_{\substack{\delta_x \to 0 \\ \delta_y = 0 \\ \delta_z = 0}} k\, L\, \frac{1}{2}\, \frac{\frac{-2\, u_x + 2\, \delta_x}{L^2}}{\sqrt{1 - \frac{2\, u_x \delta_x}{L^2} + \frac{{\delta_x}^2}{L^2}}} \tag{5.36}$$

Evaluating the limit and simplifying gives:

$$\frac{\partial(T)}{\partial \delta_x} = \; k\, L\, \frac{1}{2}\, \frac{\frac{(-2\, u_x)}{L^2}}{1} = -\, k\, \frac{u_x}{L} = -\, k\, \hat{u}_x \tag{5.37}$$

By the same pattern, partial derivatives for T with respect to δ_y and T with respect to δ_z are:

$$\frac{\partial(T)}{\partial \delta_y} = \; -\, k\, \hat{u}_y \tag{5.38}$$

$$\frac{\partial(T)}{\partial \delta_z} = \; -\, k\, \hat{u}_z \tag{5.39}$$

Then, the second term in Equation (5.9) becomes the following:

$$-\hat{u}\, \frac{\partial(T)}{\partial \vec{\delta}_d} = \hat{u}\, k\, [\hat{u}_x \quad \hat{u}_y \quad \hat{u}_z] = k\, [\hat{u}\, \hat{u}^T] \tag{5.40}$$

The final solution for the first quadrant of the stiffness matrix becomes:

$$-\frac{\partial(\hat{u}\, T)}{\partial \vec{\delta}_d} = \frac{T}{L}\left[[I_{ide}] - \hat{u}\, \hat{u}^T\right] + k\, [\hat{u}\, \hat{u}^T] \tag{5.41}$$

5.2.3 Second Quadrant

Using the product rule, the partial derivative in the second quadrant becomes:

$$-\frac{\partial(\hat{u}\,T)}{\partial\vec{\delta}_r} = -\,T\frac{\partial(\hat{u})}{\partial\vec{\delta}_r} - \hat{u}\frac{\partial(T)}{\partial\vec{\delta}_r} \tag{5.42}$$

When the end-effector rotates by a small rotation $\vec{\delta}_r$, the distance vector $\vec{r}$ from the center of the end-effector to the cable connection also rotates by $\vec{\delta}_r$. This causes the location of the cable connection to be moved by a small distance $\vec{p}$ as shown in Figure 5-3, and it has the same effect as $\vec{\delta}_d$ on the direction unit vector $\hat{u}$ and cable length L.

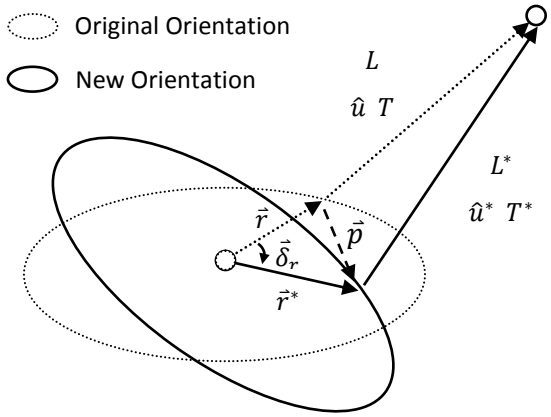

Figure 5-3: Changes in Cable Direction and Length under Small Rotation $\vec{\delta}_r$

Applying the chain rule with the new displacement variable p, Equation (5.42) can be written as:

$$-\frac{\partial(\hat{u}\,T)}{\partial\vec{\delta}_r} = -\,T\frac{\partial(\hat{u})}{\partial\vec{p}}\frac{\partial(\vec{p})}{\partial\vec{\delta}_r} - \hat{u}\frac{\partial(T)}{\partial\vec{p}}\frac{\partial(\vec{p})}{\partial\vec{\delta}_r} \tag{5.43}$$

Since $\vec{p}$ is virtually equivalent to $\vec{\delta}_d$, the following is true from the solution to the first quadrant:

$$-\,T\frac{\partial(\hat{u})}{\partial\vec{p}} = -\,T\frac{\partial(\hat{u})}{\partial\vec{\delta}_d} = \frac{T}{L}\left[[I_{ide}] - \hat{u}\,\hat{u}^T\right] \tag{5.44}$$

$$-\,\hat{u}\frac{\partial(T)}{\partial\vec{p}} = -\,\hat{u}\frac{\partial(T)}{\partial\vec{\delta}_d} = k\,[\hat{u}\,\hat{u}^T] \tag{5.45}$$

Then, the only new unknown in Equation (5.43) is the partial derivative of $\vec{p}$ with respect to $\vec{\delta}_r$. The following equations show *x*, *y*, and *z* components of $\partial\vec{p}$ in terms of $\partial\vec{\delta}_r = (\ \partial\theta_x \quad \partial\theta_y \quad \partial\theta_z\ )$:

$$\partial p_x = r_z\,\partial\theta_y - r_y\,\partial\theta_z \tag{5.46}$$

$$\partial p_y = -r_z\,\partial\theta_x + r_x\,\partial\theta_z \tag{5.47}$$

$$\partial p_z = r_y\,\partial\theta_x - r_x\,\partial\theta_y \tag{5.48}$$

Based on Equations (5.46) to (5.48), it is not difficult to derive every term for this partial derivative:

$$\frac{\partial(\vec{p})}{\partial\vec{\delta}_r} = \begin{bmatrix} \frac{\partial(p_x)}{\partial\theta_x} & \frac{\partial(p_x)}{\partial\theta_y} & \frac{\partial(p_x)}{\partial\theta_z} \\ \frac{\partial(p_y)}{\partial\theta_x} & \frac{\partial(p_y)}{\partial\theta_y} & \frac{\partial(p_y)}{\partial\theta_z} \\ \frac{\partial(p_z)}{\partial\theta_x} & \frac{\partial(p_z)}{\partial\theta_y} & \frac{\partial(p_z)}{\partial\theta_z} \end{bmatrix} = \begin{bmatrix} 0 & r_z & -r_y \\ -r_z & 0 & r_x \\ r_y & -r_x & 0 \end{bmatrix} = [\vec{r}\times]^T \tag{5.49}$$

The matrix $[\vec{r}\times]$ is the cross product operator, or the skew-symmetric matrix, of vector $\vec{r} = (\ r_x \quad r_y \quad r_z\ )^T$, which it has the form:

$$[\vec{r}\times] = \begin{bmatrix} 0 & -r_z & r_y \\ r_z & 0 & -r_x \\ -r_y & r_x & 0 \end{bmatrix} \tag{5.50}$$

and it has the property $[\vec{r}\times]^T = -[\vec{r}\times]$.

Substituting Equations (5.44), (5.45), and (5.49) into Equation (5.43) gives the final solution for the second quadrant of the stiffness matrix:

$$-\frac{\partial(\hat{u}\,T)}{\partial\vec{\delta}_r} = \frac{T}{L}[\ [\vec{r}\times]^T - \hat{u}\,\hat{u}^T[\vec{r}\times]^T\ ] + k\,[\ \hat{u}\,\hat{u}^T[\vec{r}\times]^T\ ] \tag{5.51}$$

5.2.4 Third Quadrant

Using the product rule, the partial derivative in the third quadrant becomes:

$$-\frac{\partial\left((\vec{r}\times\hat{u})\,T\right)}{\partial\vec{\delta}_d}=-T\frac{\partial(\vec{r}\times\hat{u})}{\partial\vec{\delta}_d}-(\vec{r}\times\hat{u})\frac{\partial(T)}{\partial\vec{\delta}_d} \tag{5.52}$$

The cross product between $\vec{r}$ and $\hat{u}$ can be represented by a matrix multiplication between $[\vec{r}\times]$ and $\hat{u}$:

$$\vec{r}\times\hat{u}=\begin{bmatrix} r_y\hat{u}_z-r_z\hat{u}_y \\ r_z\hat{u}_x-r_x\hat{u}_z \\ r_x\hat{u}_y-r_y\hat{u}_x \end{bmatrix}=[\vec{r}\times]\,\hat{u} \tag{5.53}$$

Since r is constant with respect to $\vec{\delta}_d$, $[\vec{r}\times]$ can be taken out from the partial derivative. The first part of Equation (5.52) becomes:

$$-T\frac{\partial(\vec{r}\times\hat{u})}{\partial\vec{\delta}_d}=-T\frac{\partial([\vec{r}\times]\hat{u})}{\partial\vec{\delta}_d}=-T[\vec{r}\times]\frac{\partial(\hat{u})}{\partial\vec{\delta}_d} \tag{5.54}$$

Substituting Equation (5.41) from the first quadrant into Equation (5.54) gives:

$$-T\frac{\partial(\vec{r}\times\hat{u})}{\partial\vec{\delta}_d}=-T[\vec{r}\times]\frac{\partial(\hat{u})}{\partial\vec{\delta}_d}=\frac{T}{L}[\vec{r}\times]\left[[I_{ide}]-\hat{u}\,\hat{u}^T\right]=\frac{T}{L}\left[[\vec{r}\times]-[\vec{r}\times]\hat{u}\,\hat{u}^T\right] \tag{5.55}$$

Similarly, substituting Equation (5.41) into the second part of Equation (5.52) gives:

$$-(\vec{r}\times\hat{u})\frac{\partial(T)}{\partial\vec{\delta}_d}=-[\vec{r}\times]\,\hat{u}\frac{\partial(T)}{\partial\vec{\delta}_d}=[\vec{r}\times]\,\hat{u}\,k\,\hat{u}^T=k\left[[\vec{r}\times]\hat{u}\,\hat{u}^T\right] \tag{5.56}$$

Then, the final solution for the third quadrant of the stiffness matrix becomes the following:

$$-\frac{\partial\left((\vec{r}\times\hat{u})\,T\right)}{\partial\vec{\delta}_d}=\frac{T}{L}\left[[\vec{r}\times]-[\vec{r}\times]\hat{u}\,\hat{u}^T\right]+\,k\left[[\vec{r}\times]\hat{u}\,\hat{u}^T\right] \tag{5.57}$$

5.2.5 Fourth Quadrant

In this quadrant, the displacement vector $\vec{r}$ changes with respect to change in $\vec{\delta}_r$. Therefore, $\vec{r} \times \hat{u}$ requires the product rule. The partial derivative in the fourth quadrant becomes:

$$-\frac{\partial\big((\vec{r} \times \hat{u})\, T\big)}{\partial \vec{\delta}_r} = -\frac{\partial([\vec{r} \times]\hat{u}\, T)}{\partial \vec{\delta}_r} = -T\,\frac{\partial([\vec{r} \times])}{\partial \vec{\delta}_r}\hat{u} - T[\vec{r} \times]\frac{\partial(\hat{u})}{\partial \vec{\delta}_r} - (\vec{r} \times \hat{u})\frac{\partial(T)}{\partial \vec{\delta}_r} \tag{5.58}$$

Solutions for the second term and third term are already available from combinations of previous results from the second quadrant and third quadrant:

$$-T[\vec{r} \times]\frac{\partial(\hat{u})}{\partial \vec{\delta}_r} = \frac{T}{L}\big[[\vec{r} \times][I_{ide} - \hat{u}\,\hat{u}^T]\big][\vec{r} \times]^T = \frac{T}{L}\big[[\vec{r} \times][\vec{r} \times]^T - [\vec{r} \times]\hat{u}\,\hat{u}^T[\vec{r} \times]^T\big] \tag{5.59}$$

$$-(\vec{r} \times \hat{u})\frac{\partial(T)}{\partial \vec{\delta}_r} = k\,[\vec{r} \times][\hat{u}\,\hat{u}^T][\vec{r} \times]^T = k\,\big[[\vec{r} \times]\hat{u}\,\hat{u}^T[\vec{r} \times]^T\big] \tag{5.60}$$

The first term involves the partial derivative of $[\vec{r} \times]$ with respect to $\vec{\delta}_r$, which can be rearranged as:

$$-T\,\frac{\partial([\vec{r} \times])}{\partial \vec{\delta}_r}\hat{u} = -T\,\frac{\partial(\vec{r} \times \hat{u})}{\partial \vec{\delta}_r} = -T\,\frac{-\partial(\hat{u} \times \vec{r})}{\partial \vec{\delta}_r} = T\,[\hat{u} \times]\frac{\partial(\vec{r})}{\partial \vec{\delta}_r} \tag{5.61}$$

It can be observed from Figure 5-3 that $\vec{r}^* - \vec{r} = \vec{p}$. The derivative of $\vec{r}$ with respect to $\vec{\delta}_r$ is equal to the derivative of $\vec{p}$ with respect to $\vec{\delta}_r$, which evaluates to $[\vec{r} \times]^T$ from Equation (5.49).

$$-T\,\frac{\partial([\vec{r} \times])}{\partial \vec{\delta}_r}\hat{u} = T\,[\hat{u} \times]\frac{\partial(\vec{r})}{\partial \vec{\delta}_r} = T\,[\hat{u} \times]\frac{\partial(\vec{p})}{\partial \vec{\delta}_r} = T\,[\hat{u} \times][\vec{r} \times]^T \tag{5.62}$$

Then using the property $[\vec{r} \times]^T = -[\vec{r} \times]$ gives:

$$-T\,\frac{\partial([\vec{r} \times])}{\partial \vec{\delta}_r}\hat{u} = T\,[\hat{u} \times][\vec{r} \times]^T = -T\,[\hat{u} \times][\vec{r} \times] \tag{5.63}$$

Then the final solution for the fourth quadrant of the stiffness matrix is as following:

$$-\frac{\partial\big((\vec{r} \times \hat{u})\, T\big)}{\partial \vec{\delta}_r} = \frac{T}{L}\big[[\vec{r} \times][\vec{r} \times]^T - [\vec{r} \times]\hat{u}\,\hat{u}^T[\vec{r} \times]^T\big] + k\,\big[[\vec{r} \times]\hat{u}\,\hat{u}^T[\vec{r} \times]^T\big] - T\,[\hat{u} \times][\vec{r} \times] \tag{5.64}$$

5.2.6 Complete Stiffness Matrix and Stability

Solutions for the partial derivatives for each quadrant was determined in Sections 5.2.2 to 5.2.5. Combining these solutions together gives the stiffness matrix for a single cable. Adding the summation back gives a complete stiffness matrix for the end-effector. The following equation shows this complete stiffness matrix for the end-effector, $[K]$, separated into three parts:

$$
\begin{aligned}
[K] \quad = \quad & \sum_{i=1}^{7} \quad k_i \begin{bmatrix} \hat{u}_i\,\hat{u}_i^{\,T} & \hat{u}_i\;\hat{u}_i^{\,T}[\vec{r}_i\times]^T \\ [\vec{r}_i\times]\,\hat{u}_i\,\hat{u}_i^{\,T} & [\vec{r}_i\times]\,\hat{u}_i\;\hat{u}_i^{\,T}[\vec{r}_i\times]^T \end{bmatrix} \\
+ \quad & \sum_{i=1}^{7} \quad \frac{T_i}{L_i} \begin{bmatrix} [I_{ide}] - \hat{u}_i\,\hat{u}_i^{\,T} & [\vec{r}_i\times]^T - \hat{u}_i\;\hat{u}_i^{\,T}[\vec{r}_i\times]^T \\ [\vec{r}_i\times] - [\vec{r}_i\times]\,\hat{u}_i\,\hat{u}_i^{\,T} & [\vec{r}_i\times][\vec{r}_i\times]^T - [\vec{r}_i\times]\,\hat{u}_i\;\hat{u}_i^{\,T}[\vec{r}_i\times]^T \end{bmatrix} \\
+ \quad & \sum_{i=1}^{7} \quad T_i \begin{bmatrix} 0 & 0 \\ 0 & -[\hat{u}_i\times][\vec{r}_i\times] \end{bmatrix}
\end{aligned} \tag{5.65}
$$

Let K_1, K_2, and K_3 represents each part of the complete stiffness matrix:

$$[K] = K_1 + K_2 + K_3 \tag{5.66}$$

$$K_1 \quad = \quad \sum_{i=1}^{7} \quad k_i \begin{bmatrix} \hat{u}_i\,\hat{u}_i^{\,T} & \hat{u}_i\;\hat{u}_i^{\,T}[\vec{r}_i\times]^T \\ [\vec{r}_i\times]\,\hat{u}_i\,\hat{u}_i^{\,T} & [\vec{r}_i\times]\,\hat{u}_i\;\hat{u}_i^{\,T}[\vec{r}_i\times]^T \end{bmatrix} \tag{5.67}$$

$$K_2 \quad = \quad \sum_{i=1}^{7} \quad \frac{T_i}{L_i} \begin{bmatrix} [I_{ide}] - \hat{u}_i\,\hat{u}_i^{\,T} & [\vec{r}_i\times]^T - \hat{u}_i\;\hat{u}_i^{\,T}[\vec{r}_i\times]^T \\ [\vec{r}_i\times] - [\vec{r}_i\times]\,\hat{u}_i\,\hat{u}_i^{\,T} & [\vec{r}_i\times][\vec{r}_i\times]^T - [\vec{r}_i\times]\,\hat{u}_i\;\hat{u}_i^{\,T}[\vec{r}_i\times]^T \end{bmatrix} \tag{5.68}$$

$$K_3 \quad = \quad \sum_{i=1}^{7} \quad T_i \begin{bmatrix} 0 & 0 \\ 0 & -[\hat{u}_i\times][\vec{r}_i\times] \end{bmatrix} \tag{5.69}$$

K_1 comes from changes in cable tensions due to movement of the end-effector. K_2 and K_3 come from changes in direction of cable tensions. K_1 contributes for the majority of the total stiffness while K_2 and K_3 are relatively small. This is because k_i is usually a very large number over $1 \times 10^4 N/m$ for steel cable, compared to T_i which typically ranges between 20 to 200 N.

The complete stiffness matrix obtained in this section is equivalent to the stiffness matrix derived by Behzadipour in his thesis [2]. $K_1 + K_2$ is equivalent to K_s from Equation (6.27) from his thesis, and K_3 is equivalent to K_f from Equation (6.31) from his thesis. How to include the spine force in the stiffness calculation was not discussed in [2], but the derivation in this thesis shows that the spine force should be treated as one of the cable tension with zero for both the displacement vector ($\vec{r}$) and cable stiffness (k).

Behzadipour introduces the concept of "*stability*" and "*stabilizability*" in his thesis. His definition of stabilizability is:

Definition: ***Stabilizability*** *A cable-based manipulator is stabilizable if and only if its total stiffness matrix can be made positive definite under any arbitrary external load by choosing a proper set of antagonistic forces.*

In this case, the antagonistic force refers to the spine force. Another way to interpret stabilizability is that external forces and moments necessary to move the end-effector must increase as the end-effector moves further away from the original position. Stability of the end-effector can be verified from its stiffness matrix. The end-effector is stable if and only if the stiffness matrix is positive definite.

5.3 Valid Range for Stiffness Calculation

A stiffness of a linear spring is valid for any spring length as long as there is no plastic deformation. However, this is not the case for stiffness matrices of cable-based manipulators. The complete stiffness matrix for the end-effector shown in Equation (5.65) depends on a set of cable tensions. Magnitudes and directions of these cable tensions change depending on the position of the end-effector in the workspace. Therefore, a stiffness matrix calculated at a particular end-effector position is not valid elsewhere. In order to understand stiffness of the end-effector along the entire workspace, it is required to calculate the stiffness matrix at every single position. This is fine for stiffness in the x and y directions, but it is a problem for stiffness in the z direction, which causes the end-effector to move in the out-of-plane direction. Equations for calculating cable tensions formulated in Section 4.3.4 do not consider out-of-plane motions, and tensionability of the manipulator is not guaranteed in the out-of-plane direction. This means that even if the calculated stiffness is high, it may only be valid for a short range of motion due to changes in cable tensions. Stiffness of the end-effector is significantly reduced if one of the cables loses tension.

In the new proposed manipulator design, the most important part of the stiffness matrix is translational stiffness in the z (out-of-plane) direction. Reformulating new equations for inverse kinematics and cable tensions to include out-of-plane component would require these equations to be much more complicated. Instead, a simpler method is proposed to estimate the force required to make at least one of the cables lose tension. This method applies an external force in the out-of-plane direction while keeping the end-effector fixed, and then calculates new cable tensions. The external force is increased until one of the cables loses tension. In reality, the end-effector would move when an external force is applied. However, it is difficult to calculate the exact movement of the end-effector because the stiffness matrix changes at each step. Therefore, valid range of stiffness calculated with this method should only be used as an estimate, or to compare stiffness of different designs.

Method for Estimating Valid Range of Stiffness

1. Select a position (*x*, *y*) to examine the out-of-plane stiffness. Calculate the cable tensions and stiffness matrix $[K]$ at this position using Equations (4.32) and (5.65).

2. Let W be a vector of applied forces and moments on the end-effector:

$$\overrightarrow{W} = (\ F_x \quad F_y \quad F_z \quad M_x \quad M_y \quad M_z\ )^T$$

3. Initialize all terms in $\overrightarrow{W}$ to be 0.

4. Select a term from $\overrightarrow{W}$ and increase it by a small step, for translational stiffness in the out-of-plane direction, F_z is the most appropriate choice.

5. Recalculate new cable tensions with Equation (4.32), but include $\overrightarrow{W}$ and ignore the dynamic terms:

$$\vec{T} = [A]^{-1}\left(\vec{B} + \overrightarrow{W}\right) \tag{5.70}$$

6. Go to step 7 if at least one of the cable tensions is lesser than or equal to 0. Otherwise go back to step 4 and further increase the selected term by a small step to repeat the process.

7. Use the vector $\overrightarrow{W}$ that satisfies condition stated in step 6 and inverse of the stiffness matrix $[K]$ to estimate displacement of the end-effector under the applied forces and moments $\overrightarrow{W}$:

$$displacement = [K]^{-1}\,\overrightarrow{W} \tag{5.71}$$

5.4 Comparison of Stiffness Between Different Cable Configurations

In Section 5.2.6, it is stated that K_1 contributes for the majority of the total stiffness because the coefficient k is typically large. This coefficient k is the elongation stiffness of the steel cable itself, and it only acts along the axial direction of the cable, or in other words along the cable direction unit vector $\hat{u}$. Stiffness in the lateral direction normal to the unit vector $\hat{u}$ is not very strong. Therefore, in order for the end-effector to have good stiffness in all 6 DOF, the cable configuration becomes important. In general, it is a good design decision to have more component of $\hat{u}$ in the direction that requires more stiffness. In the case of the new proposed manipulator, the translational stiffness in the out-of-plane direction is most important. Therefore, the cables should have as much component in the z direction as possible without making the out-of-plane profile of the robot too large.

In addition to the consideration on K_1, tensionability, and stability, there is another factor that affects the cable orientation and configuration. Figure 5-4 shows the path of a cable fixed at one end. The cable is assumed to be under tension at all time, and it behaves like a rigid link. Let this path be called "*natural path*" of the cable. Figure 5-5 shows an end-effector with two cables in a parallelogram configuration. There is virtually no translational stiffness in the horizontal direction since the natural paths of the cables are equivalent. However, rotational stiffness is very high because rotating the end-effector would move them away from the natural paths. Figure 5-6 shows an end-effector with cables in a triangle configuration. The end-effector cannot translate at all without moving away from the natural paths, which gives the triangle configuration very high translational stiffness. However, it has virtually no rotational stiffness since the end-effector is free to rotate about the center. Figure 5-7 shows an end-effector with cables in a trapezoid configuration. The end-effector can translate and rotate to some degree while staying on the natural paths. Translation and rotation are coupled together in this case. This configuration provides both translational and rotational stiffness, but neither is as high as rotational stiffness in parallelogram or translational stiffness in triangle.

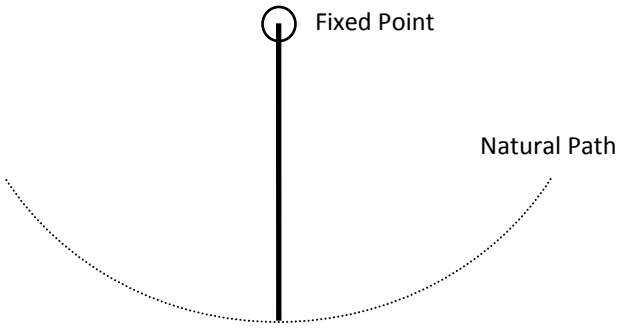

Figure 5-4: Natural Path for a Single Cable

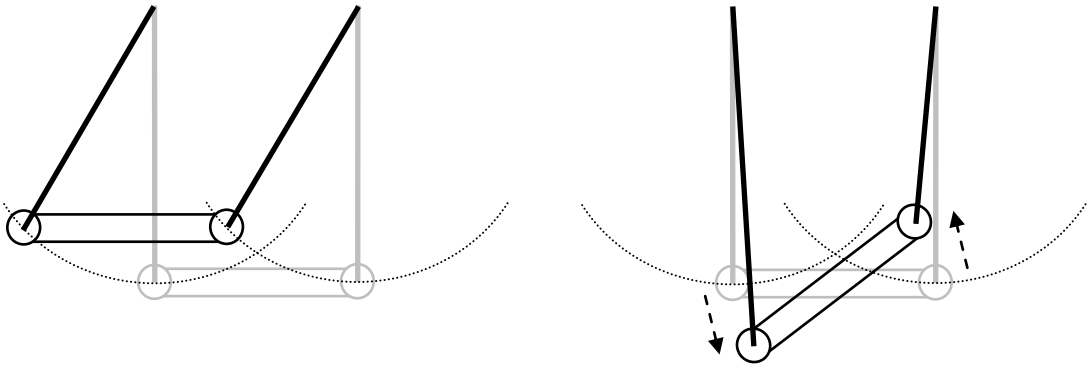

Figure 5-5: Natural Paths for Parallelogram Configuration

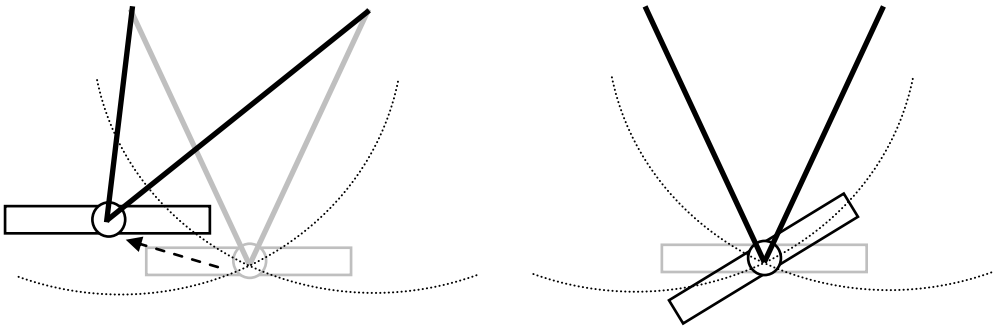

Figure 5-6: Natural Paths for Triangle Configuration

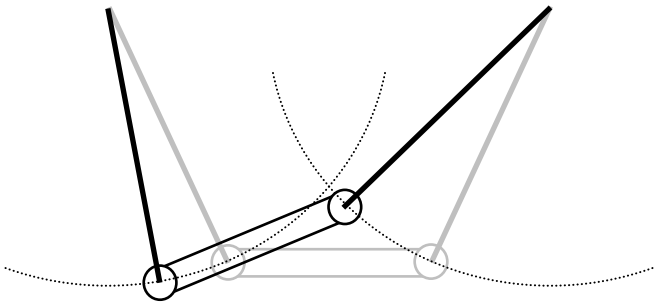

Figure 5-7: Natural Paths for Trapezoid Configuration

The parallelogram configuration provides high rotational stiffness but low translational stiffness. The triangle configuration provides high translational stiffness but low rotational stiffness. The cable configuration used in the new proposed design is based on the idea of combining parallelogram and triangle configurations to have both high translational stiffness and high rotational stiffness. Figure 5-8 (*a)* shows that cable pairs 3-4 and 5-6 creates a parallelogram configuration. Figure 5-8 (b) shows that cable pairs 3-4 and 5-6 can be reduced into a single cable, and then it creates a triangle configuration with cable pair 1-2. Therefore, the cable configuration in the front view is a combination of a parallelogram and a triangle. The parallelogram configuration provides high rotational stiffness about the *z* axis, while the triangle configuration provides high translational stiffness in the *x* direction. The cable configuration in the side view is also a combination of parallelogram and triangle as shown in Figure 3-10.

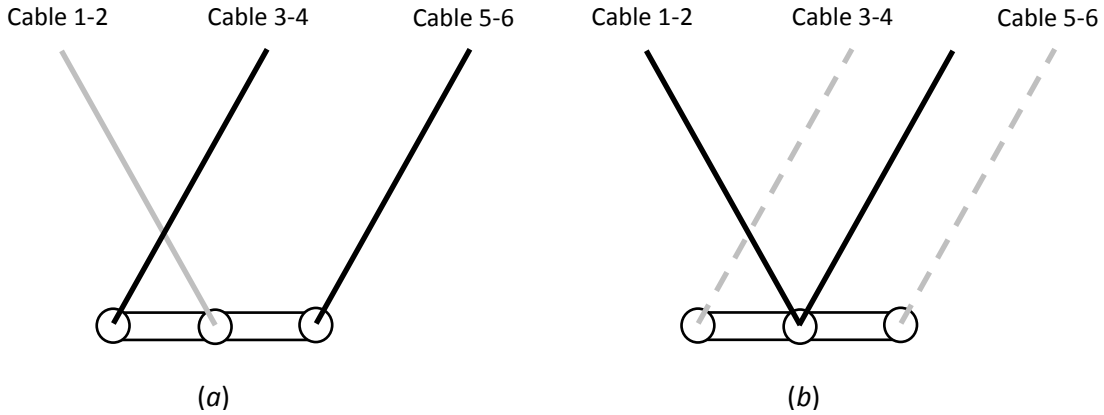

Figure 5-8: Cable Configuration for the New Proposed Design (Front View)

Figure 5-9 shows a sample stiffness matrix for the new proposed manipulator design. Translational stiffness in the *x* and *z* directions are highlighted bold in the stiffness matrix, and they are entries in cells (1,1) and (3,3) respectively. Translational stiffness in the *x* direction is much higher than translational stiffness in the *z* direction. This is because the cable direction unit vectors ($\hat{u}$) have more component in the *x* direction. It can be observed that the second and third quadrants of the stiffness matrix are zero matrices, which means that there is no coupling effect between translational stiffness and rotational stiffness. Table 5-1 shows the displacement of the end-effector caused by various magnitudes of applied forces in the *z* direction. The end-effector is estimated to move 2.8 *mm* under 40 *N* of applied force.

$$[K] = 10^6 \times \begin{bmatrix} \mathbf{0.4540} & -0.2372 & 0 & 0 & 0 & 0 \\ -0.2372 & 1.1559 & 0 & 0 & 0 & 0 \\ 0 & 0 & \mathbf{0.0143} & 0 & 0 & 0 \\ 0 & 0 & 0 & 0.0010 & -0.0006 & 0 \\ 0 & 0 & 0 & -0.0006 & 0.0006 & 0 \\ 0 & 0 & 0 & 0 & 0 & 0.0120 \end{bmatrix}$$

Figure 5-9: Sample Stiffness Matrix for the New Proposed Design

Table 5-1: Sample Displacement of the End-Effector

		Applied Force in *z* direction (*N*)			
		10	20	30	40
Displacement (m) or (rad)	δ_x	0	0	0	0
	δ_y	0	0	0	0
	δ_z	0.7002×10^{-3}	0.0014	0.0021	0.0028
	θ_x	0	0	0	0
	θ_y	0	0	0	0
	θ_z	0	0	0	0

Suppose that the cable configuration for the new proposed design is slightly modified as shown in Figure 5-10. The side view is now a combination of parallelogram and trapezoid configurations, while the front view is kept the same. No other changes are made to this modified design.

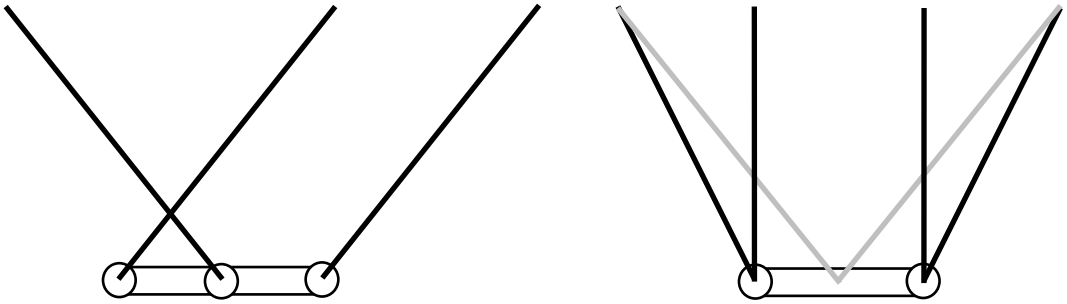

Figure 5-10: Cable Configuration for the Modified Design

Figure 5-11 shows the stiffness matrix for the modified design. It can be observed that translational stiffness in the *x* direction remains unchanged, but translational stiffness in the z direction decreased significantly. Table 5-2 shows displacements of the end-effector caused by various magnitudes of applied forces in the *z* direction. The table shows that displacements are much larger compared to the design before the modification, and there are coupled rotations about the *x* and *y* axis associated with displacement in the *z* direction. This is coupling effect is also shown in the stiffness matrix because the second and third quadrants are no longer zero matrices.

$$[K] = 10^6 \times \begin{bmatrix} \mathbf{0.4562} & -0.2407 & 0 & 0 & 0 & 0 \\ -0.2407 & 1.1615 & 0 & 0 & 0 & 0 \\ 0 & 0 & \mathbf{0.0064} & -0.0035 & -0.0022 & 0 \\ 0 & 0 & -0.0035 & 0.0027 & 0.0007 & 0 \\ 0 & 0 & -0.0022 & 0.0007 & 0.0012 & 0 \\ 0 & 0 & 0 & 0 & 0 & 0.0121 \end{bmatrix}$$

Figure 5-11: Sample Stiffness Matrix for the New Proposed Design (Modified)

Table 5-2: Sample Displacement of the End-Effector (Modified)

		Applied Force in z direction (N)			
		10	20	30	40
Displacement (m) or (rad)	δ_x	0	0	0	0
	δ_y	0	0	0	0
	δ_z	0.0351	0.0702	0.1052	0.1403
	θ_x	0.0332	0.0664	0.0996	0.1328
	θ_y	0.0454	0.0909	0.1363	0.1817
	θ_z	0	0	0	0

Two conclusions can be made from comparing cable configurations in the new proposed design versus the modified design. The combination of parallelogram configuration and triangle configuration is very effective in providing both high translational stiffness and high rotational stiffness. A slight modification in the cable configuration can significantly alter the overall stiffness due to changes in the natural paths of the cables.

5.5 Limitations in Stiffness Calculations and the Physical Model

This section discusses some assumptions in the stiffness calculation and limitations in manufacturing of the physical model.

- Cables are treated as linear springs in the stiffness calculation, which allows both elongation and compression. However, cables can only accept elongation, and the only time they do compress is when they lose tension. The stiffness calculation ignores the fact that some cables may have negative changes in length. Verifying tensionability and valid range for stiffness should address this problem to some degree.

- The cable configuration for the new proposed design requires some cable attachments to be right beside each other on the end-effector. This is not physically possible due to mechanical interference. The cables will be attached as close to each other as possible, but this will result in some loss of translational stiffness in the out-of-plane direction.

- Unequal cable lengths can distort the position and orientation of the end-effector, or cause one of the cables to lose tension faster than expected. This causes problems in both tensionability and loss of stiffness.

Chapter 6

Optimization of Design Parameters

6.1 Introduction to Optimization of Design Parameters

The purpose of optimization in the design of the new proposed manipulator is to determine the best set of design parameters that satisfies certain design specifications. Design specifications are requirements that must be met, such as size of the workspace and maximum payload. The design parameters to be optimized are kinematic dimensions of the manipulator, such as lengths of the arms and cables. Different sets of design parameters are compared according to their cost functions, which include dynamic performance, stiffness performance, and size of the manipulator.

6.1.1 Design Specifications

The workspace of the new proposed manipulator is a rectangle with horizontal length of 1.2 *m* and height of 0.3 *m*. The payload for the manipulator is set to be 1.0 *kg* including the end-effector itself. Most of the weight is assumed to be the end-effector, since the high-speed pick-and-place operation is done by a vacuum suction cup which cannot lift too much weight. The eccentricity in the *y* direction is set to 5 *cm* below the end-effector, while eccentricity in the *x* and *z* directions are ignored and set to zero . In order to determine the minimum required spine force, the absolute minimum cable tension is defined to be 15 *N*. This means that even under the worst case scenario, cable tensions will never drop below 15 *N*. The cycle time is aimed at 90 cycles per minute, which requires the end-effector to move at maximum acceleration

and velocity of 4 g and 6.0 m/s respectively. The requirements for maximum acceleration and velocity are reduced near the edge of the workspace as shown in Figure 6-1. The end-effector is not expected to move very fast near the edge of the workspace, and it is also where the minimum cable tension occurs. Reducing the maximum acceleration and velocity prevents over-designing the manipulator for extreme corner cases, and focuses on more common area of the workspace.

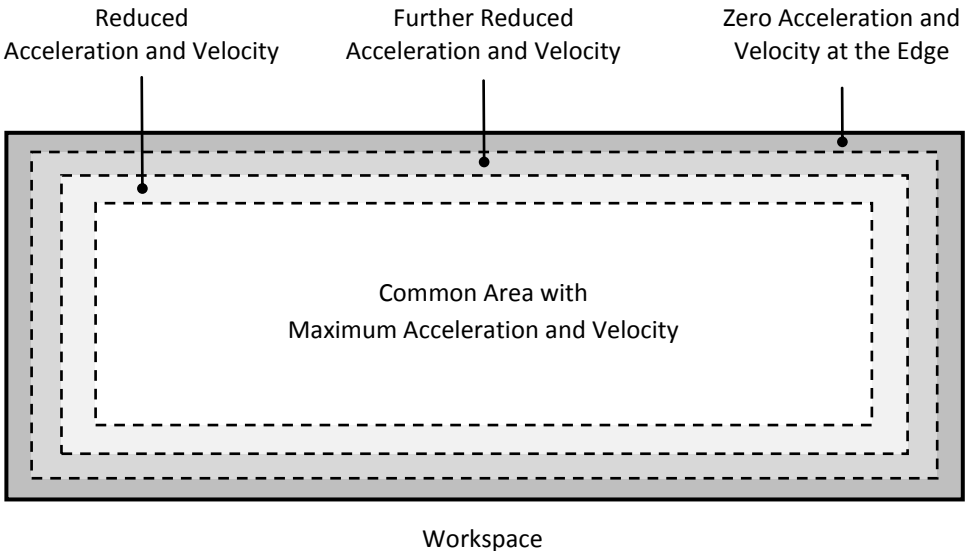

Figure 6-1: Reduction of Maximum Required Acceleration and Velocity

6.1.2 Design Parameters

The design parameters to be optimized are listed in Table 6-1. Most of them are kinematic dimensions already shown in Section 4.1 with their usage shown in Figure 4-1 and Figure 4-2. The only new parameter introduced here is H_{WS}, which represents "*starting height of the workspace*". Figure 6-2 shows an example of the required rectangular workspace that can fit in a total available workspace created by a parallel structure. The required workspace is much smaller than the total available workspace. H_{WS} is the vertical distance from the origin of the manipulator to the top of the required workspace. Note that the bottom of the required workspace should avoid contact with the edge of the total available workspace,

because the edge is near singularity for the arms and cables. Ranges for the design parameters are arbitrarily chosen to be reasonable values that are not too large or too small. The range for H_{WS} is calculated based on the size of available workspace determined from other design parameters.

Table 6-1: List of Design Parameters

Parameter	Range
L_B	$0.20\ m - 0.50\ m$
L_A	$0.20\ m - 0.50\ m$
L_C	$1.00\ m - 2.50\ m$
L_E	$0.10\ m - 0.30\ m$
L_{AS}	$0.10\ m - 0.30\ m$
L_{ES}	$0.05\ m - 0.20\ m$
H_{WS}	n/a

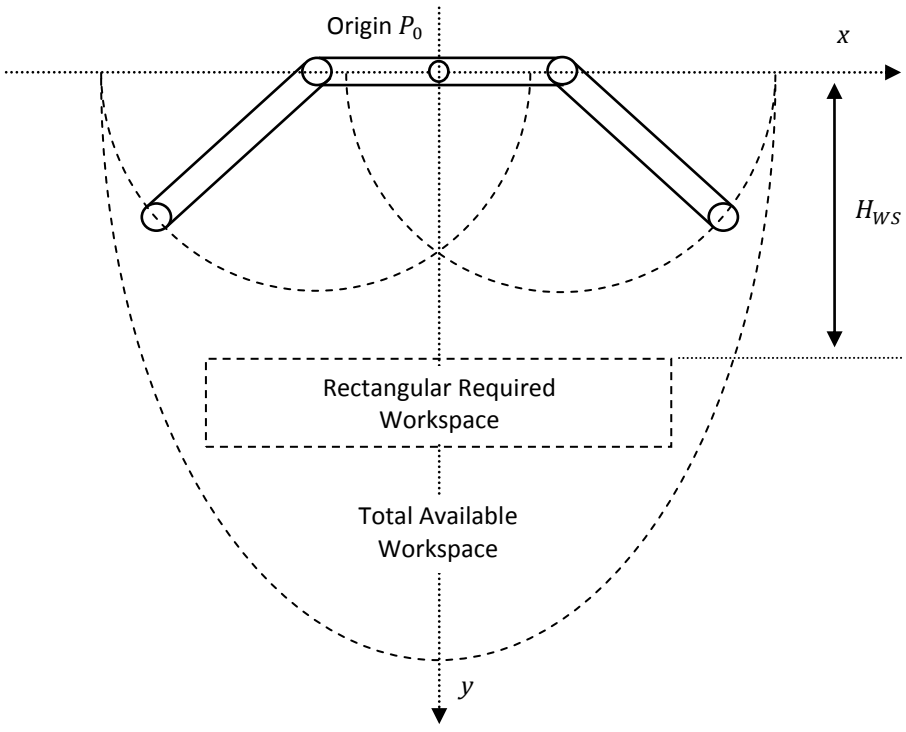

Figure 6-2: Required Workspace and Total Available Workspace

6.1.3 Cost Functions

Table 6-2 lists all the cost functions used in the optimization for the best set of design parameters. Minimum required spine force, is the amount of spine force required to satisfy the minimum required cable tension of 15 *N* under the worst case. Maximum cable tension is the highest cable tension value calculated based on the minimum required spine force. Maximum static torque, maximum dynamic torque, and maximum angular velocity are cost functions associated with the motor dynamic. Stiffness for different sets of design parameters are compared with the amount of out-of-plane displacement when a 40 *N* external force is applied to the end-effector. Size of the manipulator is compared by area of a rectangular box that can encase the entire manipulator.

Table 6-2: List of Cost Functions

Cost	Description	Limit	Weight
F_{C_min}	minimum required spine force	$500\ N$	0.5
T_{max}	maximum cable tension	$300\ N$	0.5
τ_{st_max}	maximum static torque	$150\ N \cdot m$	1.0
τ_{dy_max}	maximum dynamic torque	$300\ N \cdot m$	2.0
$\dot{\theta}_{max}$	maximum angular velocity	$194\ rpm$	2.0
δ_z	out-of-plane displacement under 40 N of force in the *z* direction	n/a	1.5
S_{area}	size of the manipulator in area	n/a	1.0

The "*limit*" column shows the maximum allowable value for each cost functions. For example, limit for maximum static torque and maximum dynamic torque are defined by the motor datasheet. If any one of the cost functions evaluates to a value higher than the limit, that particular set of design parameters are considered invalid, and the total cost is set to infinity.

These cost functions must be summed into a single total cost function in order to compare different sets of design parameters. This summation is not a trivial task for two reasons. First, not all cost functions

are weighted equally as shown in the "*weight*" column, since some cost functions are more important than others. Second, the cost functions have different units, and they cannot be summed without normalization of their values. The expression for the total cost function is as following:

$$Total\ Cost \quad = \quad \sum_{n=1}^{7} \ (Weight)_n \times \frac{(Cost)_n}{(Normalization\ Factor)_n} \tag{6.1}$$

The weight for each cost functions are assigned based on experience and prior knowledge in designs of cable-based manipulators. For example, increasing the spine force would directly increase cable tensions and motor torques, but in this case the motors are more likely to reach their dynamic limit before the cylinders or cables do. Therefore, cost functions for the motor dynamic are weighted higher than minimum required spine force and maximum cable tension. The same applies for maximum dynamic torque compared to maximum static torque. The motors are more likely to reach the dynamic torque limit before the static torque limit.

6.2 Evaluation of Cost Functions

In order to compare dynamic performances of different sets of design parameters, it is necessary to find the worse case value for each cost functions. In order to do this, the required workspace is divided into many data points as shown in Figure 6-3, and then all cost functions are evaluated at each data point. The interval between each point is decided to be 1 cm for performing the optimization. This creates 121 points in the *x* direction, 31 points in the *y* direction, and 3751 points in total.

It is necessary to go through the entire workspace twice for a single set of design parameters. The first time is for determining the minimum required spine force, and the second time is for calculating the remaining dynamic performances. The process of evaluating the cost functions can be divided into three steps shown in this section.

It should be noted that the search for the best set of design parameters is different from the search in the workspace. The purpose of the optimization is to search for the best set of design parameters, and in order to compare different sets of design parameters, it is necessary to search through the entire workspace to calculate cost functions for each sets of design parameters. This section discusses the search in the workspace required to evaluate the cost functions. Optimization methods used for the search of the best set of design parameters are discussed in the next section.

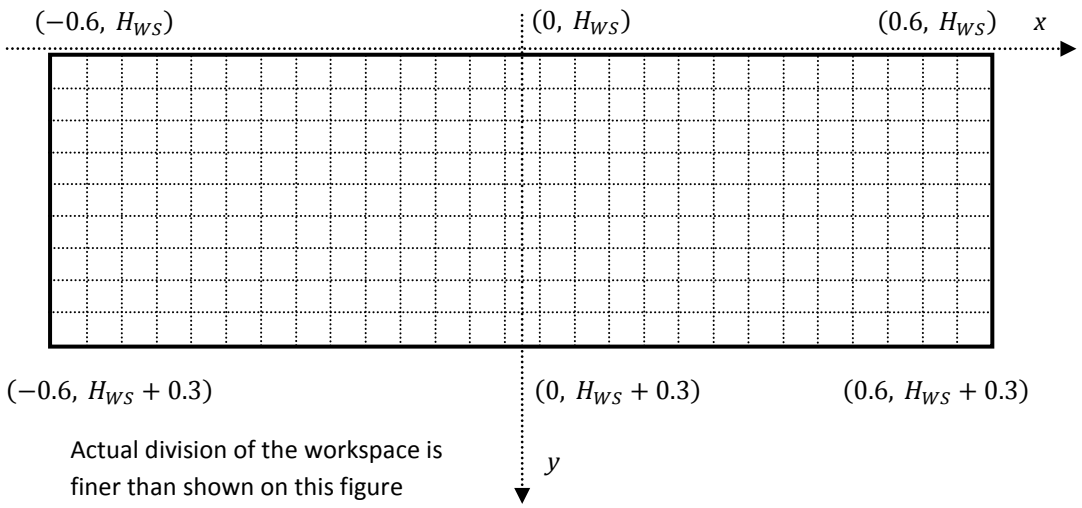

Figure 6-3: Workspace Divided into Data Points

6.2.1 Step 1: Workspace Verification

The first step is to check if the current set of design parameters can generate a large enough available workspace to fit the required workspace. The valid range for H_{WS} is also calculated for each set of design parameters. Figure 6-4 shows that the lower bound for H_{WS} is equal to L_A. The value of H_{WS} is increased by a small step until the upper bound is reached, where the bottom corners of the rectangular workspace is outside of the available workspace. This is checked with the inverse kinematic equation. If a specified (x, y) coordinate is outside of the available workspace, the solutions for θ_1 and θ_2 includes imaginary component. Every valid step of H_{WS} is considered as a candidates for the best set of design parameters.

Therefore, cost functions are evaluated for each one. If there is no valid value of H_{WS}, it means that the current set of design parameters does not have an available workspace large enough to fit the required workspace. In this case, the current set of design parameters is rejected immediately with the total cost function set to infinity. The majority of available combinations of design parameters are rejected in this first step. The cost function for size of the end-effector S_{area} can be calculated in this step.

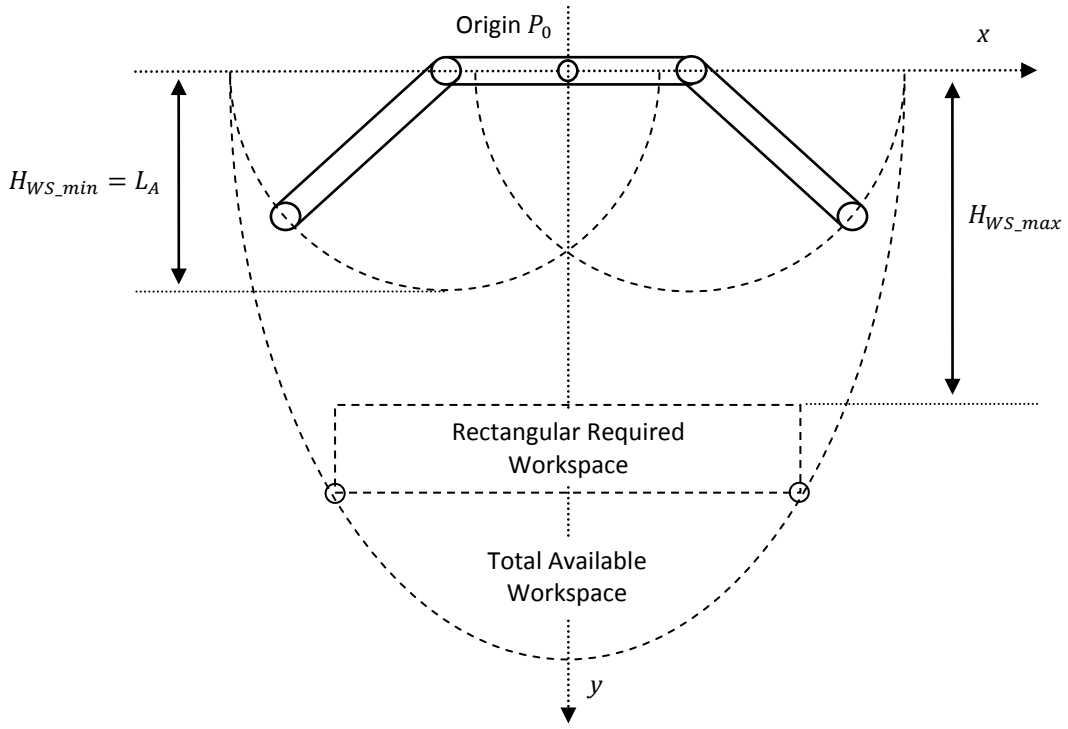

Figure 6-4: Lower Bound and Upper Bound for H_{WS}

6.2.2 Step 2: Evaluation of Minimum Required Spine Force

In this step, the entire workspace is examined for the first time and the following tasks are completed at each data point:

- Check for singularity between arms and cables.
- Evaluate matrices [A], $[M]$, $[C]$, and $\vec{B}$ for Equation (4.32) and store it step 3.
- Calculate the spine force required for minimum cable tensions of 15 *N*.

The following data are recorded for later use:

- Minimum and maximum values of θ_1 and θ_2 for mechanical design.
- Minimum required spine force.

Singularity between arms and cables occur when they are parallel to each other. In order to avoid the regions near singularity, the angles between the arm and the cable, Φ, is limited between 10 degrees to 170 degrees as shown in Figure 6-5. The value of Φ is calculated from the inverse kinematic equation, and if Φ is outside of the allowed limit, the current set of design parameters is rejected.

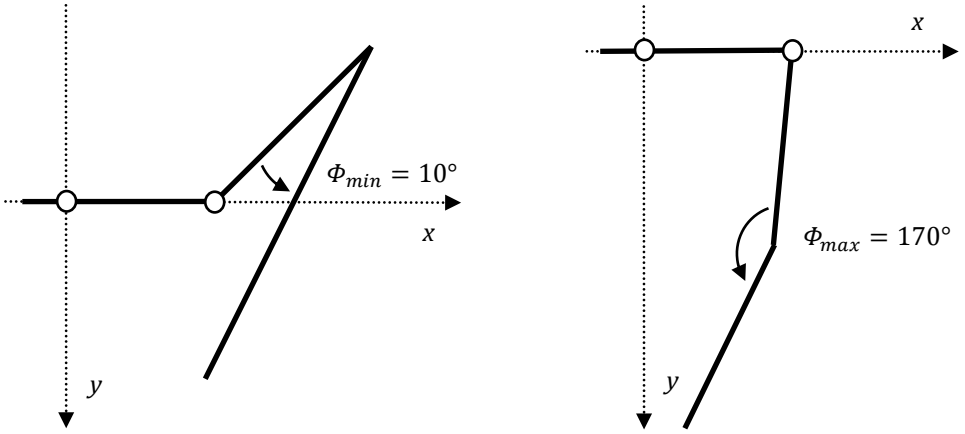

Figure 6-5: Limits for Angle between Arms and Cables

The values of θ_1 and θ_2 returned from the inverse kinematic equation are compared against previous data points to record the maximum and minimum values among the entire workspace. This data is used to determine the angle for neutral position discussed in Section 3.3.2 and shown in Figure 3-7.

Before continuing to the calculation of the minimum required spine force, it is necessary to have a method to determine the directions of acceleration and velocity that result in minimum and maximum cable tensions. Recall the expression for cable tensions from Equation (4.32):

$$\vec{T} = [A]^{-1}\left([M]\,\ddot{\vec{X}} + \dot{\vec{X}}^{T}[C]\,\dot{\vec{X}} + \vec{B}\right)$$

In order to maximize or minimize the value of $\vec{T}$, it is necessary to find $\ddot{\vec{X}}$ that maximize or minimize $[M]\,\ddot{\vec{X}}$, and also find $\dot{\vec{X}}$ that maximizes or minimizes $\dot{\vec{X}}^{T}[C]\,\dot{\vec{X}}$. The maximum magnitudes for both of them are already defined in the design specifications, and therefore only their directions need to be found. By the principal axis theorem, the maximum value of $[M]\,\ddot{\vec{X}}$ occurs when $\ddot{\vec{X}}$ is in the direction of Eigen-vector associated with the largest Eigen-value of $[M]$. Then, the minimum value of $[M]\,\ddot{\vec{X}}$ occurs when $\ddot{\vec{X}}$ is in the negative direction of the same Eigen-vector. Similarly, the maximum value of $\dot{\vec{X}}^{T}[C]\,\dot{\vec{X}}$ occurs when $\dot{X}$ is in the direction of Eigen-vector associated with the largest Eigen-value of $[C]$. Since $\dot{\vec{X}}$ is multiplied twice it is similar to squaring $\dot{\vec{X}}$, then the minimum value of $\dot{\vec{X}}^{T}[C]\dot{\vec{X}}$ occurs when $\dot{\vec{X}}$ is in the direction of Eigen-vector associated with the smallest Eigen-value of $[C]$. Let $\ddot{\vec{X}}_{max}$, $\dot{\vec{X}}_{max}$ and $\ddot{\vec{X}}_{min}$, $\dot{\vec{X}}_{min}$ represent accelerations and velocities that maximize or minimize the cable tensions.

In Equation (4.35), the spine force $\vec{F}_C$ is part of the constant $\vec{B}$ matrix. Increasing the spine force in this equation results in a monotonic increase in the cable tensions. The equation indicates that there are linear relationships between the spine force and cable tension for each cable. If two points are known on this relationship, it is possible to derive the equation of the line and interpolate any other points on this line. One way to calculate the minimum required spine force is to first find the cable tensions at two random spine forces (for example 0 *N* and 500 *N*), and then use interpolation to find the spine force where the cable tension is 15 *N* as shown in Figure 6-6.

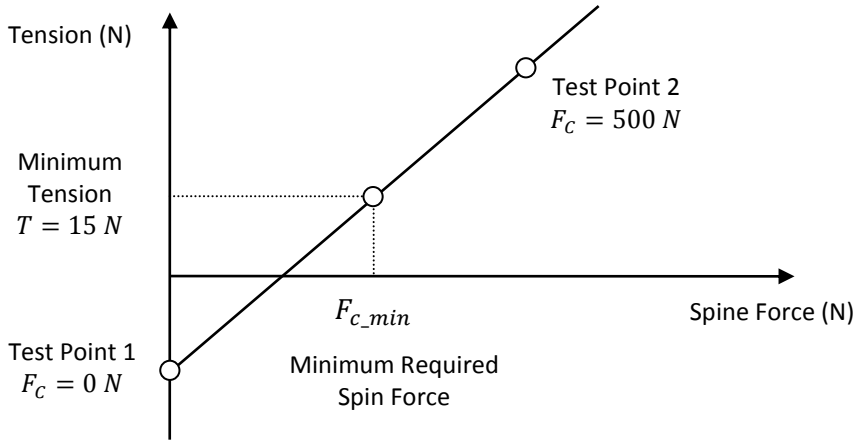

Figure 6-6: Linear Relationship between Spine Force and Cable Tensions

The interpolation method requires the calculation of matrix $\vec{B}$ twice for each test point, and then one more time at the end for the minimum required spine force. An alternative method is proposed here that only requires calculation of the B matrix once for the entire process:

Method for Calculating Minimum Required Spine Force

1. Let $\hat{u}_{F_C}$ be the direction unit vector of F_C, and let B_0 be B matrix without any component of F_C.

$$\hat{u}_{F_C} = [\ \hat{u}_{F_{C\_x}}\quad \hat{u}_{F_{C\_y}}\quad 0\quad 0\quad 0\quad 0\ ]^T \tag{6.2}$$

$$\vec{B} = \vec{B}_0 + \vec{F}_C\ \hat{\mathrm{u}}_{\mathrm{F_C}} \tag{6.3}$$

2. Calculate Matrices $[A]$, $[M]$, $[C]$, $\vec{B}_0$, and $\hat{u}_{F_C}$ at each data point, and store it for later use.

3. Formulate the following equation to be the cable tensions at $\vec{F}_C = 0$. Calculate the minimum values for $\vec{T}_0$ using $\ddot{\vec{X}}_{min}$ and $\dot{\vec{X}}_{min}$ discussed in the previous page.

$$\vec{T}_0 = [A]^{-1}\left([M]\ \ddot{\vec{X}}_{min} + \dot{\vec{X}}_{min}^{\ T}\ [C]\ \dot{\vec{X}}_{min} + \vec{B}_0\right) \tag{6.4}$$

4. Let $\vec{T}_{min}$ be a vector of minimum required cable tensions.

$$\vec{T}_{min} = [\ 15\ N\quad 15\ N\quad 15\ N\quad 15\ N\quad 15\ N\quad 15\ N\ ]^T \tag{6.5}$$

5. Let $\vec{F}_{C\_15N}$ be a vector of spine forces that gives 15 *N* of tension on each cables. For example, the first term in $\vec{F}_{C\_15N}$ is the spine force required to give 15 *N* of tension on cable number 1.

$$\vec{F}_{C\_15N} = \left[\vec{F}_{C\_15N\_cable\_1} \quad \vec{F}_{C\_15N\_cable\_2} \quad \cdots \quad \vec{F}_{C\_15N\_cable\_6} \right]^T \tag{6.6}$$

6. Formulate the following equation using T_{min} and F_{C_15N}.

$$\vec{T}_{min} = [A]^{-1}\left([M]\,\ddot{\vec{X}}_{min} + \dot{\vec{X}}_{min}{}^{T}\,[C]\,\dot{\vec{X}}_{min} + \left(\vec{B}_0 + \vec{F}_{C\_15N}\,\hat{u}_{F_C}\right)\right) \tag{6.7}$$

7. Combine Equation (6.4) with Equation (6.7), and then rearrange to solve for $\vec{F}_{C\_15N}$.

$$\vec{F}_{C\_15N} = \frac{\vec{T}_{min} - \vec{T}_0}{[A]^{-1}\,\hat{u}_{F_C}} \tag{6.8}$$

8. The minimum required spine force for each data point is the largest value in $\vec{F}_{C\_15N}$.

$$F_{C\_\min\ \_dp} = max\left(\vec{F}_{C\_15N}\right) \tag{6.9}$$

9. The minimum required spine force for the entire workspace is the largest value of $\vec{F}_{C\_\min\ \_dp}$.

$$F_{C\_min} = max\left(F_{C\_\min\ \_dp}\right) \tag{6.10}$$

10. After F_{C_min} is determined, calculate the $\vec{B}$ matrix at each data point using Equation (6.3), and store it in memory for later use.

$$\vec{B} = \vec{B}_0 + F_{C\_min}\,\hat{u}_{F_C} \tag{6.11}$$

6.2.3 Step 3: Evaluation of Dynamic Performances and Stiffness

The third and last step examines the entire workspace for the second time to complete the following tasks at each data point:

- Calculate cable tensions.
- Calculate static torque, dynamic torque, and angular velocity.
- Evaluate minimum stiffness matrix and check for stability
- Calculate out-of-plane displacement under 40 *N* of force in the *z* direction.

The following data are recorded:

- Maximum value of cable tension.
- Maximum values of static torque, dynamic torque, and angular velocity.
- Maximum value of out-of-plane displacement.

The maximum cable tension at each data point is calculated using Equation (4.32) with $\ddot{\vec{X}}_{max}$ and $\dot{\vec{X}}_{max}$, and matrices $[A]$, $[M]$, $[C]$, and $\vec{B}$ are stored in memory from step 2. The maximum cable tension for each data point is the largest value among all the cables in the $\vec{T}$ vector. The maximum cable tension for the entire workspace is the largest value of cable tension among all the data points.

$$T_{\min\ \_dp} = max(\vec{T}) \tag{6.12}$$

$$T_{min} = max(T_{\min\ \_dp}) \tag{6.13}$$

The gradient of the inverse kinematic equation shown in Equation (4.2) is calculated at each data point, and then the maximum angular velocity at each data point is calculated using the gradient and $\dot{X}_{max}$. For calculating maximum static torque, maximum static cable tension is recalculated without the dynamic components ($\ddot{X} = 0,\ \dot{X} = 0$), and then Equations (4.37) or (4.38) for calculating motor torque are used with maximum static cable tension and maximum angular velocity. Similarly, maximum dynamic torque is calculated using the same equations with maximum dynamic cable tension and maximum angular velocity. The largest value for each one of these motor dynamic performances in the entire workspace is used for the cost functions.

In order to find the largest out-of-plane displacement, it is necessary to find minimum stiffness matrix that occurs when the cable tensions are minimum, which is calculated using Equation (4.32) with $\ddot{\vec{X}}_{min}$ and $\dot{\vec{X}}_{min}$, and matrices $[A]$, $[M]$, $[C]$, and $\vec{B}$. The stiffness matrix is calculated based on these minimum cable tensions, and then the out-of-plane displacement is calculated using Equations (5.65) and (5.71) with 40 *N* applied in the *z* direction.

6.3 Options for Optimization Methods

The challenge in optimization for the best set of design parameters is that there are multiple cost functions to consider simultaneously. This type of optimization problem is classified as a multi-objective optimization. It was proposed in Section 6.2 to sum all individual cost functions into a single total cost function with Equation (6.1), but it is difficult to assign appropriate weights and normalization factors for each cost function. This section presents four optimization methods that were considered for the search of the best set of design parameters. Brief introductions are given for each optimization method, and their advantages and disadvantages with respect to the challenge in assigning weights and normalization factors are discussed. This thesis does not show detailed algorithms or implementation steps for the four optimization methods because that is out of scope of this thesis. The methods presented in this section are all well-known optimization strategies, and there are abundance of literature surrounding their algorithms and implementations.

6.3.1 Option 1: Nelder-Mead (Direct Search)

The problem space of the optimization for the best set of design parameters is highly nonlinear due to having multiple cost functions. The Nelder-Mead method, or otherwise known as the downhill simplex method, is a common derivative-free nonlinear optimization method. This method was used by Edmon Chan in his optimization for the previous design of the 2D cable-based manipulator [1]. The method defines a polygon with $N + 1$ vertices in N dimensions, where N is the number of optimization parameters. For example, this polygon would be a triangle on a plane, and tetrahedron in a three dimensional space. The cost function is evaluated at each vertex, and then the vertex with the highest cost is moved to an another point in the problem space, usually toward and through the centroid of the remaining N points in an attempt to reduce the cost. This process moves the polygon in the problem space until most of the vertices converge at a local minimum. Figure 6-7 shows a sample step in the search process of the Nelder-Mead method for a 2D problem.

The Nelder-Mead method is one of the most simple and well-defined optimization algorithm, and it is easy to implement. However, there are several disadvantages associated with this method. The time required for optimization increases proportionally to the number of optimization parameters, which makes this method not suitable for a large number of optimization parameters. This method works best when the optimization space is smooth and unimodal, but this is not the case with multiple nonlinear cost functions. There could be many potential local minima that trap the polygon and prevent this method from finding the global minimum. Edmon Chan addressed this problem by using multiple starting points distributed evenly across the entire problem space, but this significantly increases the optimization time. Finally, this method does not address the problem with assigning weights and normalization factors at all.

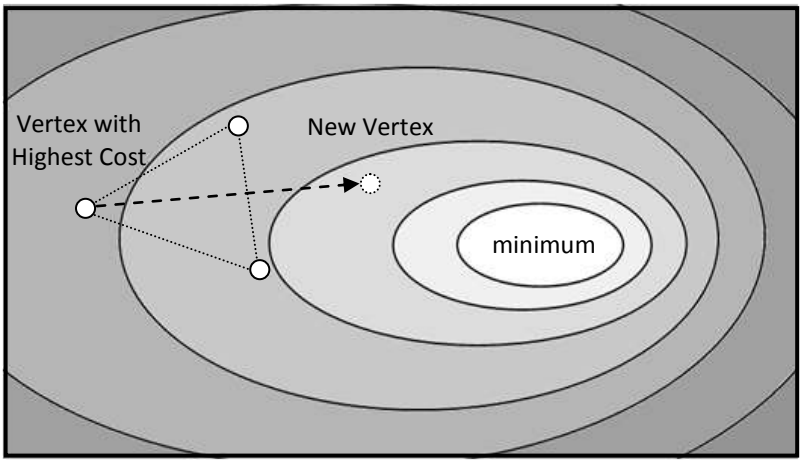

Figure 6-7: Searching Process of Nelder-Mead Method – 2D Example

6.3.2 Option 2: Genetic Algorithm (Stochastic Search)

The Genetic Algorithm method solves optimization problems by emulating population propagation and the concept of the "*survival of the fittest*". The optimization parameters are modelled as genes or chromosomes of a population of candidates. In the beginning, a population of candidates are created with randomly selected genes. Then, each candidate in the population is evaluated for its fitness based on the cost function, and half of the population with poor fitness is removed. The remaining population

reproduces children to take the place of the removed candidates. In the reproduction phase, two parent candidates form a pair and create two child candidates by mixing their genes; this process is called crossover. The most simple crossover method is shown in Figure 6-8. After the reproduction phase, a small portion of the population goes under mutation to randomly change their genes, which adds randomness in the optimization method to help it escape from local minima. This cycle of selection, reproduction, and mutation is continued until majority of the population converges to a similar gene.

The strength of Genetic Algorithm is its ability to avoid being trapped in local minima using the random mutation phase. This makes Genetic Algorithm well suited for solving the optimizations with highly nonlinear problem space such as the search for the best set of design parameters. However, due to the randomness of the algorithm, it is still good idea to run the optimization several times and compare the solutions for convergence. A challenge in Genetic Algorithm is that the user must define many parameters for the algorithm, such as the population size, method of crossover, and frequency of mutation. This is not simple without some experience, but there is software available with Genetic Algorithm tools such as MATLAB that will take care of these parameters. This method still does not address the problem with assigning weights and normalization factors to the cost functions.

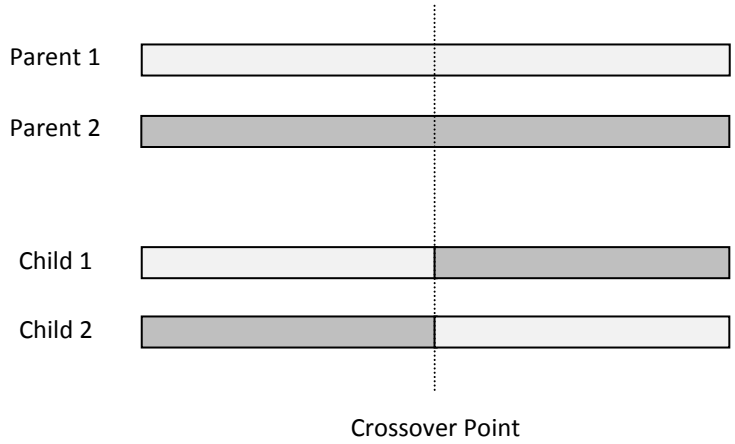

Figure 6-8: One-Point Crossover Method for Genetic Algorithm

6.3.3 Option 3: NSGA-II (Multi-Objective Search)

NSGA-II stands for “Non-dominated Sorting Genetic Algorithm”, and it is a an extension to the Genetic Algorithm method that is specifically designed to solve multi-objective optimization problems. This method simultaneously optimizes two or more conflicting objectives to find points where improving an objective would make other objectives worse. This point is called Pareto point, and there are many Pareto points in a multi-objective optimization problem. Therefore, NSGA-II gives multiple valid solutions to the problem.

The advantage of NSGA-II is that it handles multi-objective optimization problems without specifying weights or normalization factors. However, the lack of necessity for decision making prior to the optimization process creates a problem later, when selecting one of many solutions given by the NSGA-II method. Therefore, it is still unavoidable to have some human decision making in the optimization process. In the case of the NSGA-II method, the decision making part is simply delayed until the end of the optimization algorithm.

6.3.3 Option 4: Complete Search

Complete Search is an optimization method where every single combination of optimization parameters are examined. It uses brute force to explore the entire problem space, and therefore it is guaranteed to find the global minimum. Although this is not an elegant solution, it does have important advantages compared to other optimization methods.

A problem space can have multiple regions of good solutions. Since Complete Search examines the entire problem space, it can identify these multiple regions similar to multiple Pareto points in NSGA-II. The Nelder-Mead method and Genetic Algorithm method both lack the ability to provide any information other than the final solution, and there is no easy way to examine other good regions or explore parameter

sensitivity without a sensitivity analysis. Even for NSGA-II, there may be some solutions better than any Pareto points in the opinion of human eyes.

In Complete Search, it is not necessary to come up with a single total cost function. It is sufficient to only calculate each individual cost function and organize the results in a spreadsheet for a human to examine. This is not possible for other optimization methods such as Nelder-Mead or Genetic Algorithm, since a total cost function is required to run these algorithms. It was concluded that human decision-making is unavoidable in the optimization of design parameters. The Complete Search method uses the most basic search algorithm and relies completely on human decision making for selecting the best set of design parameters. Since information about the entire problem space is available for human eyes, this method guarantees to find a solution desired by a human.

There are two obvious disadvantages to the Complete Search method. It takes a tremendous amount of time to compute solutions for the entire problem space, and there is large amount of data for a human to examine. However, there are ways to address both disadvantages. The computation time is significantly reduced by modern computing technology with high clock speeds and multi-core processors. It is possible to divide the problem space and run multiple instances of the computation program in separate threads, or even use multiple computers since they are widely available. The amount of valid solutions is significantly reduced during the evaluation of cost functions due to kinematic verification and dynamic limits. When the human examines the remaining results, it is still useful to rank them with a total cost function. The normalization factor for each cost functions can be set to the highest value of that particular cost function in the entire problem space. Weight for each cost function can be arbitrary chosen and changed at any time. Since all the results are organized in a spreadsheet, it is very fast to calculate the maximum of a cost function or to see the effect of changing the value of a weight. This allows a human to experiment with the results and identify multiple regions of good solutions.

6.4 Optimization Result and Final Design

6.4.1 Optimization Process and Result of Each Method

The Complete Search method was chosen to be tested first for the search for best set of design parameters, because it is the simplest to implement and it can provide general idea on how to choose appropriate weights and normalization factors. The search program was implemented in MATLAB, and it was run on a relatively powerful computer with quad-core processor and 8 available threads. The entire search was separated into two sessions, with each session covering half of the entire problem space. Six instances of the search program were run at the same time in each session. The search process took approximately 8 hours to complete, which is a very long time but certainly not unreasonable. The Complete Search method is viable for this particular optimization problem, and benefits provided by it outweigh the long search time.

After the Complete Search method was completed, results were organized in a spreadsheet and inspected manually. In order to identify good solutions, a total cost function was created with the weights listed in Table 6-2 and the maximum value of each cost function as normalization factors. The absolute best solution according to the total cost function had cable length of 1.8 *m*, which was impractically long. However, there were other solutions with cable length of around 1.3 *m* and comparable dynamic performances. This illustrates the problem with assigning weights on a multi-objective optimization problem. The current set of weights made the total cost function choose negligible increases in dynamic performance over unreasonably large increases in the cable length. It is obvious to a human that the solution with shorter cable length and similar dynamic performances is more preferred, and the weights need to be modified to increase the importance of manipulator size. This kind of information is easily identifiable in the Complete Search method, but it is hidden in Nelder-Mead or Genetic Algorithm methods because these only give a single solution.

Nelder-Mead, Genetic Algorithm, and NSGA-II, were also tested for experimental purposes. The weights for the cost functions were changed based on the result of the Complete Search method. In order to avoid an unreasonably long cable, the weight for size of manipulator was increased, and also the evaluation of cost function itself was changed to put more emphasis on the length of cable instead of the total area. The new set of weights was designed to select the most preferred solution identified in the Complete Search method as the highest ranking solution. Choosing new values for the weights is simple because it is fast to recalculate the total cost function in the spreadsheet.

The Nelder-Mead method took the longest time to complete because it was necessary to perform the search from multiple starting locations. It was able to identify the same preferred solution from the Complete Search method as long as the starting location was not too far from the solution. The Genetic Algorithm method had the best performance. The method was tested 5 times in total, and it was able to find the preferred solution in less than an hour every single time. If appropriate weights and normalization factors were known beforehand, Genetic Algorithm would definitely the best optimization method out of the four options considered. NSGA-II took about 2 hours to complete with a variety of Pareto points that were mostly unreasonable. Some solutions were close to the final solution from the Complete Search method, but they were less preferred in terms of the trade-off between cable length and dynamic torque, which is information is only available in the Complete Search method.

6.4.2 Final Design Parameters and Performances

Table 6-3 shows the final set of design parameters selected based on the Complete Search method. The arm length is close to the upper bound of the search range because longer arms increases available workspace and reduces maximum angular velocity. The cable separation distance at the arms (L_{AS}) is almost always at its maximum value for good solutions, because it increases stiffness in the out-of-plane direction while having very little effect on dynamic costs. This means that larger value for L_{AS} is almost always better, but it is limited at 0.30 *m* since it is not desirable to have a large out-of-plane profile for the

manipulator. This set of design parameters is attractive because it has the shortest cable length and starting height of workspace out of all the good solutions while having competitive dynamic performances. This set of design parameters offers the best ratio between size of the manipulator and dynamic performances.

Table 6-3: Design Parameters for the Final Design

Parameter	Value
L_B	$0.31\ m$
L_A	$0.48\ m$
L_C	$1.30\ m$
L_E	$0.20\ m$
L_{AS}	$0.30\ m$
L_{ES}	$0.10\ m$
H_{WS}	$1.10\ m$

Table 6-4 shows the dynamic performances associated with the final set of design parameters. The maximum dynamic torque is close to the motor limit of $300\ N \cdot m$, but this is still one of the best solutions. It was noticed during the Complete Search method that very few solutions had their maximum dynamic torque under the limit, and majority of the solutions were rejected due to going over the limit.

Table 6-4: Dynamic Performances for the Final Design

Cost	Description	Value
F_{C_min}	minimum required spine force	$314\ N$
T_{max}	maximum cable tension	$130\ N$
τ_{st_max}	maximum static torque	$142\ N \cdot m$
τ_{dy_max}	maximum dynamic torque	$285\ N \cdot m$
$\dot{\theta}_{max}$	maximum angular velocity	$142\ rpm$

Figure 6-9 shows the distribution of maximum dynamic torque in the workspace. It can be observed that the maximum dynamic torque is close to the motor limit of 300 $N \cdot m$ throughout majority of the workspace. This is troublesome because 300 $N \cdot m$ is the absolute peak limit, and the actual rated motor torque is 146 $N \cdot m$ at rated current of 6 A. Note that this graph shows the absolute worst case defined by $\ddot{\vec{X}}_{max}$ and $\dot{\vec{X}}_{max}$, where the arms are most likely moving vertically at maximum acceleration and velocity. In a normal pick-and-place operation, it is very rare to reach this absolute worst case. However, Figure 6-10 shows the distribution of maximum static torque in the workspace, and it also indicates trouble for the torque limit. This graph shows that the static torque is already close to the rated torque of 146 $N \cdot m$ throughout most of the workspace. This suggests that as soon as the end-effector starts moving, the motors will go over their rated torque, and this is a normal case scenario instead of the worst case. Usually at this point, the design should be revised or more powerful motors should be considered. However, due to the budget limit at the time of this project, it was decided to use the current motors for prototyping and replace it later when the budget allows. The implication of this decision to the performance of the manipulator is discussed in the next Chapter.

Figure 6-11 shows the distribution of minimum cable tension in the workspace for static case. Showing maximum cable tension would not be useful because the upper limit for cable tension is very high. On the other hand, the distribution of minimum cable tension can show where in the workspace the manipulator is closest to losing tension on one of the cables. The lowest cable tension occurs at bottom right of the workspace for the static case. The graph shows that tension for at least one of the cable drops to 52 N around this region. Figure 6-12 shows the distribution of minimum cable tension in the workspace for dynamic cases. This graph shows that low cable tension can happen nearly everywhere in the workspace under the worst case defined by $\ddot{\vec{X}}_{min}$ and $\dot{\vec{X}}_{min}$.

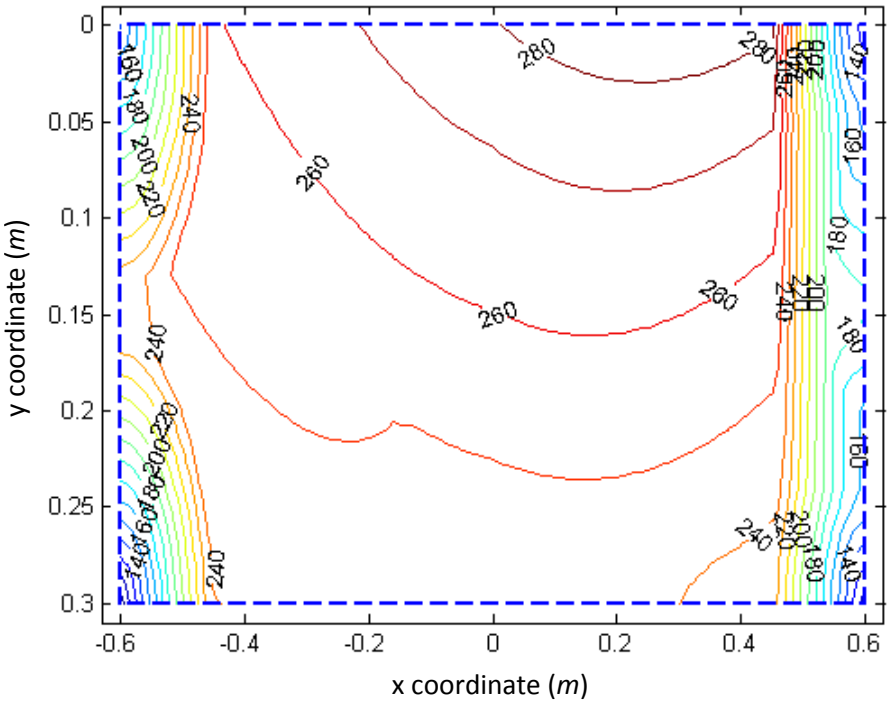

Figure 6-9: Distribution of Maximum Dynamic Torque (*N-m*)

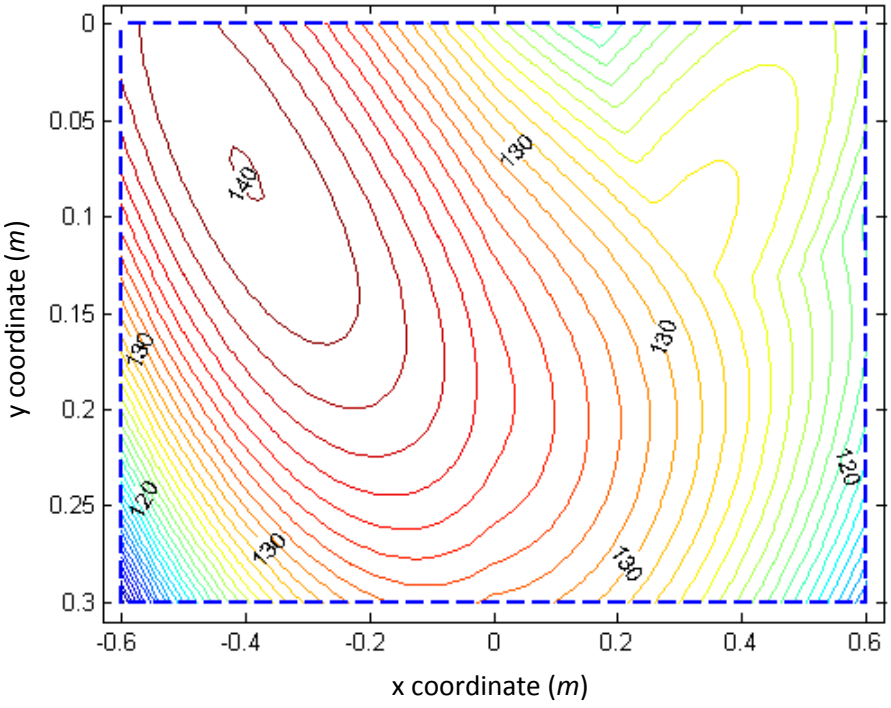

Figure 6-10: Distribution of Maximum Static Torque (*N-m*)

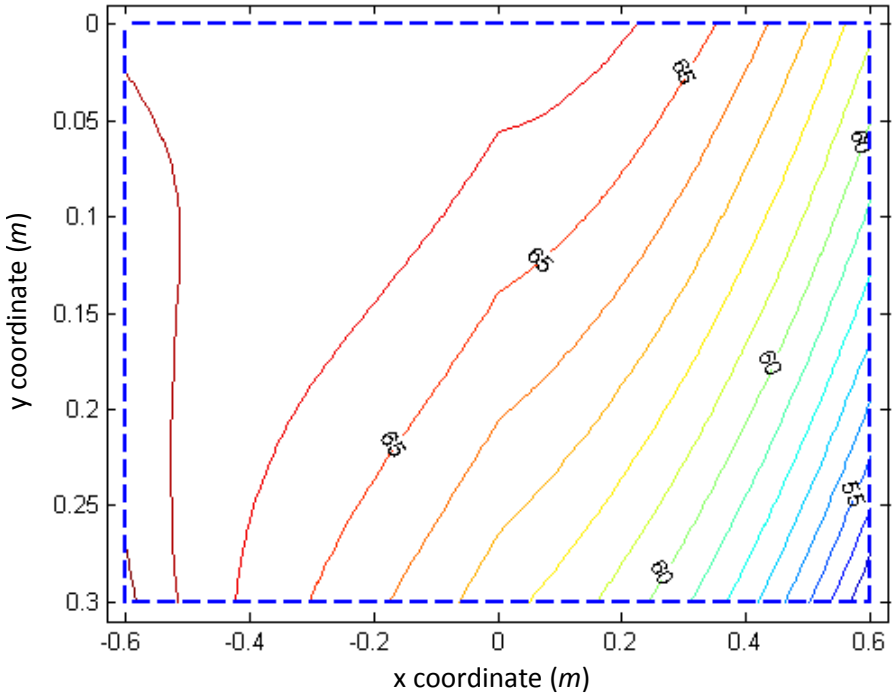

Figure 6-11: Distribution of Minimum Cable Tension for Static Case (*N-m*)

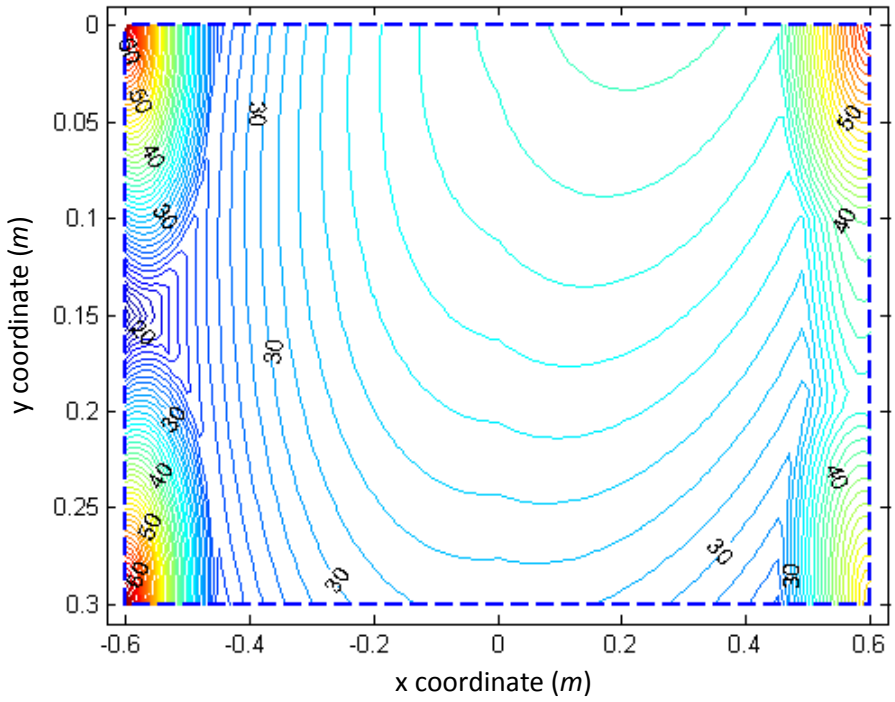

Figure 6-12: Distribution of Minimum Cable Tension for Dynamic Case (*N-m*)

Figure 6-13 shows the complete stiffness matrix of the end-effector with the final set of design parameters at a sample position of ($x = 0,\ y = 0.15$), which is at the exact center of the workspace. The main components of translational stiffness in the *x* direction and *z* direction are bolded. Table 6-5 shows the displacement of the end-effector in the *z* direction caused by various magnitudes of applied forces in the *z* direction. The end-effector is estimated to move 2.8 *mm* under 40 *N* of applied force. However, the calculation for valid range of stiffness discussed in Section 5.3 estimates that at least one of the cables will lose tension under 23 *N* of applied force. Therefore, the estimated displacements under 30 *N* and 40 *N* in Table 6-5 may not be valid. The valid range of stiffness of 23 *N* is still acceptable, because the external force in the out-of-plane direction is not expected to be that large.

$$[K] = 10^6 \times \begin{bmatrix} \mathbf{0.5411} & -0.2490 & 0 & 0 & 0 & 0 \\ -0.2490 & 1.0687 & 0 & 0 & 0 & 0 \\ 0 & 0 & \mathbf{0.0143} & 0 & 0 & 0 \\ 0 & 0 & 0 & 0.0009 & -0.0006 & 0 \\ 0 & 0 & 0 & -0.0006 & 0.0007 & 0 \\ 0 & 0 & 0 & 0 & 0 & 0.0111 \end{bmatrix}$$

Figure 6-13: Stiffness Matrix for the Final Design

Table 6-5: Displacement of the End-Effector for the Final Design

	Applied Force in *z* direction (*N*)			
	10	20	30	40
δ_z (m)	0.7002×10^{-3}	0.0014	0.0021	0.0028

Finally, the maximum value and minimum value for θ_1 and θ_2 for the final set of design parameters are recorded to be 88.42 degrees and -23.49 degrees. Therefore, the angle for the neutral position of the parallelogram structure on the right side arm (discussed in Section 3.3.2) is the midpoint between the maximum and minimum angle, which evaluates to 32.46 degrees.

Chapter 7

Prototyping and Experimental Results

7.1 Mechanical Design of the Prototype

Figure 7-1 and Figure 7-2 show the CAD model of the mechanism designed based on the final set of design parameters. The CAD model is created by partners from Conestoga College. There are some aesthetic changes to the shape of the arms and triangle structure on the right side to make them look similar to other cable-based manipulators designed and built by AEMK System. These changes do not affect the kinematics of the manipulator, since the distances between all the joints remains the same.

In the early stage of testing, the spine force was limited to approximately 260 N before the motor faulted due to a torque limitation, which is less than the theoretically planned 314 N. One of the problems caused by this issue is less tension in the cables and reduced stiffness. In order to reinforce the stiffness in the out-of-plane direction, additional parts were designed to be installed at the upper universal joint of the pneumatic cylinder as shown in Figure 7-3. These add-on parts contain a revolute joint that acts as an additional mechanical constraint that prevents out-of-plane movement, while the inner universal joint still allows the transmission of rotation between the 3rd motor axis and cylinder axis. The weakness of a mechanical stiffness is that any small displacement at the upper universal joint can be amplified at the end-effector due to the long pneumatic cylinder. Large 20 mm diameter clevis pins are used to minimize the amount of backlash.

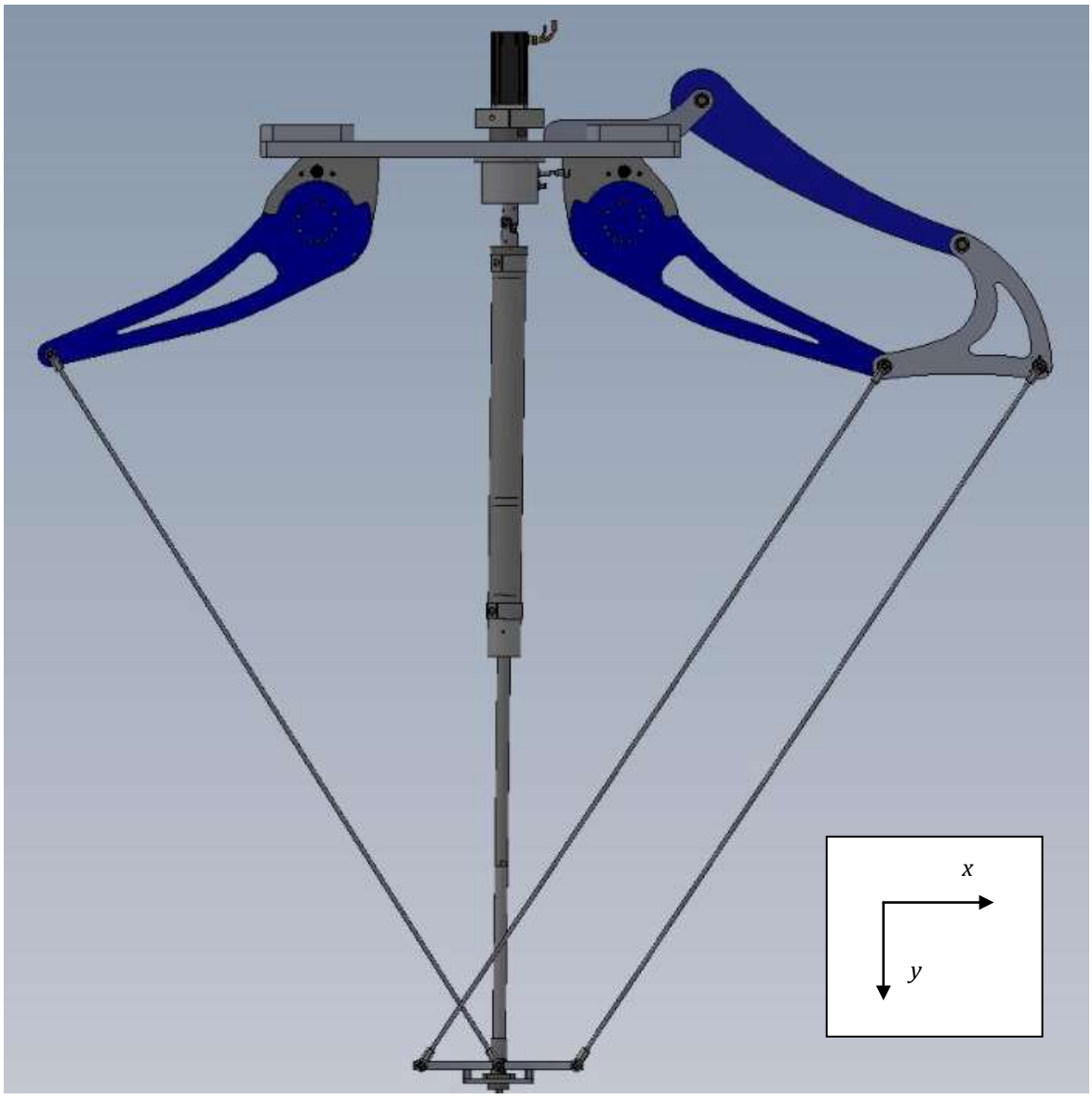

Figure 7-1: CAD Model of the Mechanical Design (Front View)

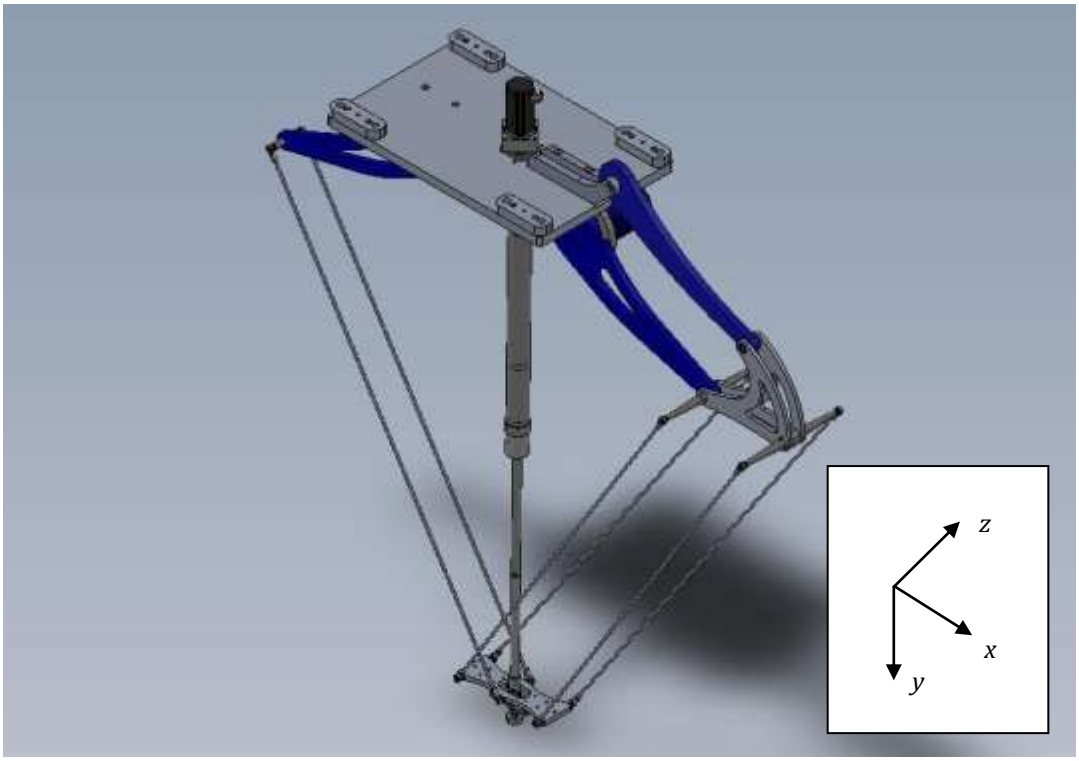

Figure 7-2: CAD Model of the Mechanical Design (Isometric View)

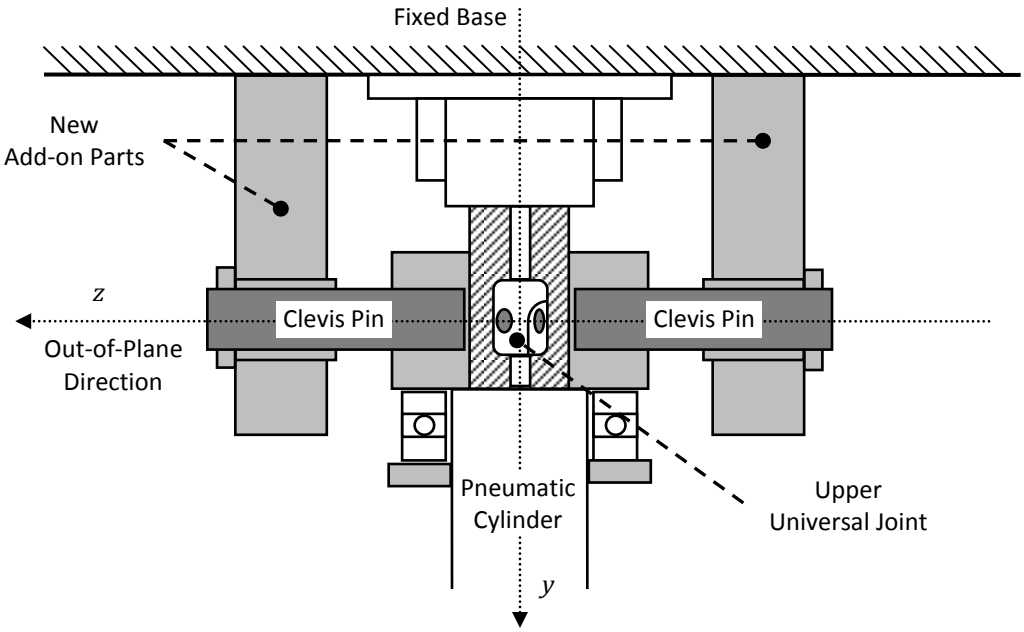

Figure 7-3: Add-on Parts at the Upper Universal Joint

Figures 7-4 shows a photograph of the fully assembled manipulator with the outer mounting frame. The manipulator is controlled with BeckHoff control system and TwinCAT PLC program. The control program is based on an existing program written for a 3D cable-based manipulator created by AEMK System. On top of the fixed base, there are pneumatic parts for the cylinder and suction cup. The photograph shows that there are some air hoses running to the pneumatic cylinder. Figure 7-5 shows a photograph of the control box and workstation for the manipulator. The control box contains three BeckHoff motor drivers, PLC module, a power supply unit, and a computer running TwinCAT control software. Figure 7-6 shows a photograph of the end-effector.

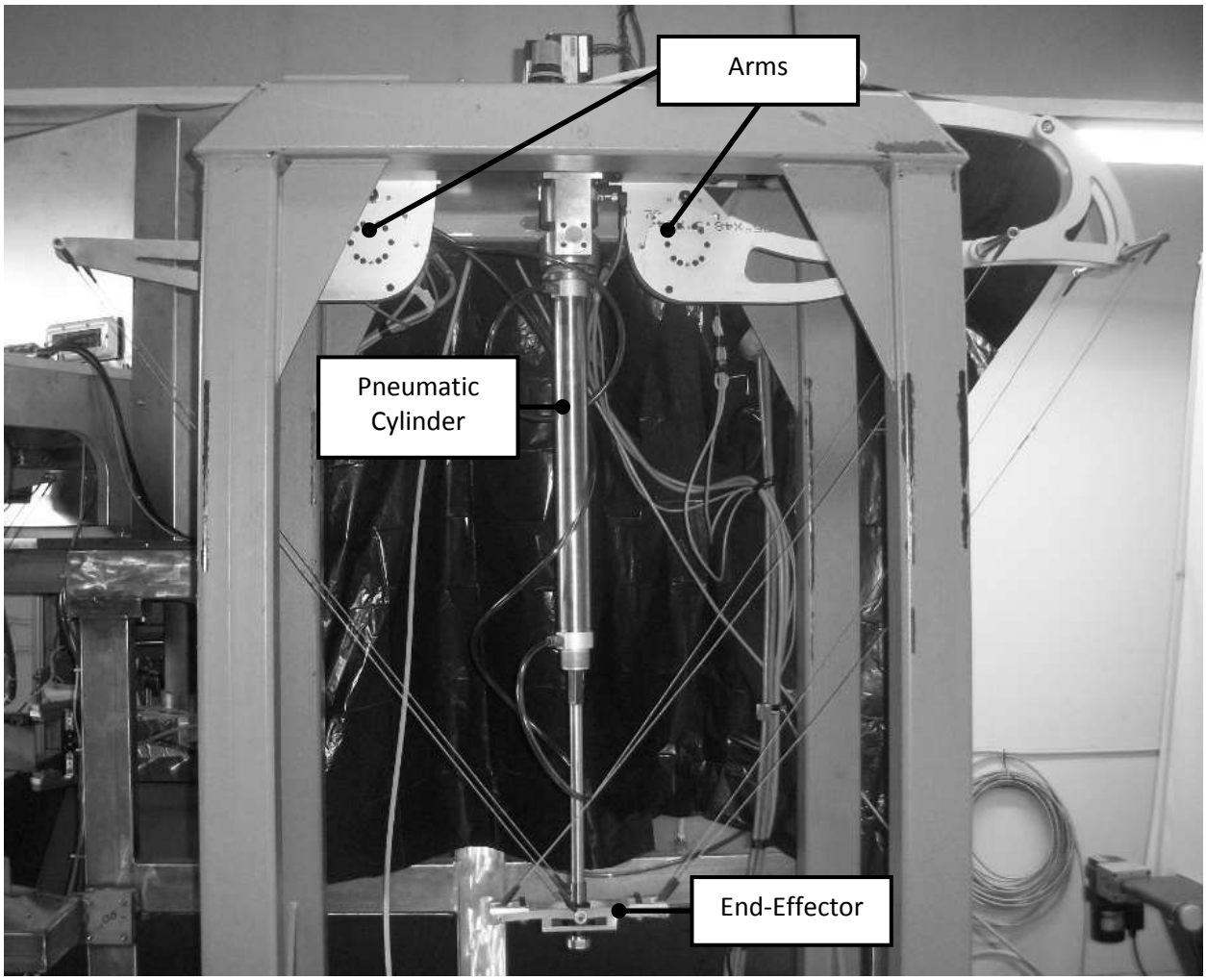

Figure 7-4: Photograph of the Manipulator

Figure 7-5: Photograph of the Control Box

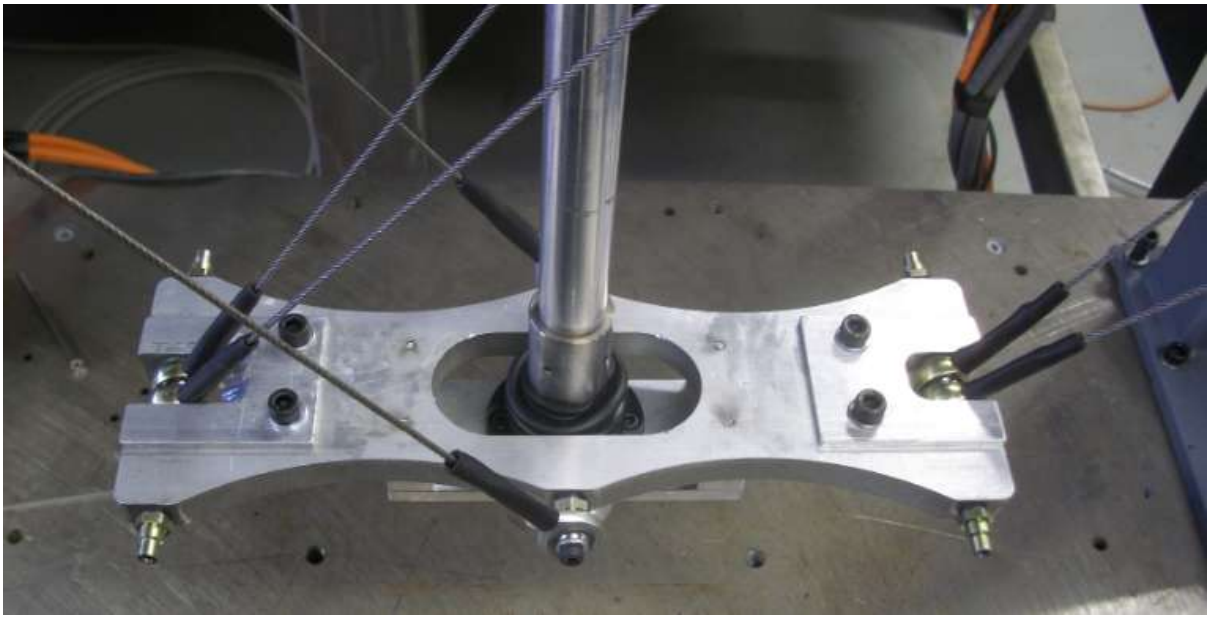

Figure 7-6: Photograph of the End-Effector

7.2 Experimental Results

7.2.1 Torque Measurement

It was mentioned in the previous section that the spine force can only supply up to approximately 260 *N* instead of the originally planned 314 *N*, due to the limitation with the motors. This reduces the amount of tension in the cables and also reduces the amount of static torque. Figure 7-6 shows the new distribution of maximum static torque in the workspace with a spine force of 260 *N*. In order to verify the static torque calculation, the end-effector was moved to various locations in the workspace and measured motor torques were compared with calculated motor torques in Table 7-1. It can be observed that the values in Figure 7-6 and the calculated values are reasonably close to the measured values. The measured values were consistently lower than the calculated values. This most likely suggests that the value of the spine force estimated from the air pressure was higher than the actual value, because the spine force contributes for most of the static torques.

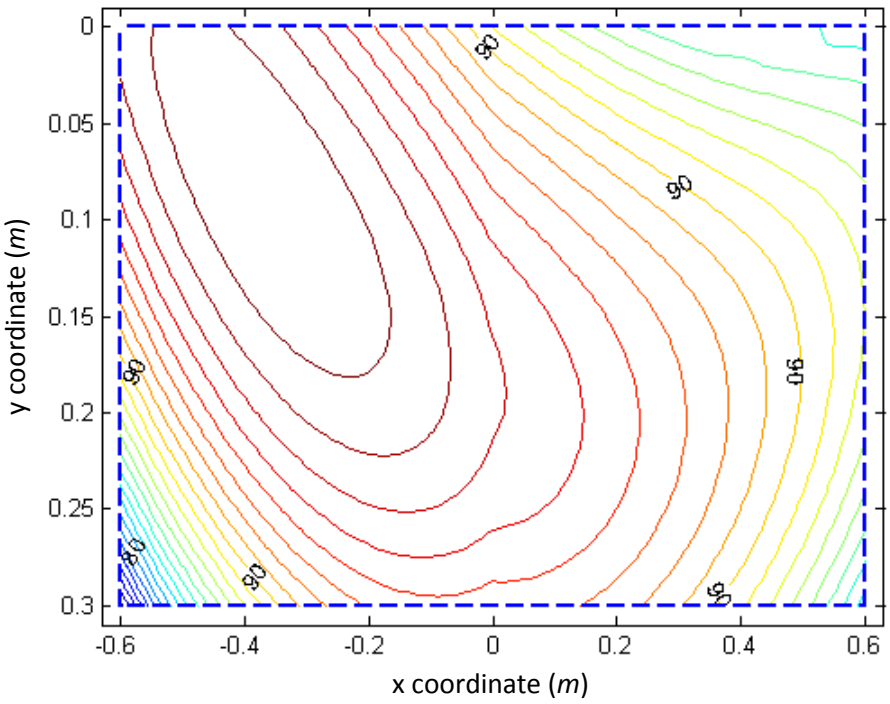

Figure 7-6: New Distribution of Maximum Static Torque (*N-m*)

Table 7-1: Measured Static Torque vs. Calculated Static Torque

Left Motor		Right Motor	
Calculated Toque	Measured Torque	Calculated Toque	Measured Torque
87.0 $N \cdot m$	78 .5 $N \cdot m$	91.8 $N \cdot m$	88.3 $N \cdot m$
87.3 $N \cdot m$	84.6 $N \cdot m$	93.6 $N \cdot m$	83.6 $N \cdot m$
73.8 $N \cdot m$	69.1 $N \cdot m$	99.4 $N \cdot m$	97.8 $N \cdot m$
88.2 $N \cdot m$	77.5 $N \cdot m$	97.0 $N \cdot m$	95.1 $N \cdot m$
94.5 $N \cdot m$	85.9 $N \cdot m$	105.3 $N \cdot m$	95.7 $N \cdot m$
86.4 $N \cdot m$	82 .2 $N \cdot m$	103.5 $N \cdot m$	91.5 $N \cdot m$

Next, the measured dynamic torques and calculated dynamic torques are compared. Figure 7-7 shows the movement of the end-effector in *x* and *y* axis with respect to time for a sample pick-and-place path. Figure 7-8 shows the movement of the end-effector in the workspace for the same path.

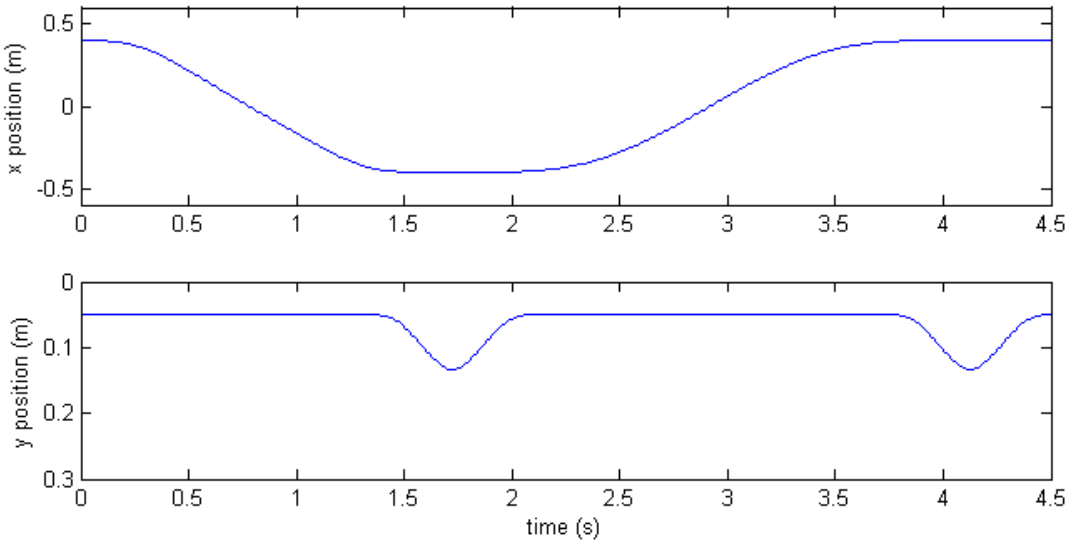

Figure 7-7: Movement of the End-Effector with respect to Time for a Sample Path

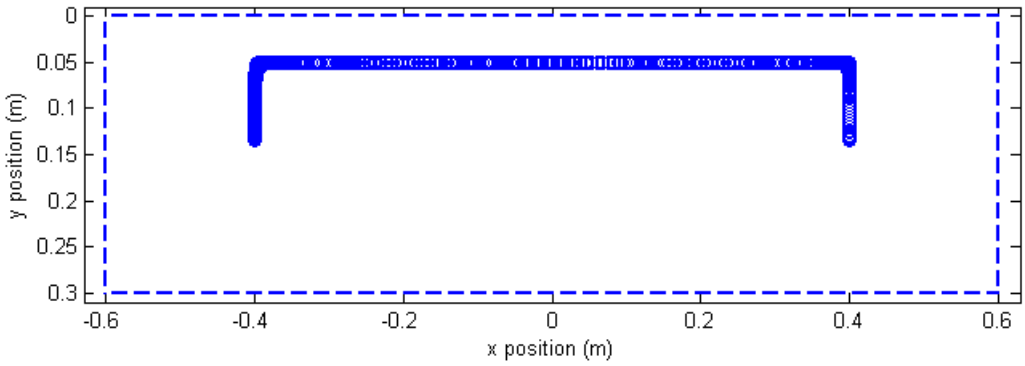

Figure 7-8: Movement of the End-Effector in the Workspace for a Sample Path

Figure 7-9 shows the comparison of measured torque and calculated torque for the left motor, and Figure 7-10 shows the comparison for the right side motor. The calculated torques are off by up to 20% compared to the measured torque at some places, and the measured torque varies more erratically. However, they are fairly close and the key features of the curves match with each other. The peaks after 1.5 seconds and 4 seconds correspond to the quick vertical movements of the end-effector for pick-up and drop-off motion .

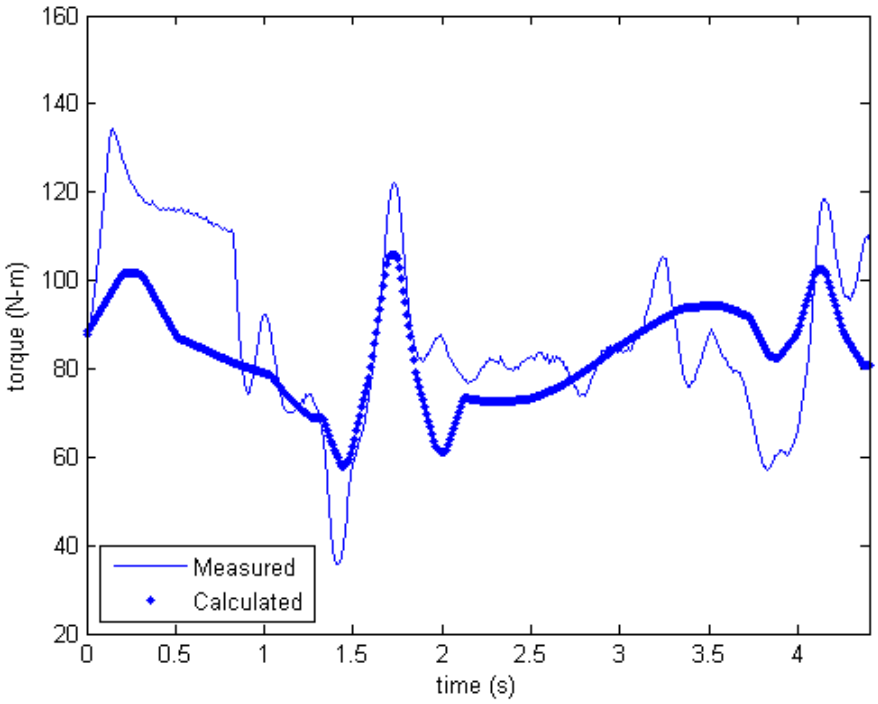

Figure 7-9: Measured vs. Calculated Torques for Sample Path (Left Motor)

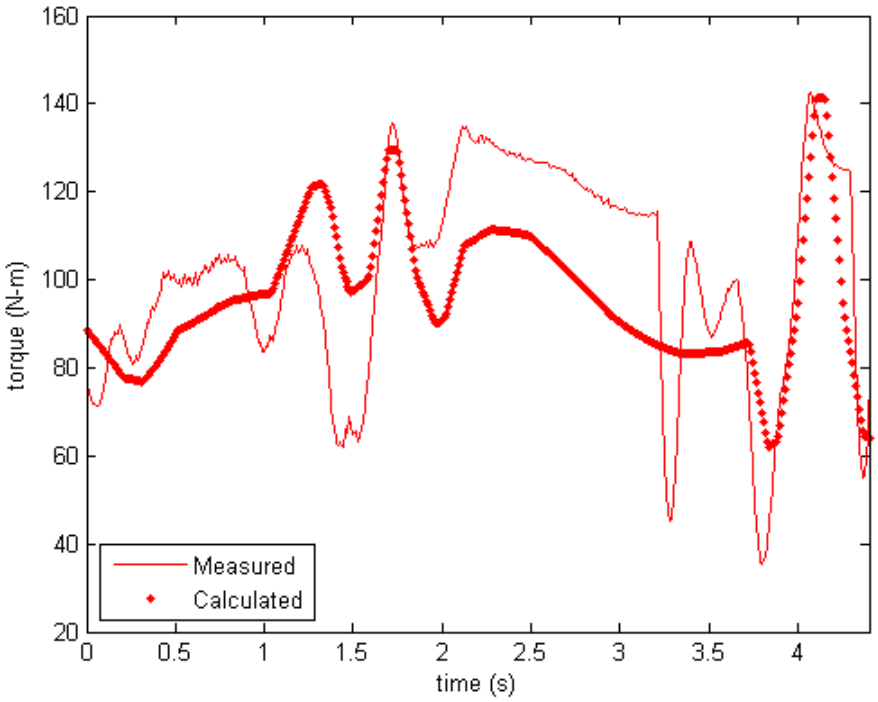

Figure 7-10: Measured vs. Calculated Torques for Sample Path (Right Motor)

7.2.2 Stiffness Measurement

The stiffness of the end-effector is measured with a simple experimental setup. The end-effector is equipped with a laser pointer that marks its position on the table, and a spring gauge is used to pull the end-effector in the out-of-plane direction with some force. The displacement of the end-effector is measured in terms of the displacement of the laser beam projected on the table. This is certainly not an accurate way to measure stiffness, but it can provide rough estimates. Measurements were taken at several different end-effector positions, but no measurable differences were observed because the displacements of the laser projection were very small. Table 7-2 shows the measurement result at the exact center of the workspace. Note that these measurements were taken with the add-on parts installed at the upper universal joint for increased stiffness.

Table 7-2: Displacement of the Laser Projection in the Out-of-Plane Direction

Applied Force	Displacement of the Laser Projection
10 N	0 mm
30 N	2 mm
50 N	5 mm
70 N	8 mm
90 N	10 mm

It is hard to conclude anything from this crude measurement except for the fact that the end-effector has very good out-of-plane stiffness. The end-effector moves about 3 *mm* with 40 *N* of applied force. This is close to the calculated value shown in Table 6-5. Recall that the valid range of stiffness estimated in Section 6.4 is only 23 *N*, but in reality the end-effector is able to handle 90 *N* of applied force with the help of mechanical stiffness provided by the additional revolute joint mechanism. 90 *N* is far beyond the expected value of external force in the out-of-plane direction.

7.2.3 Pick-and-Place Demonstration and Performance

A demonstration for the manipulator is performed for an actual pick-and-place operation. Figure 7-11 shows the front view of the demonstration setup. A conveyer belt is placed at bottom center of the workspace. A COGNEX camera system is mounted on the fixed base, out of the workspace plane in the negative *z* direction. Both the conveyer and camera are connected to the PLC Module and computer to be managed from the control program. Figure 7-12 shows the top view of the demonstration setup. The conveyer carries spoons and forks in various spacing and orientations. The program identifies locations and orientations of spoons and forks with the COGNEX camera, then the manipulator picks them up and places them in either the spoon pile or fork pile in a fixed orientation. Rotating the spoons and forks to fix their orientations is an excellent way to demonstrate the new rotational DOF of the end-effector.

Due to the limitation with the motors, the manipulator was only able to run at 70% of the maximum speed, at around maximum acceleration of 2.8 *g* and maximum velocity of 4.2 *m/s*. The motors were overstressed, and there was a risk of faulting the motors if the manipulator was run at higher speed. Another reason is that the kinematics of the manipulator is not properly calibrated at the time of demonstration due to a time constraint. Without proper kinematic calibration, the position of the end-effector has some inaccuracy. In order to address this problem, a simple calibration is applied at the software level to offset images taken by the camera. Although it was not quantitatively measured, the success rate of the pick-and-place operation and repeatability of the manipulator observed during the demonstration was very good. The stiffness of the manipulator is high enough to keep the end-effector sturdy without any noticeable vibrations. In the end, the manipulator was able to achieve 60 cycles per minutes for the pick-and-place operation.

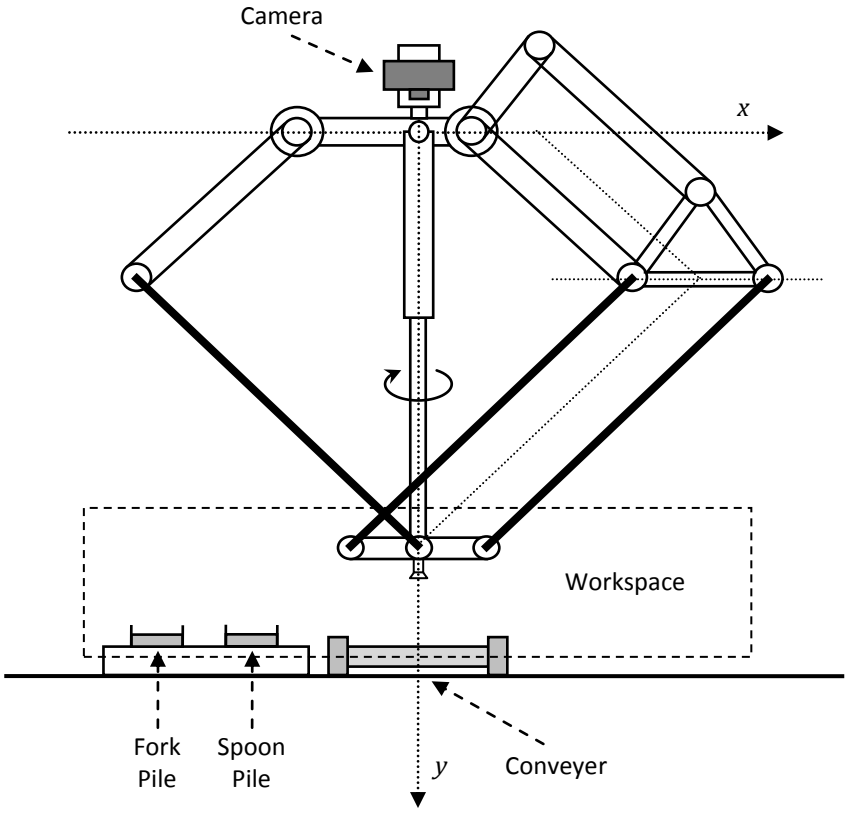

Figure 7-11 Pick-and-Place Demonstration Setup (Front View)

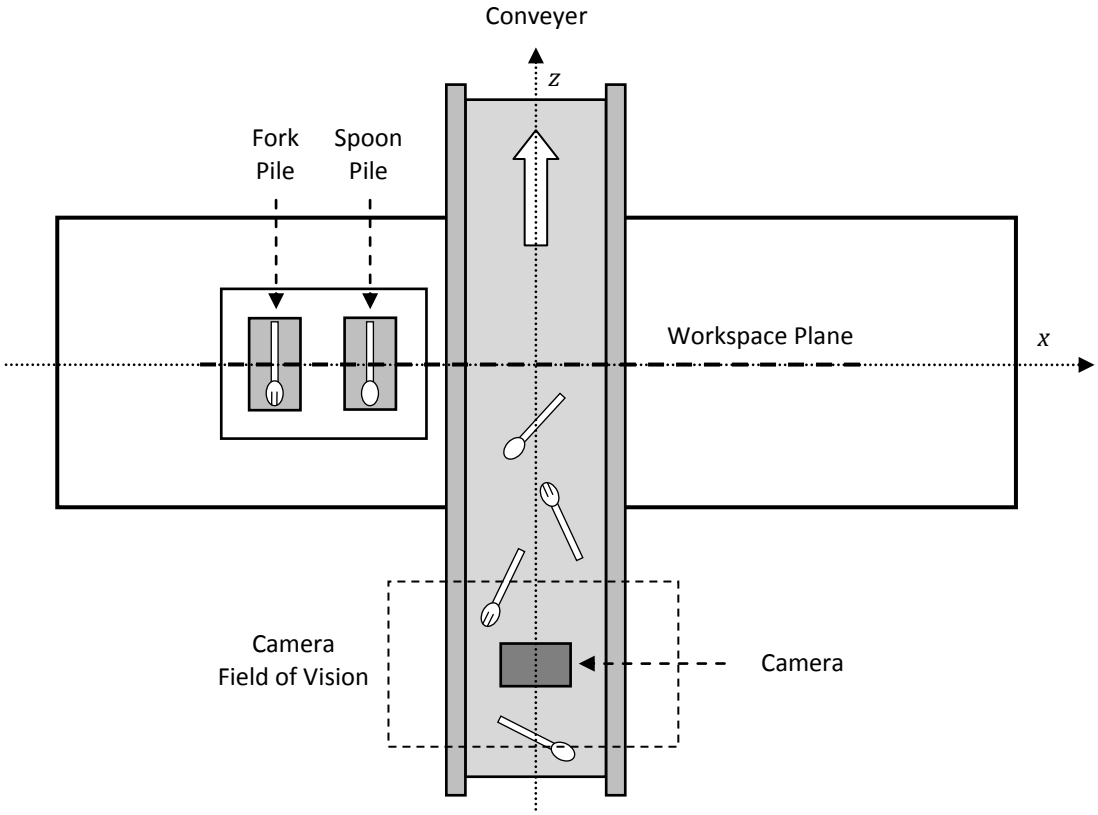

Figure 7-12 Pick-and-Place Demonstration Setup (Top View)

Chapter 8

Conclusions and Recommendations

8.1 Conclusions

The goal of this thesis was to investigate and validate the design and implementation of a new 2D cable-based parallel manipulator. The new manipulator design added a new rotational DOF to the end-effector in addition to the original 2D planar workspace design. This thesis proposes to transmit rotation to the end-effector by physically rotating a kinematic link in the structure, which in this case is a pneumatic cylinder. This keeps the manipulator a true parallel mechanism where all the actuators are located at a fixed base. In order to transmit rotation to the end-effector, revolute joints on the pneumatic cylinder were replaced with universal joints. This caused the manipulator to lose a significant amount of out-of-plane stiffness. A new six-cable design was proposed to increase the stiffness in the out-of-plane direction, and there were several other mechanical design changes.

The methods for kinematic and dynamic analysis were revised to make the procedure more systematic, and expressions for calculating cable tensions and motor torques were formulated in terms of matrices. This thesis presented a mathematical formulation for the stiffness matrix of the end-effector using spring models for the cables. The resultant stiffness matrix is equivalent to the stiffness matrix formulated by in [2] and [29]. This thesis also presented the concept of a valid range of stiffness calculations and a method to estimate it for this particular manipulator design. Additionally, this thesis

compared stiffness of different cable configurations and showed that the cable configuration has significant effect in the stiffness of the end-effector.

A multi-objective optimization problem was formulated in order to search for the best set of design parameters for the manipulator. The challenge in multi-objective optimization is selecting appropriate weights for each cost function. This thesis presented four optimization methods and compared them in terms of their ability to handle highly non-linear problem space and multiple objectives. It was concluded that the Complete Search method was feasible and it was the best option for the particular optimization problem in this thesis.

A mechanical model of the manipulator was drafted with the best set of design parameters chosen from the optimization process, and a physical prototype of the manipulator was manufactured with the help of partners from Conestoga college. Several experiments and demonstrations were conducted with the physical prototype, and it showed that more powerful motors were needed to run the robot at full speed. Measured torques and calculated torques are compared to verify the dynamic analysis. A pick-and-place demonstration showed that the manipulator has very good stiffness and repeatability. The manipulator was able to demonstrate a sorting and pick-and-place operation at 60 cycles per minute while running at 70% of the maximum speed, which is approximately acceleration of 2.8 *g* and velocity of 4 *m/s*.

8.2 Recommendations

This thesis would like to make the following recommendations for improving the manipulator developed in this thesis and future development of similar cable-based manipulators:

- Accuracy for this particular manipulator can be increased by applying kinematic calibration to correct for imperfection in the manufactured parts. Additionally, further tuning of motor control parameters to reduce the settling time may help as well.

- More powerful actuators are required for manipulator of this size. 2D manipulators require more powerful motors in order to have similar workspace size compared to 3D manipulators, because the arms are required to be much larger and the number of motors are reduced from three to two.

- For development of similar cable-based manipulators, consider the valid range of stiffness calculation in the stiffness analysis. The further the end-effector moves away from its original position, the actual stiffness is more likely to deviate from the calculation and for one of the cables to start losing tension.

- Cable configuration should be the first consideration in cable-based design, because it has significant effect on stiffness due to the natural paths of the cables. This thesis suggests a combination of a parallelogram configuration and a triangle configuration.

- The Complete Search method should be considered as one of the options for optimization of design parameters, because it has unique advantages over other optimization methods.. With the advancement in computing technology, the Complete Search method is becoming more feasible.

Bibliography

[1] Chan E., "Design and Implementation of a High Speed Cable-Based Planar Parallel Manipulator", MASc thesis, University of Waterloo, Canada, 2005.

[2] Behzadipour S., "Ultra-High-Speed Cable-Based Robots", Ph.D thesis, University of Waterloo. Canada, 2005.

[3] Bonev L., "The True Origins of Parallel Robots", *Para//eMIC – the Parallel Mechanisms Information Center, http://www.parallemic.org/Reviews/Review007.html*, 2003

[4] Gough V.E. and Whitehall S.G., "Universal tyre test machine", *Proceedings of 9th International Technical Conference F.I.S.I.T.A.*, pages 177-135, 1962.

[5] Steward D. ,"A platform with six degree of freedom", *Proceedings of the Institute of Mechanical Engineering*, 180: 371-386, 1965.

[6] Shiga Y. Tanaka Y. Goto H. and Takeda H., "Design of a six degree-of-freedom tripod parallel mechanism for flight simulators", *International Journal of Automation Technology*, vol. 5, no. 5, pages 715-716, 2011.

[7] Wang H. Qi Z. Xu G. Hu G. and Huang Z., "Kinematics analysis and motion simulation of a quadruped walking robot with parallel leg mechanism", *The Open Mechanical Engineering Journal*, vol. 4 pages 77-85, 2010.

[8] Clavel R. "Device for the movement and positioning of an element in space." Technical Report, 1990.

[9] Kim H. and Tsai L.W., "Design optimization of a cartesian parallel manipulator". Journal of Mechanical Design, transaction of the ASME, vol. 125 (n1): pages 43-51, 2003.

[10] Ergin M.A. Satici A.C. and Patoglu V., "Design optimization, impedance control and characterization of a modified delta robot", *Proceedings of IEEE International Conference on Mechatronics*, pages 737-742, 2011.

[11] Zhang L. and Song Y., "Optimal design of the delta robot based on dynamics", *Proceedings of IEEE International Conference on Robotics and Automation*, pages 336-341, 2011.

[12] Ghorbel F. and Chetelat O., "A reduced model for constrained rigid bodies with application of parallel robots." *Proceedings of the IFAC Symposium on Robot Control*, SYROCO, pages 57-62, 1994.

[13] Meng L. Chetwynd G. Huang T. Zhanxian L. and Cosselin M., "Conceptual design and dimensional synthesis of a novel 2-dof translational parallel robot for pick and place operations", *Journal of Mechanical Design*, vol.7, pages 449-455, 2004.

[14] Yang Y. Kiu Y. Pi J. Shi Y. and Li W., "Calibration of a 6-PRRS parallel manipulator using D-H method combined with vector chain", *International Conference on Mechatronics and Automation*, pages 3944-3948, 2009.

[15] Kucuk S., "Kinematics, singularity and dexterity analysis of planar parallel manipulators based on DH method", *Robot Manipulators new Achievements*, InTech, pages 387-400, 2010.

[16] Tsai. L. W. and Joshi, S., "Kinematics and optimization of a spatial 3-UPU parallel manipulator", Journal of Mechanical Design, transation of the ASME, vol. 122, pages 439-447, 2000.

[17] Lee K.M. and Shah D.K., "Kinematic analysis of a three-degree-of-freedom in-parallel actuated manipulator", *IEEE Journal of Robotics and Automation*, vol. 4, no. 3, 1988.

[18] Landsberger S. and Sheridan T. "A new design for parallel manipulators", *Proceedings of International Conference on Cybernetics and Society*, pages 812-814, 1985.

[19] Choe W. Kawamura S. and Tanaka S., "Development of an ultrahigh speed robot falcon using wire driven systems", Proceedings of IEEE International Conference on Robotics and Automation, pages 215-220, 1995.

[20] Khajepour A. Behzadipour S., Dekker R. and Chan E., "Deltabot a new cable-based ultra high speed robots", *International Mechanical Engineering Congress and Expo*, ASME IMECE2003-41470, 2003.

[21] Ming A. and Higuchi T., "Study on multiple degree-of-freedom positioning mechanism using wires (part 1)", International Journal of Japan Society and Precision Engineering, vol. 28, issue. 2, pages 131-138, 1994.

[22] Behzadipour S. and Khajepour A., "A new cable-based parallel robot with three degrees of freedom", *Multibody System Dynamics*, vol. 14, issue. 4, pages 371-383, 2005.

[23] Pham C. B. Song S. H. and Yang G., "Tension analysis of cable-driven parallel mechanisms", *IEEE International Conference on Intelligent Robots and Systems*, pages 257-262, 2005.

[24] Fattah A. and Agrawal S. K., "On the design of cable-suspended planar parallel robots", *Journal of Mechanical Design*, vol. 127. Issue. 5, pages 1021-1029, 2005.

[25] Griffis M. and Duffy J., "Global stiffness modeling of a class of simple compliant couplings," *Mechanism and Machine Theory*, vol. 28, issue. 2, pages 207-224, 1993

[26] Ciblak N. and Lipkin H., "Centers of stiffness, compliance and elasticity in the modeling of Robotics systems," *ASME Design Technical Conference*, de-vol. 72, pages 185-195, 1994.

[27] Svinin M. M. Ueda, K. and Uchiyama, M., "On the stability condition of a class of parallel manipulators," *IEEE International Conference on Robotics and Automation*, vol. 3, pages 2386–2391, 2000.

[28] Svinin M. M. Hosoe, S. and Uchiyama, M., "On the Stiffness and Stability of Gough-Stewart Platforms," *IEEE International Conference on Robotics and Automation*, vol. 4, pages 3268–3273, 2001.

[29] Behzadipour S. and Khajepour Amir., "Stiffness of cable-based parallel manipulators with application to stability analysis", *ASME Journal of Mechanical Design*, vol. 128, pages 303-310, 2006.